2016

A multi-scale approach to study Solid Oxide Fuel Cells: from Mechanical Properties and Crystal Structure of the Cell's Materials to the Development of an Interactive and Interconnected Educational Tool

Amjad Aman
University of Central Florida

STARS Citation
Aman, Amjad, "A multi-scale approach to study Solid Oxide Fuel Cells: from Mechanical Properties and Crystal Structure of the Cell's Materials to the Development of an Interactive and Interconnected Educational Tool" (2016). *Electronic Theses and Dissertations, 2004-2019*. 5270.
https://stars.library.ucf.edu/etd/5270

A MULTI-SCALE APPROACH TO STUDY SOLID OXIDE FUEL CELLS: FROM MECHANICAL PROPERTIES AND CRYSTAL STRUCTURE OF THE CELL'S MATERIALS TO THE DEVELOPMENT OF AN INTERACTIVE AND INTERCONNECTED EDUCATIONAL TOOL

by

AMJAD AMAN
B.S. Visvesvaraya Technological University, 2006
M.S. University of Central Florida, 2012

A dissertation submitted in partial fulfillment of the requirements
for the degree of Doctor of Philosophy
in the Department of Mechanical and Aerospace Engineering
in the College of Engineering and Computer Science
at the University of Central Florida
Orlando, Florida

Fall Term
2016

Major Professors: Nina Orlovskaya and Yunjun Xu

ABSTRACT

Solid Oxide Fuel Cells are energy conversion devices that convert chemical energy of a fuel directly into electrical energy. They are known for being fuel-flexible, have minimal harmful emissions, ideal for combined heat and power applications, highly energy-efficient when combined with gas or steam turbines. The current challenges facing the widespread adoption these fuel cells include cost reduction, long-term testing of fully integrated systems, improving the fuel cell stack and system performance, and studies related to reliability, robustness and durability. The goal of this dissertation is to further the understanding of the mechanical properties and crystal structure of materials used in the cathode and electrolyte of solid oxide fuel cells, as well as to report on the development of a supplementary educational tool that could be used in course related to fuel cells. The first part of the dissertation relates to the study of $LaCoO_3$ based perovskites that are used as cathode material in solid oxide fuel cells and in other energy-related applications. In-situ neutron diffraction of $LaCoO_3$ perovskite during uniaxial compression was carried out to study crystal structure evolution and texture development. In this study, $LaCoO_3$ was subjected to two cycles of uniaxial loading and unloading with the maximum stress value being 700-900 MPa. The in-situ neutron diffraction revealed the dynamic crystallographic changes occurring which is responsible for the non-linear ferroelastic deformation and the appearance of hysteresis in $LaCoO_3$. At the end of the first cycle, irreversible strain was observed even after the load was removed, which is caused by non-recoverable domain reorientation and texture development. At the end of the second cycle, however, no irreversible strain was observed as domain reorientation seemed fully recovered. Elastic constants were calculated and Young's modulus was estimated for $LaCoO_3$ single crystals oriented along different crystallographic directions. The high temperature mechanical behavior study of $LaCoO_3$ based perovskites is also of prime importance as solid oxide fuel cells operate at high temperatures. Incidentally, it was observed that as opposed to the behavior of most materials, $LaCoO_3$ exhibits stiffening between 700 °C to 900 °C, with the Young's modulus going from a value of ~76 GPa at room temperature to ~120 GPa at 900 °C. In-situ neutron diffraction, XRD and Raman spectroscopy were used to study structural changes occurring in the material as it was heated. The results from these experiments will be discussed.

The next portion of the dissertation will focus on electrolytes. Numerical simulation was carried out in order to predict the non-linear load-stress relationship and estimation of biaxial flexure strength in layered electrolytes, during ring-on-ring mechanical testing.

Finally, the development of an interactive and inter-connected educational software is presented that could serve as a supplementary tool to teach fuel cell related topics.

To my parents, siblings, and Laurie - for their love, support and for always reminding me what really matters in life

"Let us be grateful to the people who make us happy; they are the charming gardeners who make our souls blossom."

— Marcel Proust

ACKNOWLEDGMENTS

I’d like to first thank my research advisors - Dr. Nina Orlovskaya and Dr. Yunjun Xu, for their patience, support, guidance and commitment. Dr. Nina taught me a lot about fuel cells, material science and gave me the opportunity to work on some extraordinary projects. Dr. Yunjun has always been available, provided useful feedback and supported some of my graduate funding. To them, I express my deepest gratitude.

I would like to thank colleagues, scientists and professors who I got to collaborate with during my PhD. They are Dr. Mykola Lugovy, Dr. Yan Chen, Dr. Richard Stadelmann, Dr. Xinyu Huang, Dr. Dong Ma, Dr. Ke An, Dr. Thomas Graule, Mr. Jakob Kuebler, Dr. Mike Reece, Dr. Alexandru Stoica, Dr. Clarina dela Cruz.

I would like to thank all the professors who were on my dissertation committee – Dr. Stephen Kuebler, Dr. Seetha Raghavan, Dr. Tuhin Das, Dr. Shawn Putnam.

I also thank my colleagues and friends – Dr. Jonathan Wehking, Dr. Zhilin Xie, Dr. Anthony Terracciano, Dr. Richard Stadelmann, Dr. Ashkan Davanlou, Alejandro Carrasco-Pena, Dr. Batikan Koroglu, Nadun Kuruppumullage, Vaahini Ganesan, Dr. Janardan Nath, Joanthan Torres, Manuel David, James Wilson and many others.

I would like to thank my friends and loved ones who have supported me in this journey, especially Shruti Sanganeria, Rashmi Murthy, J. Ann Palomar, Robert Palomar, and Amy Goodman.

I am also very grateful to my university, my department, and the funding agencies that supported the research projects I had the privilege to work on – the National Science Foundation and the U.S. Department of Energy. A portion of this research used resources at the Spallation Neutron Source and the High Flux Isotope Reactor, a DOE Office of Science User Facility operated by the Oak Ridge National Laboratory.

TABLE OF CONTENTS

LIST OF FIGURES

LIST OF TABLES

CHAPTER 1: INTRODUCTION

1.1. Why renewable energy?

The need for clean, sustainable and cost-effective energy has become of the biggest challenges of the century. There are numerous reasons for this – growing population, wide spread adoption of power dependent-devices as simple as computers in developing and third world countries, continued development of automation in all sorts of fields, problems arising from greenhouse gas emissions and their effects on earth's atmosphere and the weather, concern about the depletion of fossil fuels. According to the International Energy Agency, the energy demands are predicted to grow globally by 37% by 2040, the market share of renewables in terms of total power generation will go up to 33% in 2040 and the global investment in renewables will go from $121 billion in 2013 to $205 billion in 2014 [1]. Since the 1997 Kyoto Protocol, the European Union (EU) and many other countries in the world started focusing their efforts to reduce their dependence on fossil fuels to generate power and to rather depend on renewables, as witnessed by the commitment made by the EU to reduce CO_2 emissions by 20% by the year 2020 compared to the levels reported in 1990 and the commitment made by UK to reduce greenhouse gas emissions by 80% by the year 2050 compared to the levels reported in 1990 [2]. In March 2015, the United States submitted a report, also known as an Intended Nationally Determined Contribution (INDC), to the United Nations Framework Convention on Climate Change (UNFCCC) that expresses the country's goal of reducing greenhouse emissions by 26-28% in 2025 below the levels recorded in 2005, as seen in Figure 1 [3].

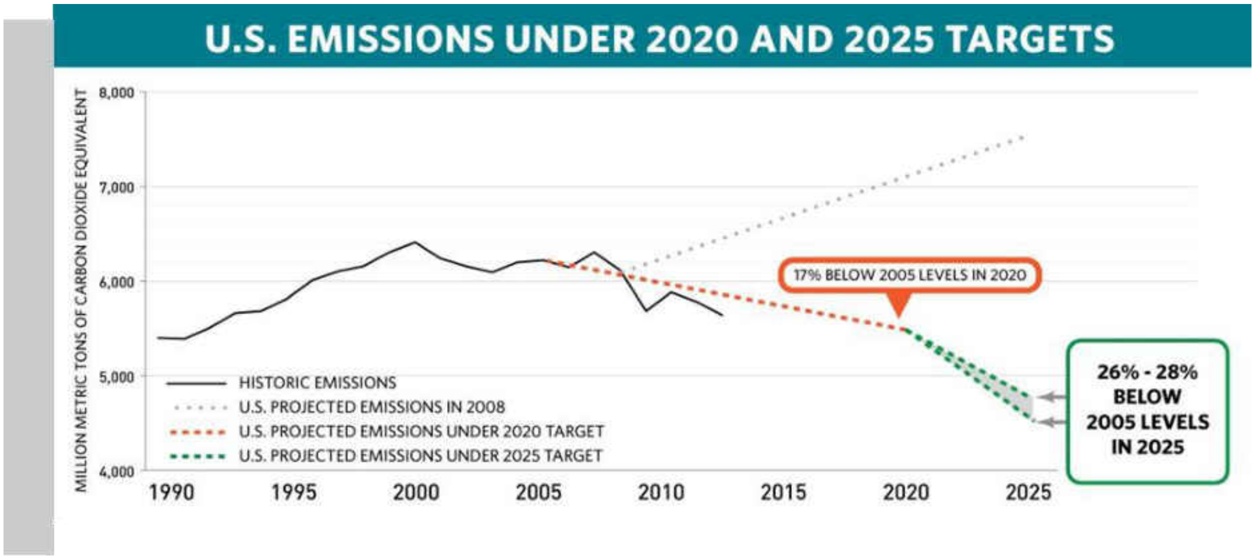

Figure 1: Graph shows the greenhouse gases emissions for the United States in the past and the projected goal for reducing emissions by 2020 and 2025 in comparison to the levels in 2005 [3]

1.2. Why Fuel Cells?

A fuel cell is an energy conversion device that can convert the chemical energy of a fuel to electrical energy and heat, through electrochemical reactions. The heat released may be significant or not, depending on the type of fuel cell. A battery operates in a similar manner, except in the case of batteries the fuel is stored within the battery and is not replenished, which gives it a limited life. On the contrary, fuel cells can run as long as the fuel is replenished. Combustion engines convert chemical energy of the fuel to mechanical energy and thermal energy, and if electrical energy is the desired output there will be an additional energy conversion process. Fuel cells can have higher efficiency compared to combustion engines since the additional energy conversion process is eliminated, and are not limited by the Carnot cycle. In addition fuel cells have no moving parts and this avoid the problem of vibrations, noise, friction, wear and tear. These devices can be very environmental friendly with minimal or zero emission of harmful gases. Fuel cells can operate continuously for months or years, in fact a research group from Forschungszentrum Jülich performed a long-term test that lasted for more than 5 years in August 2012, with a goal of reaching operation time beyond 17 years [4].

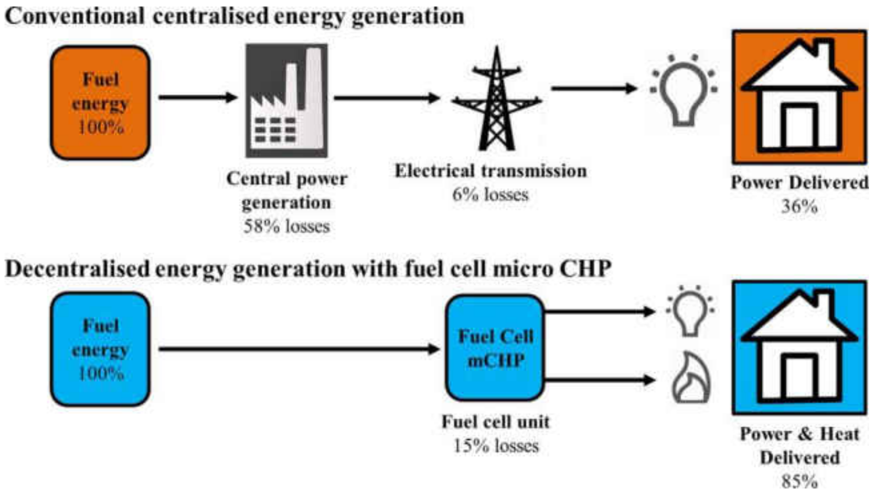

Figure 2. Illustration of losses encountered in using the traditional internal combustion engines to generate power using a centralized system, versus the minimal losses encountered when a fuel cell system tailored to serve as a micro Combined Heat and Power (CHP) system can be used to deliver both power and heat [2]

The first fuel cell was invented by the English scientist William Robert Grove in 1839 [5]. Figure 2 shows the minimal losses encountered in using a fuel cell system to convert chemical energy of the fuel into electrical energy and heat, compared to the conventional centralized power conversion and distribution system. Fuel (in this case hydrogen) enters at the anode electrode, through electrochemical reactions hydrogen is split into positive ions and electrons (oxidation process). The oxidant (in this case oxygen) enters at the cathode side is reduced to oxidized species (reduction process). The protons travel through the electrolyte and the electrons through an external circuit. When all these species combine, they form water. The purpose of the electrolyte is to allow passage of only a particular positive or negative ion and also avoid crossover of other species.

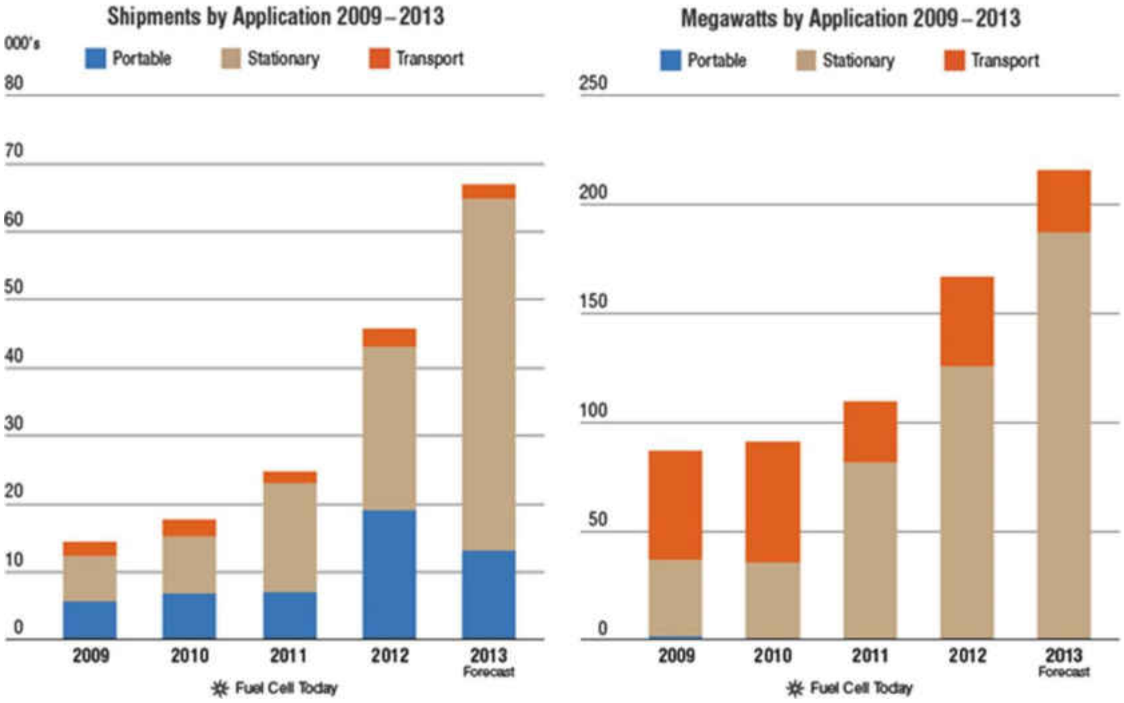

Figure 3: Worldwide shipment of fuel cell systems are increasing each year [6]

1.3. Types of Fuel Cells

There are five fundamental types of fuel cells: Alkaline fuel cells (AFC), Phosphoric acid fuel cells (PAFC), Polymer electrolyte membrane fuel cells (PEMFC), Molten carbonate fuel cells (MCFC), and Solid oxide fuel cells (SOFC). Direct methanol fuel cells (DMFC) is a subset of PEMFC. Figure 4 illustrates the different types of fuel cells in terms of the materials used, operating temperature range and charge carrier through the electrolyte. The main difference between each of these fuel cells is the type of electrolyte used, and the charge carrier that migrates through the electrolyte. SOFCs use a ceramic electrolyte. The conceptual Solid Oxide Fuel Cell was probably first demonstrated in 1937 by the Swiss scientists Emil Bauer and Hans Preis using zirconia ceramics as the electrolyte, Fe_3O_4 as the cathode, and C as the anode [7].

Currently, the most common Solid Oxide Fuel Cell uses yttria-stabilized zirconia as the electrolyte, which is an oxygen ion conductor.

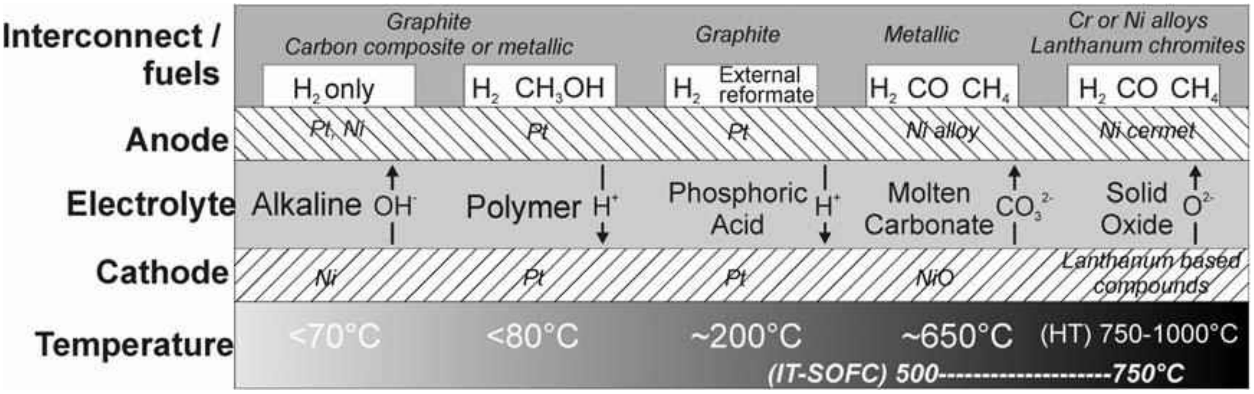

Figure 4: Illustration of the fundamental types of fuel cells [8]

1.4. Solid Oxide Fuel Cell

A fuel cell consists of four main functional components: anode, electrolyte, cathode, and interconnect. As mentioned before a Solid Oxide Fuel Cell (SOFC) uses a solid ceramic electrolyte. The chemical reactions of a typical SOFC is given,

Anode: $$\boldsymbol{H_2 + O^{2-} \rightarrow H_2O + 2e^-}$$

Cathode: $$\boldsymbol{\frac{1}{2}O_2 + 2e^- \rightarrow O^{2-}}$$

This type of SOFC uses an electrolyte that is called a oxygen ion conductor. Figure 6 shows an example of such SOFC [9][9]. Anode is the electrode where oxidation process takes place and cathode is the electrode where reduction process takes place. Hydrogen gas (fuel) is supplied at the anode and oxygen gas or air (oxidant) is supplied at the cathode. Oxygen undergoes reduction (process of electrons are consumed), the oxygen ions (O^{2-}) are transported through the electrolyte. At the anode the hydrogen atoms undergo oxidation (process of liberation of electrons), they combine with the oxygen ions to form water and releases two electrons in the process. The liberated electrons travel through an external circuit via current collectors, hence producing electricity, and reach the cathode where they combine with oxygen atoms to create more oxygen ions. Therefore, the function of the electrolyte is to facilitate the conduction of oxygen ions, prevent electronic conductance, prevent passing over of gases and other species from one side to the other. The most popular SOFC electrolyte is yttria-stabilized zirconia possess the ability to withstand the highly reducing high-temperature environment at the anode, and the air electrode must possess the ability to withstand the highly oxidizing high-temperature environment of the cathode. The most common material for the anode electrode in a SOFC is nickel-YSZ cermet (a cermet is a mixture of ceramic and metal). Conductivity and catalytic activity is the purpose of nickel, while YSZ adds ionic conductivity, thermal expansion compatibility, and mechanical stability and helps maintain high porosity and surface area of the anode structure. Mixed ion-conducting and electronically conducting (MIEC) ceramic materials are usually used for the cathode electrode. Some examples are strontium-doped lanthanum manganite (LSM), lanthanum-strontium ferrite (LSF), lanthanum-strontium cobaltite (LSC), and lanthanum strontium cobaltite ferrite (LSCF). High catalytic activity and good oxidation resistance are the reasons these materials are chosen for the cathode electrode. By varying the compositions of the materials at the cathode, anode and electrolyte different levels of properties like ionic conductivity, catalytic activity, and thermal expansion compatibility can be achieved. SOFCs could also employ electrolytes that proton ion conductors. In such SOFCs the electrolytes conduct proton ions as shown in Figure 6, and hence the only other difference compared to the oxygen/negative ion conducting fuel cell is the site where water is produced, the water being produced at the cathode. The more common type of SOFCs are the ones that use negative ion conductor electrolytes. The overall driving force for a SOFC is the chemical or concentration gradient of oxygen between the cathode where the partial pressure of oxygen is high to the anode where the partial pressure of the oxygen is low. The thermodynamic voltage output of a single SOFC based on the electrochemical half reactions is around 1.23 V at standard temperature and pressure conditions. As it can be noticed this voltage is low and inadequate for practical use. To produce voltage and power that is high enough to suffice energy requirements the individual cells can be connected in series and/or parallel with the aid of interconnectors and/or cell-to-cell connectors. The cell-to-cell connectors need to be ionic insulator and pure electronic conductors. This method is called stacking of cells and it is the way SOFC are designed for practical power generation. The complete fuel cell system consists of a number of stacks of individual fuel cells. A fuel cell system however includes a number of other components apart from the fuel cell stack, like reformer, heat exchangers, fuel and oxidant storage, flow control systems, catalytic combustor, etc. An illustration of a SOFC system can be seen in Figure 5.

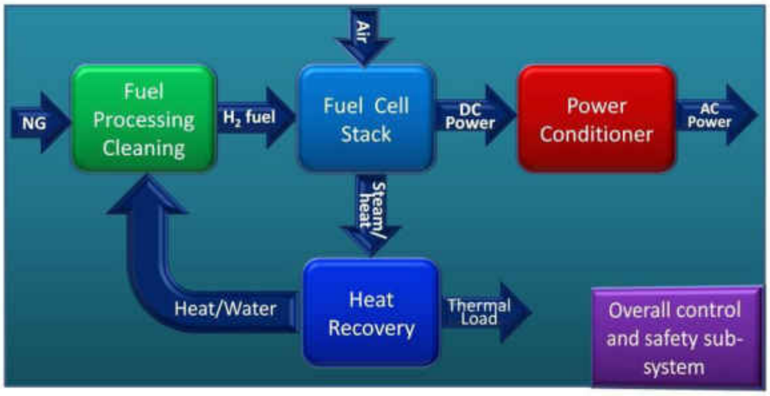

Figure 5: An illustration of the different sub-systems that are part of a fuel cell system [10]

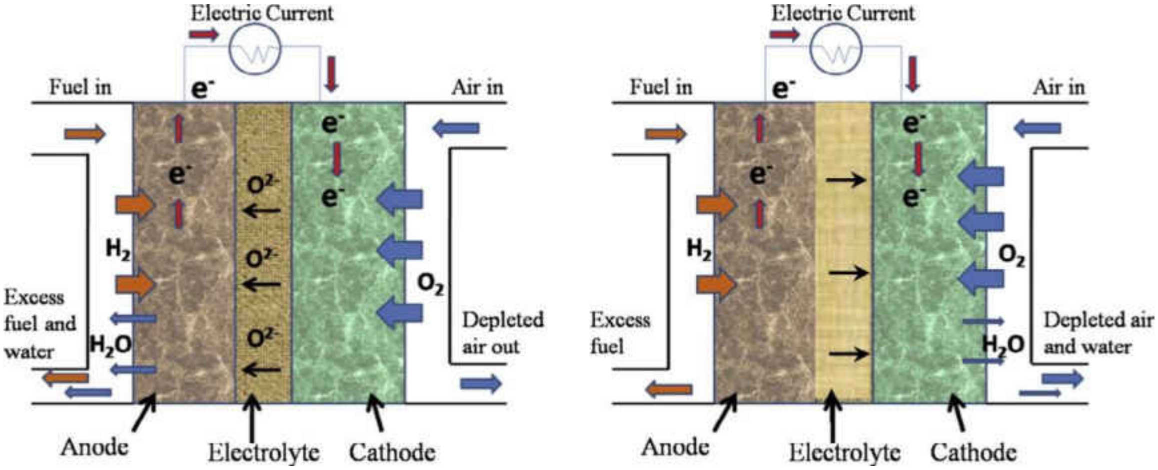

Figure 6: The working of a solid oxide fuel cell that uses oxygen ion charge carriers (left) and proton ion charge carriers (right) [11]

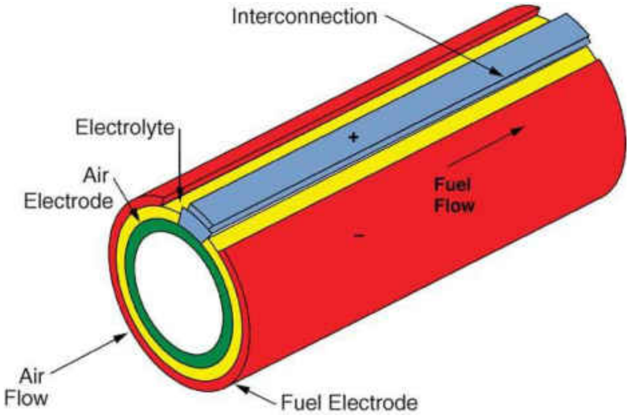

Figure 7. Tubular fuel cell design by Seimens Westinghouse [12, 13]

1.4.1 Designs of Solid Oxide Fuel Cells

There are different designs of SOFC. Modern SOFC generally is made of a thin electrolyte film and a supporting substrate. The substrate is a porous or channeled dense body for gas transport, ad is made of anode and cathode electrodes, interconnect (metal or ceramic), or inactive insulator. The substrate can be classified geometrically as tubular (cylindrical or flattened and ribbed), an example can be seen in Figure 8 and Figure 10. The tubular geometry design was introduced by Siemens Westinghouse Power Corporation in the 1970s and have been continuously developing this design since [12]. In this type of design one closed end is usually closed and the feature allows for a seal-less design. This design has proven to demonstrate continued performance over long periods of time, with a 0.1% degradation for every 100 hours of operation[13]. The company has demonstrated that this particular design can withstand thermal cycling from room temperature to 1000ºC over a 1000 times. Most recently, the corporation has produced a 250 kW power system in Canada that employs 2292 tubular SOFCs in its design. In the tubular SOFC design, it is common to fabricate the thin fuel cell components directly onto the outside of a thickened porous support tube. The surface area available on the outside of each tube is often subdivided into a row of cells that are connected in series, a design referred to as segmented-in-series[14]. Other companies that have been involved in the production of tubular SOFCs are Acumentrics in the USA; and Kyocera, TOTO and Mitsubishi Heavy Industries in Japan[15]. The main advantages of tubular design include lesser sealing issues and ease in enlargement of cells; whereas the disadvantages include higher manufacturing cost and lower power density. The other geometric design of SOFC is the planar design. In this type of design fuel cell components are usually flat and assembled one on top of the other. The thickness of each component may vary, and the shape of the cell may be rectangular or circular.

Figure 8 shows an example of the planar SOFC design. This type of design deals with more sealing problems compared to tubular designs and enlargement of the cells is more difficult, but the advantages include higher power density and lower manufacturing cost. The main developers of planar designs include Mitsubishi Heavy Industries and Tokyo Gas (Japan), Ceramic Fuel Cells Ltd. (Australia), Haldor Topsoe (Denmark), H.C. Starck (The Netherlands), Ceres Power and Rolls Royce (UK), VTT (Finland), BMW, HC Stark and Webasto (Germany), Sulzer (Switzerland), HTCeramix/SOFCpower (Italy), SOFCo, Delphi Automotive Systems, GE, ZTek (USA) and Global Thermoelectric (Canada)[15]. The planar design makes staking of the cells easier and makes it a favorable design.

The single cell design can also be classified in a different manner in which the cell can be external-supporting or self-supporting. In external-supported design the cells components are thin and are supported by the external substrate or the interconnect. In the case of self-supported designs, one cell components is made thicker and more robust than the others to support the entire cell. The most common types are electrolyte-supported, anode-supported and cathode-supported. These designs can be seen in Figure 9. Electrolyte-supported cells were one of the earliest designs, but the higher thickness led to higher resistivity. By making the electrolyte thinner, lower loses from resistance could be achieved, but then the mechanical robustness of the electrolyte became an issue. The focus of this work will be on overcoming these challenges and develop effective electrolyte-supported cells. Cathode-supported cells tend to have heavy losses due to its and are rarely used. Anode-supported design has gained a lot of attention in the recent years. A summary of the advantages and disadvantages of each design is shown in Figure 9. Another important way to categorize SOFCs is by their operating temperature: High temperature

SOFC (HT-SOSC) [800 ºC – 1000 ºC], Intermediate temperature SOFC (IT-SOFC) [600 ºC – 800 ºC] and Low temperature SOFC (LT-SOFC) [300 ºC – 600 ºC]. A more detailed discussion of these types will be presented under the electrolytes section of this document.

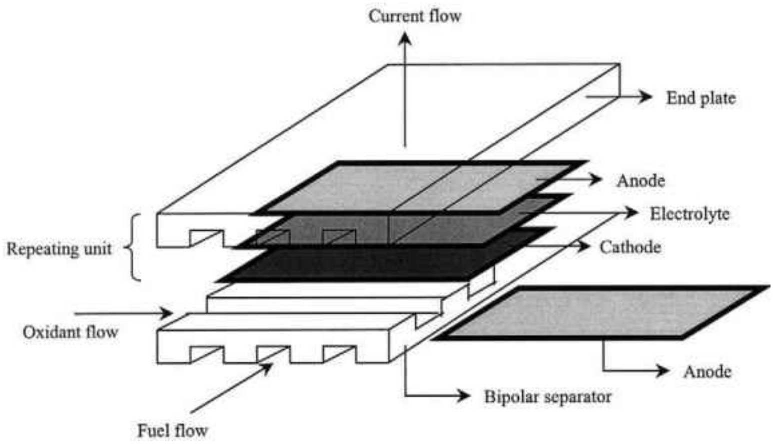

Figure 8. Planar design of SOFCs [9]

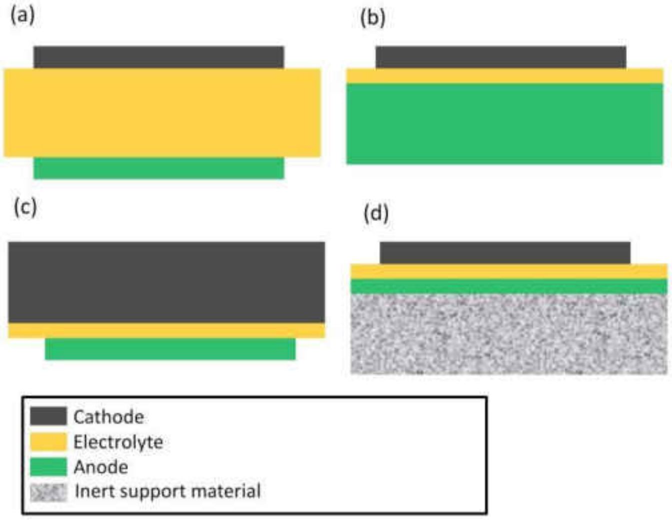

Figure 9: Different designs of fuel cells a) Electrolyte-supported b) Anode-supported c) Cathode-supported d) Ceramic- or metal-supported [10]

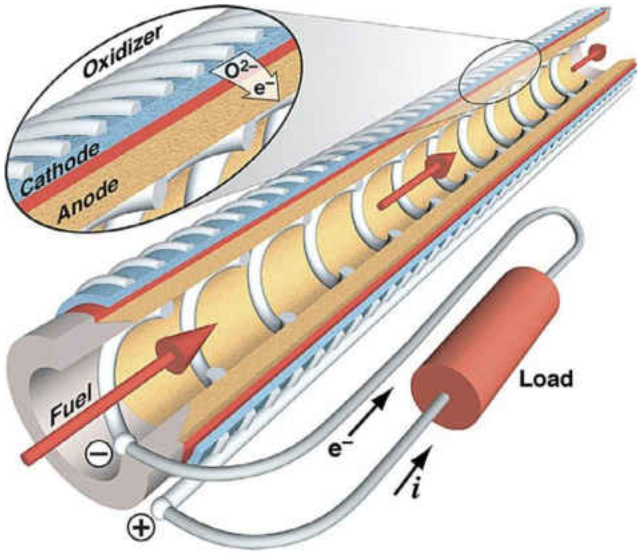

Figure 10: Design of an anode supported tubular SOFC [16]

Table 1. Comparison of the differnt configurations of single cells [17]

Cell configuration	**Advantages**	**Disadvantages**
Self-supporting		
Electrolyte-supported	▪ Relatively strong structural support from dense electrolyte ▪ Less susceptible to failure due to anode reoxidation (Ni/YSZ anode) and cathode reduction (LSM cathode)	▪ Higher resistance due to low electrolyte conductivity ▪ Higher operating temperatures required to minimize electrolyte ohmic losses
Anode-supported	▪ Highly conductive anode ▪ Lower operating temperature via use of thin electrolytes	▪ Potential anode reoxidation ▪ Mass transport limitation due to thick anodes
Cathode-supported	▪ No oxidation issues but potential cathode reduction ▪ Lower operating temperature via use of thin electrolyte	▪ Lower conductivity ▪ Mass transport limitation due to thick cathodes
External-supporting		
Interconnect-supported	▪ Thin cell components for lower operating temperature ▪ Stronger structures from metallic interconnects	▪ Interconnect oxidation ▪ Flowfield design limitation due to cell support requirement
Porous substrate	▪ Thin cell components for lower operating temperature ▪ Potential for use of non-cell material for support to improve properties	▪ Increased complexity due to addition of new materials ▪ Potential electrical shorts with porous metallic substrate due to uneven surface

1.4.2. Advantages of SOFC

Solid Oxide Fuel Cells have numerous advantages. They are one of the most studied and researched fuel cells currently. There is a real drive to their commercialization. Here are some advantages of SOFCs:

- Flexibility in the type of fuel used.

- High electrical efficiency compared to other types of fuel cells in the range of 50-60% [18].
- Wide power generated range, 10 – 100,000 kW [18].
- Could be sued in stationary and portable power generation.
- Lower CO_2 emissions per unit electricity produced (if the fuel used is a hydrocarbon) when compared with combustion engines [5].
- Less prone to CO poisoning and therefore suitable for coal-based fuel.
- Higher electrical efficiency when compared with conventional heat engines, since they are not limited by Carnot cycle.
- Nickel could be used as catalyst instead of platinum, which is very cost effective.
- Negligible greenhouse gases emission if hydrogen is the fuel used.
- High quality waste heat, which makes co-production of heat and power (CHP) possible.
- No moving parts, therefore less vibrations and noise.

1.4.3. Applications of SOFC

The primary use of Solid Oxide Fuel Cells has been in stationary power generation [5]. Portable applications of SOFCs have been explored but they have been found not to be very viable for portable applications due to the high operating temperatures (600 to 1000°C) and the low shock resistance of its ceramic components. In their paper, Wolfgang Winkler and Hagen Lorenz say that the integration of a solid oxide fuel cell (SOFC)–GT (gas turbine) power system in an all-electric car concept seems to be possible [19]. The most common ways in which SOFCs are beings used are as residential/building power, combined heat and power plant and cogeneration/trigeneration/quadgeneration [20].

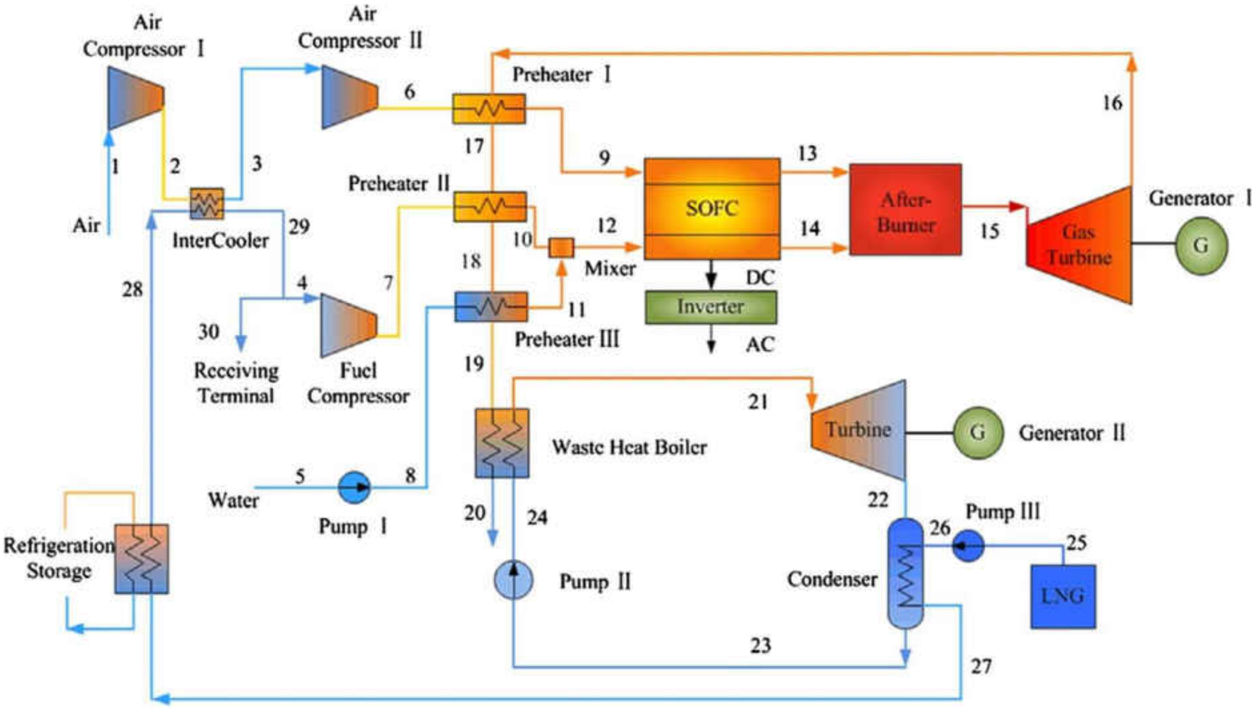

Figure 11: Layout and components of a SOFC-Gas Turbine power plant that uses Liquid Natural Gas (LNG) as fuel. This is one of the proposed designs for the combined systems of SOFCs and gas turbines [16, 21]

Commercialization of SOFC is the ultimate dream and motivation of researches. Some of the big companies that produce SOFCs include FuelCell Energy, Ballard Power Systems, Delphi. One of the other notable companies is Bloom Energy® - founded in 2001 by Dr. KR Sridhar; has successfully demonstrated the commercial uses of SOFC. Their patented SOFC technology has been used to create a type of distributed power generator called Energy Server™ that uses renewable and fossil fuels to generate power in the range of 100 kW [22]. Their customers include big corporations like Google, The Coca-Cola Company, Walmart, California Institute of Technology, IKEA and many more.

1.4.4. Material challenges in SOFCs

The materials used in SOFCs are mainly ceramics. Over the years researchers have proposed and studied many suitable materials for the different components of the SOFC. Mahato et al., have done a great job of summarizing most of the materials used in SOFCs based on each cell component [11]. SOFCs tend to operate at peak electrochemical performance in the temperature ranges of 800 to 1000ºC [23, 24]. The reason for this is that at such temperatures the ionic conductivity of the electrolyte and the chemical reaction rates tend to be relatively high, which leads to higher current density produced in the fuel cell. But operating at these temperatures have adverse effects which include (i) longer start-up and shut down times, (ii) higher operating costs, (iii) higher mechanical and structural degradation, and (iv) need to use expensive ceramics or chromite steel for interconnect materials that could be replaced by economically cheaper ferritic stainless steel at lower temperatures [24]. Therefore, there has been a push to lower the operating temperature of SOFCs in the recent years. The ionic conductivity of electrolytes like yttria stabilized zirconia (YSZ) is higher at higher temperatures; therefore some researchers have proposed to reduce the thickness of the electrolyte layer significantly, as the lower thickness will result in lower resistivity of the electrolyte. There has also been a lot of work done to find SOFC materials that perform well at lower temperatures, leading to intermediate- and low- temperature SOFCs [25]. In the case of electrolytes, gadolinia doped ceria (GDC) has ionic conductivities at 600ºC similar to YSZ at 800ºC [10]. The other alternative electrolyte materials that have been studied in depth are doped Bi_2O_3 and lanthanum strontium magnesium gallate (LSGM) perovskite. Although there has been a lot of work invested in exploring the above mentioned electrolyte materials, there has been a number of challenges associated with them. When it comes to GDC, the Ce^{4+} ions get reduced to Ce^{3+} ions, this causes electronic conduction across the electrolyte which is undesirable and also leads to significant lattice expansion [26, 27]. LSGM has good potential to be used in intermediate-temperature SOFCs but the difficulty lies in producing it in the form of a single phase. Secondary phases are known to form and affect the working of the electrolyte.

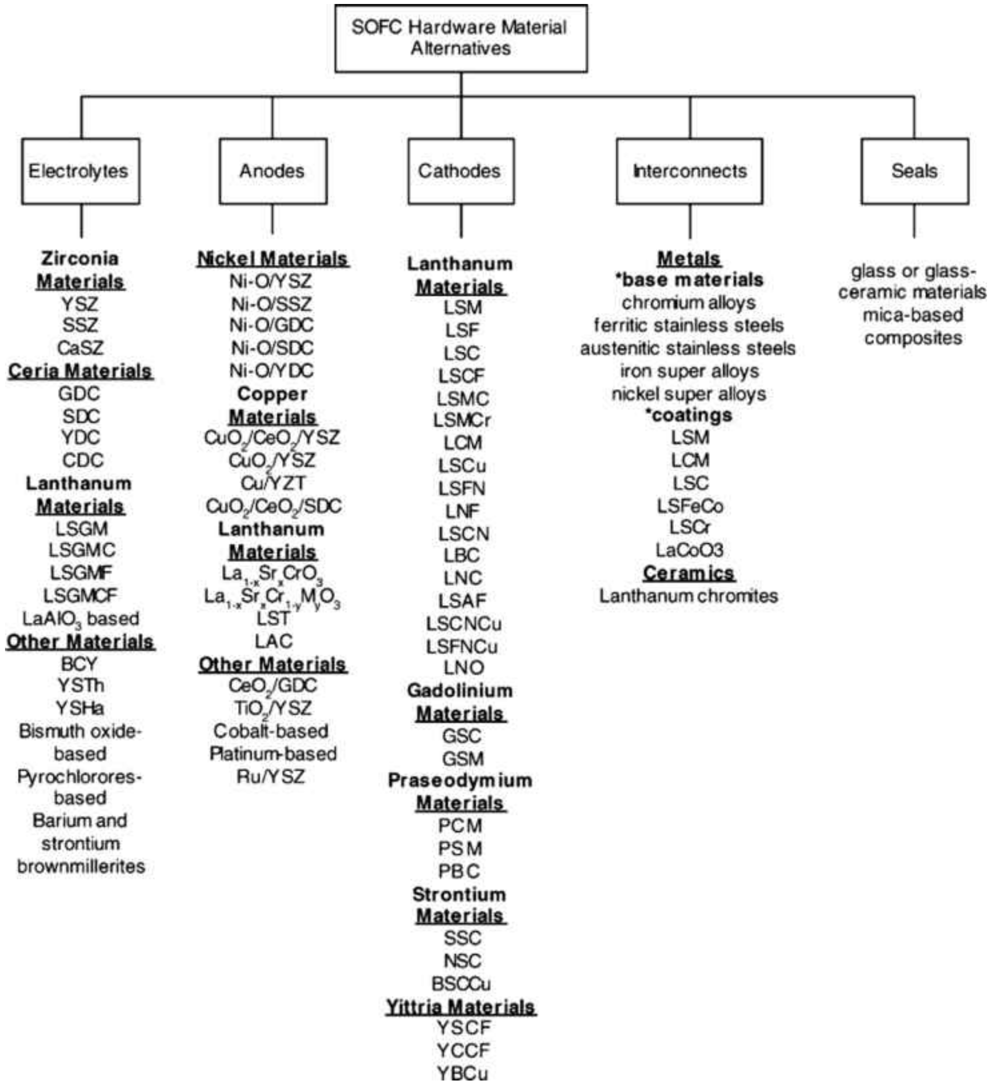

Figure 12: Chart showing all the possible types of materials that can used for the main components of a SOFC [11]

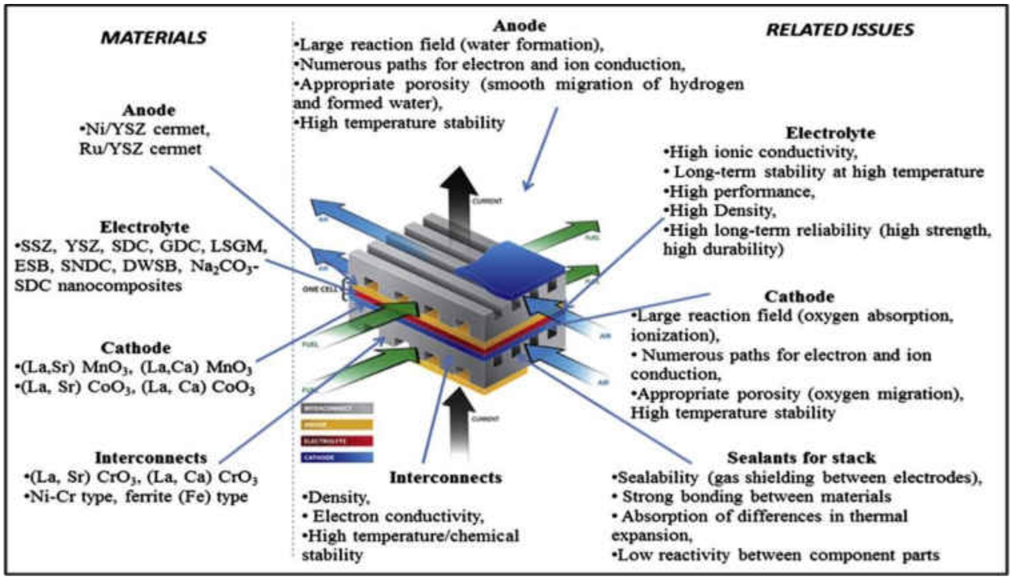

MATERIALS

Anode
- Ni/YSZ cermet,
  Ru/YSZ cermet

Electrolyte
- SSZ, YSZ, SDC, GDC, LSGM, ESB, SNDC, DWSB, Na_2CO_3-SDC nanocomposites

Cathode
- $(La,Sr)\,MnO_3$, $(La,Ca)\,MnO_3$
- $(La, Sr)\,CoO_3$, $(La, Ca)\,CoO_3$

Interconnects
- $(La, Sr)\,CrO_3$, $(La, Ca)\,CrO_3$
- Ni-Cr type, ferrite (Fe) type

RELATED ISSUES

Anode
- Large reaction field (water formation),
- Numerous paths for electron and ion conduction,
- Appropriate porosity (smooth migration of hydrogen and formed water),
- High temperature stability

Electrolyte
- High ionic conductivity,
- Long-term stability at high temperature
- High performance,
- High Density,
- High long-term reliability (high strength, high durability)

Cathode
- Large reaction field (oxygen absorption, ionization),
- Numerous paths for electron and ion conduction,
- Appropriate porosity (oxygen migration), High temperature stability

Interconnects
- Density,
- Electron conductivity,
- High temperature/chemical stability

Sealants for stack
- Sealability (gas shielding between electrodes),
- Strong bonding between materials
- Absorption of differences in thermal expansion,
- Low reactivity between component parts

Figure 13: Schematic of the different materials used in SOFCs and the challenges associated with each of them [11]

1.4.4.1. Electrolyte

SOFCs in the past have been operated in the high temperature range of 850-1000°C (HT-SOFC) and have been successfully demonstrated by companies like Siemens-Westinghouse and Rolls-Royce [28], [17]. This temperature range is used because the ionic conductivity of electrolytes is higher at these temperatures. But, operating the cells at such high temperature has disadvantages like material degradation, economic issues and complications due to the sophisticated technology needed [9, 29, 30]. An example of the problems like material degradation is the sintering of nickel at the anode at high temperatures, which causes reduction in porosity and effectiveness of the catalyst [30]. Lowering the operating temperature can be highly beneficial as it will reduce the heat needed to operate the fuel cell, reduce thermal cycling stresses in the fuel cell components, increase life of the overall fuel cell, demand less from the thermal management sub-system, reduce operating cost, lower the time for system start-up and shutdown. There has been a trend in the past few years to migrate from high-temperature (>800°C) to intermediate-temperature (650 to 800°C) and low-temperature (<650°C) fuel cell [31, 32].

The electrolyte in a fuel cell plays the role of being the medium for the positive or negative charge carrier to travel from one electrode to the other; it must have a dense microstructure to avoid mixing of the fuel and oxidant [33], and must be a poor electron conductor at the operation temperature. It must be able to withstand reducing (cathode) and oxidizing (anode) environment produced at the electrodes. In addition, for SOFCs the electrolyte needs to be thermally stable, have a coefficient of thermal expansion value comparable to the other cell components, maintain high ionic conductivity at elevated and should not chemically react with the anode or cathode material. The electrolyte material needs to have vacancies in the crystal structure for the charge carrier ions to migrate through them, current flows through the electrolyte by migration of these ions. Ideally, the ionic current through the electrolyte should match with the electronic current through the electronic circuit at the operating temperature of the cell [34]. The electrolyte material also needs to be easy to fabricate and manipulate mechanically to suit particular designs of the single cells. Furthermore, the mechanical strength and durability of the electrolyte material under thermal cycling become significant factors. This is especially important in the case of electrolyte-supported fuel cells. Lastly, cost of the material plays a big role too and is one of the biggest challenges in the wide spread commercialization of fuel cells/SOFCs. In their 2013 paper, Marques and Figueiredo presented their findings from the research done on all the various solid electrolytes in the form of a figure [35]. Figure 14 is the figure from their paper and shows where different solid electrolytes stand with regards to their stability versus their position in the market, and the knowledge base versus market position for each of them. ZrO_2 doped with 8 mol% Y_2O_3 [$(Y_2O_3)_{0.08}(ZrO_2)_{0.92}$ or 8YSZ] is the most commonly used electrolyte due to its relatively lower cost, superior phase stability in oxidizing and reducing environments, and mechanical properties. The rest of this section will help explain why.

The most commonly used electrolytes in SOFCs are the ones that conduct oxygen ions (O^{2-}). There has been some work done to explore the use of proton conducting electrolytes but their ionic conductivity tends to be lower than that of O^{2-} conducting electrolytes [17, 36] as seen Figure 15. In O^{2-} conducting electrolytes, the oxygen ions are the largest components of the lattice structure, ionic radius of approximately 0.14 nm and travel through a thermally activated hopping mechanism from one unoccupied site to the other [37]. The electrolyte material needs to have significantly high oxygen ion conductivity and materials with inherent oxygen defects are ideal candidates. The greater the presence of oxygen vacancies inherently in different crystal structures the greater the oxygen ion conductivity in those materials. A lot of oxides tend to have good oxygen ion conductivity but the ideal candidates are fast ionic conductors at elevated temperatures, such as ZrO_2-, CeO_2-, Bi_2O_3-based materials with fluorite crystal structures or oxygen-deficient perovskites like $LaGaO_3$, $Bi_4V_2O_{11}$ and $La_2Mo_2O_9$ derivatives like BIMEVOX, $(Gd,Ca)_2Ti_2O_{7-\delta}$, pyrochlores and brownmillerites.

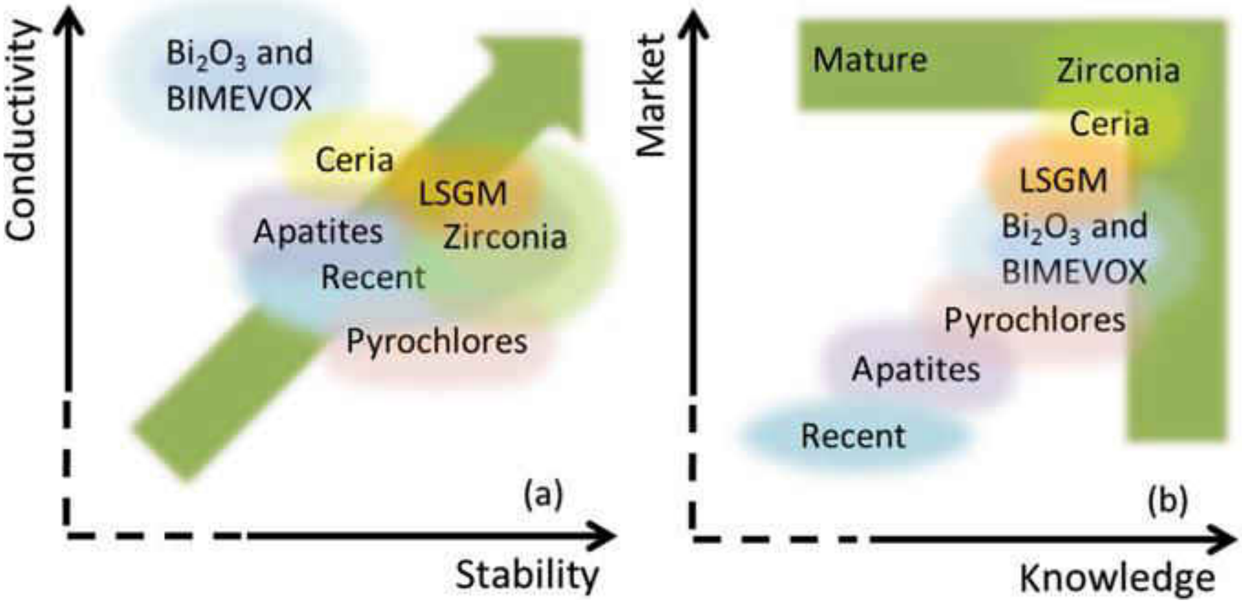

Figure 14. A quantitative comparisons of common solid electrolyte materials and recently discovered materials. (A) Conductivity versus stability comparison in the 600 to 800 °C temperature range. The desired trend is represented using the green arrow. (B) Comparison the quantifiable knowledge gained versus market share of these electrolyte materials. The green color emphasizes the mature materials [35]

Fully stabilized Zirconia (ZrO_2) doped with trivalent oxides are the most extensively used electrolyte materials for SOFCs. Zirconia exists in three structural phases – cubic, tetragonal and monoclinic [38]. Cubic zirconia only exists in elevated temperatures (2643–2953 K), followed by tetragonal zirconia (1443–2643 K) and finally monoclinic zirconia (293-1443 K) [39]. ZrO_2

in the monoclinic form has low ionic conductivity and significant electronic conductivity, and hence is not suitable to serve as electrolyte material in SOFCs [40].

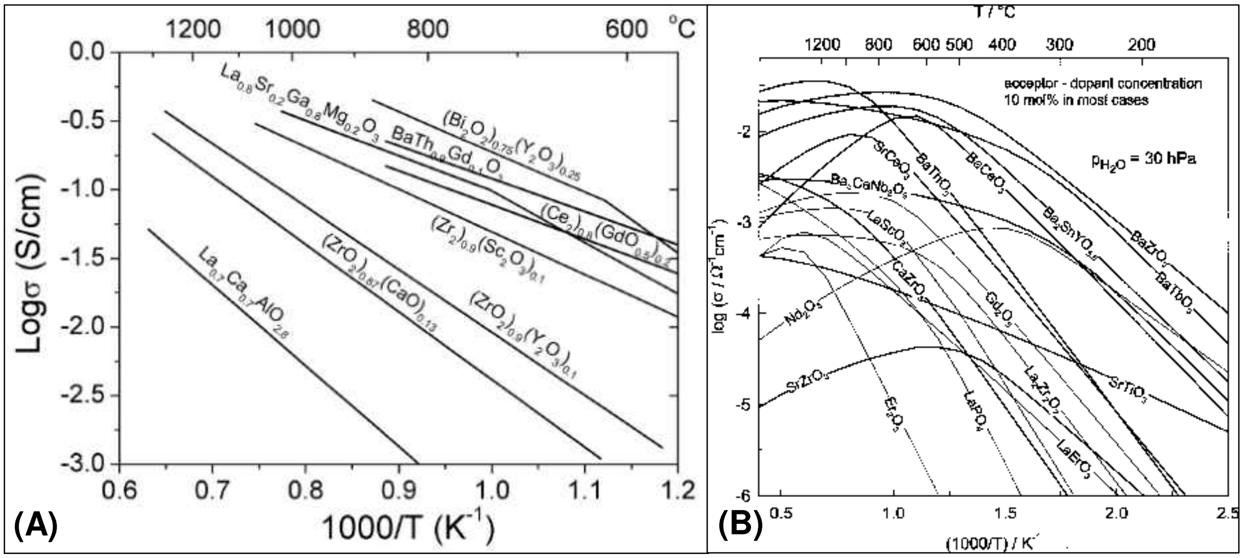

Figure 15: Ionic conductivities of electrolyte materials for SOFCs. (A) Ionic conductivities of O^{2-} conducting SOFC electrolytes [36]. (B) Ionic conductivities of proton conducting SOFC electrolytes [17].

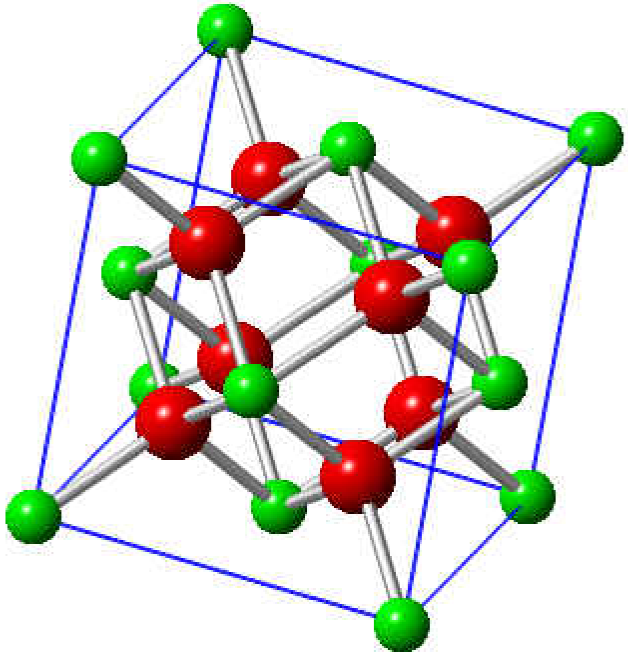

Figure 16: Fluorite oxide crystal structure. The cations (green) occupy the FCC positions, while the anions (red) occupy the tetrahedral sites [41].

Doping ZrO_2 with oxides of different vacancies can help stabilize the cubic and tetragonal crystal structure at lower temperatures. ZrO_2 can have a Fluorite crystal structure as seen in Figure 16 [41]. The attention on such oxide-ion conductors with a Fluorite structure heightened with the discovery of fast fluoride-ion conductivity observed in PbF_2 in 1839 by Michael Faraday [25]. There have been many oxides used to dope ZrO_2 like CaO, MgO, Gd_2O_3, Dy_2O_3, Sm_2O_3, Yb_2O_3, Nd_2O_3, Y_2O_3, Sc_2O_3. Two factors contribute significantly to the ionic conductivity of doped ZrO_2 at any given temperature – dopant concentration and ionic radius of the dopant cation. The closer the dopant cation radius is to the Zr^{4+} cation the higher the ionic conductivity. Zr^{4+} has a radius of 0.84Å. The dopant cation Sc^{3+} with a radius of 0.87Å results in the highest ionic conductivity of 0.1 Scm^{-1} at 800 ºC for ZrO_2 with 10 mol%. Sc_2O_3. For the same dopant concentration and at thesame temperature, the ionic conductivity is 0.03 Scm^{-1} when doped with Y_2O_3 given the radius of Y^{3+} cation is 1.02Å [42]. The dopant cation needs to have a lower valence compared to

Zr^{4+} cation (example: Y^{3+}, Sc^{3+}, and Yb^{3+}). In such a case, the drive to maintain charge neutrality of the lattice leads to anion (oxygen) vacancies. At first, as the dopant concentration increases so does the ionic conductivity resulting from the oxygen vacancies generated, but after a point there of the lattice leads to anion (oxygen) vacancies. At first, as the dopant concentration increases so does the ionic conductivity resulting from the oxygen vacancies generated, but after a point there is an optimal value reached and further addition of the dopant leads to lower ionic conductivity. With the concentration of Y_2O_3 in ZrO_2, up to 8 mol%, the ionic conductivity increases as the oxygen vacancies increase [38]. After that point, the conductivity starts to drop. It is proposed that right around 8 mol% of Y_2O_3 in ZrO_2 [8YSZ], there is a state of equilibrium reached between the increasing oxygen vacancies and the increase in electrostatic interactions between the O^{2-} anion vacancies and dopant Y^{3+} cations in the ZrO_2 lattice [43-45]. The phase diagram of Y_2O_3 doped ZrO_2 in Figure 17 shows the different phases present with the increasing concentration of Y_2O_3 in partially stabilized zirconia [46]. The tetragonal phase is supposed to exist when Y_2O_3 doping is 2-9 mol% and the cubic phase exists at Y_2O_3 concentration of 4-40% [47, 48]. Apart from Y_2O_3, there are other dopants that could be used in ZrO_2, mainly Sc_2O_3. Scandia stabilized zirconia is known for its high ionic conductivity. It has an ionic conductivity that surpasses that of 8YSZ. Doping Zirconia with 10 mol % of Scandia seems to be the most optimal.

Table 2. Doping of ZrO_2 and CeO_2 with divalent and trivalent dopants leads to solid electrolytes with oxygen vacancies and hence enhanced oxygen ionic conductivity. Adapted from [43]

	ZrO_2 (host material)	**CeO_2 (host material)**
Divalent dopant	$CaO \xrightarrow{ZrO_2} Ca''_{Zr} + O_O^x + V_O^{\cdot\cdot}$	$CaO \xrightarrow{CeO_2} Ca''_{Ce} + O_O^x + V_O^{\cdot\cdot}$
Trivalent dopant	$Y_2O_3 \xrightarrow{ZrO_2} 2Y'_{Zr} + 3O_O^x + V_O^{\cdot\cdot}$	$Gd_2O_3 \xrightarrow{CeO_2} 2Gd'_{Ce} + 3O_O^x + V_O^{\cdot\cdot}$

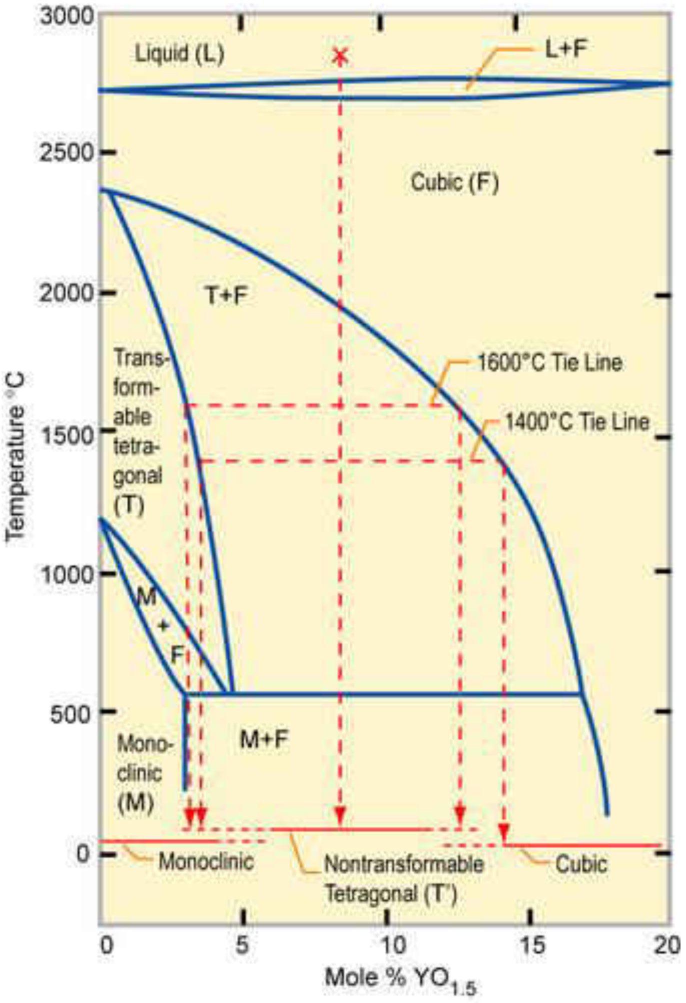

Figure 17: Phase Diagram of Partially Yttria Stabilized Zirconia [46]

1.4.4.1.1 Layered electrolyte design

To benefit from the favorable properties of both YSZ and SCSZ ceramics, a layered electrolyte design was proposed and produced by placing SCSZ layers sandwiched between thin outer YSZ layers as seen in the paper by Yan et al. [49]. The layered design of YSZ/SCSZ/YSZ electrolyte exploits the higher conductivity of SCSZ but at the same time the outer layers of YSZ protects the SCSZ layer/s since YSZ is more stable in the oxidizing and reducing conditions on either sides of the electrolyte. More about the design of these layered electrolytes will be covered in CHAPTER 2: MECHANICAL MODELING OF YSZ/SCSZ/YSZ LAYERED

ELECTROLYTES, but it is important to understand how this layered design affects the strength of the final electrolyte. Ho et al. [50] provide a great understanding and a way to calculate the residual stresses induced in the layers of the layered electrolyte. In this case, during the sintering process as YSZ and SCSZ layers are cooled from the sintering temperature (T_o) to a temperature (T) the difference in the coefficient of thermal expansion (CTE) of the two materials will result in a mismatch strain,

$$\varepsilon_m = \int_T^{T_o} (\alpha_2 - \alpha_1) dT$$

α_2 and α_1 being the CTE for the two materials. Now to be able to calculate the stresses in the layers, let's understand what stresses are involved. First, it is important to note that far from the free surface the residual stresses in the layers are biaxial and uniform in nature. The perpendicular stress far from the free surface becomes negligible i.e. $\sigma_z = 0$. If the thickness of the layers of each material in the stack is t_1 and t_2, then the residual biaxial stress in the layer with the lower value of CTE (σ_{R1}) and the residual biaxial stress in the layer with the higher value of CTE (σ_{R2}) given by,

$$\sigma_{R1} = -\frac{\varepsilon_m E_1'}{1+\frac{t_1 E_1'}{t_2 E_2'}} \quad \text{and} \quad \sigma_{R2} = -\sigma_{R1}\frac{t_1}{t_2}, \text{ where } E' = -\frac{E_1}{1-\upsilon_1}\varepsilon_m$$

E is the Young's modulus and υ is the Poisson's ratio. The layered electrolyte design also provides the feasibility to control thermal residual stresses in each layer which could bring improved strength, ionic conductivity and robustness. Thermal compressive residual stress can develop in materials with lower coefficient of thermal expansion (CTE), while thermal tensile residual stress can appear in materials with higher coefficient of thermal expansion. The values of the compressive and tensile residual stresses can be adjusted e.g. by controlling the thickness ratio of layers with compressive and tensile residual stresses [20]. The high compressive residual stress in the outer layers of a laminate will enhance the strength and apparent fracture toughness of laminates [21, 22], and it was also shown in numerous reports that the appearance of certain stress/strain states in the electrolyte improves the ionic conductivity of the material [23, 24]. The favorable benefits of layered electrolyte are the increase of electrolyte strength under bending loading, higher ionic conductivity in comparison with pure YSZ electrolyte, and improved phase stability and resistance to degradation in comparison with pure SCSZ electrolyte.

1.4.4.2. Cathode

The cathode in a SOFC is the electrode that facilitates the oxygen reduction reaction to occur. The cathode material needs to be able to conduct both electrons and ions, which calls for Mixed Ionic- Electronic Conductors (MIEC) materials. In a SOFC cathode, oxygen atoms are adsorbed from the gas flow channels, the oxygen atoms then combine with the incoming electrons to form oxygen ions that behave as the charge carriers. The cathode material has a number of desirable properties that can be summarized as [51]:

i. High ionic conductivity
ii. High catalytic activity to favor reduction reactions
iii. High electronic conductivity
iv. Maintain mechanical stability during thermal and mechanical load cycling
v. Have a CTE value close to that of other cell components
vi. Chemical stability in reducing environments
vii. Ease of fabrication and cost effective

The introduction of perovskite oxides as cathode materials set the scene in 1966 with the paper by Archer and Button, in which they proposed the use of strontium doped $LaCoO_3$ [52, 53]. A number of researchers continued to explore the use of different types of pure and doped perovskite oxides in SOFCs; like $LaCoO_3$, $LaMnO_3$, $LaFeO_3$, CeO_2, as shown in Figure 12. Like the other cell components, the cathode undergoes changes in its mechanical, chemical and other properties with the kind of thermal and mechanical cycling that the fuel cells are subjected to. Increase and decrease in temperature as the fuel cell starts up or shuts down respectively, can cause degradation or changes in mechanical properties like Young's modulus. Single fuel cells are stacked against other single cells, and this can cause the cell components to be subjected to compressive loading, leading to creep and fatigue. In some cases, the fuel cell maybe cathode-supported, this makes it even more crucial to study the mechanical behavior of the cathode material.

Doped versions of $LaCoO_3$ have been utilized as SOFC cathode material [54-56], but it has been widely studied for more than half a century due to its several unique properties [57-60]. $LaCoO_3$ is a perovskite that belongs to the family of materials that are ferroic in nature. It is a multiferroic material since it exhibits both ferroelastic and ferromagnetic behavior; more about this will be covered in the next two sections. $LaCoO_3$ has found applications in a number of fields based on its catalytic properties [61-63], mechanical properties [64-68], electrical properties [69, 70], and magnetic properties [71-73]. The ferroelastic behavior of $LaCoO_3$ was reported in the work of Orlovskaya et al. [74]. $LaCoO_3$ based materials have found use in oxygen separation due to its oxygen permeability [75-77].

1.4.4.2.1 Perovskites

The typical perovskite structure has the chemical formula of ABO_3, where A is the larger cation and B is the smaller cation. The B cation is 6-fold coordinated and the A cation is 12-fold coordinated with the oxygen anions [78]. The ideal perovskite structure is cubic, but different perovskites tend to have a distortion in their lattice and this could lead to ferroic material behavior. The size and nature of each element affects the final crystal structure and properties of the perovskite produced. The ionic radii ratio between A and B cations determines the stability and crystal group of the final perovskite.

Pure and doped $LaCoO_3$ have numerous energy applications, including SOFCs. $LaCoO_3$ has a perovskite structure as depicted in Figure 18 [79, 80]. The positions of La (A cation), Co (B cation), and oxygen anions in octahedral positions can be seen. The figure shown is for the paraleastic cubic unit cell of $LaCoO_3$. But below the transition temperature, $LaCoO_3$ maintains a rhombohedral structure that belongs to the $R\bar{3}c$ space group. Thornton et. al. [81, 82] showed that this rhombohedral structure is maintained between 4-1248 K. Kobayahsi et al. [83] in their work showed that $LaCoO_3$ transitions from rhombohedral to cubic structure at 1337 ^{o}C. The ferroelastic rhombohedral cell structure can have a hexagonal representation and is illustrated in Figure 19, adapted from [84]. For a rhombohedral unit cell, the cell lattice parameters include a_R and α_R (less than 60^{o}) and for a hexagonal representation a_H, c_H and α_H.

Lanthanum ions can be substituted with strontium ions or calcium ions in the A cation site. When such substitutions are made, the charge neutrality of the system needs to be maintained. The La ion is La^{3+} whereas Sr ion is Sr^{4+}, hence to maintain charge neutrality some oxygen ions leave the lattice, leading to oxygen vacancies in the lattice which in turn results in higher oxygen ion conductivity. This results in the formation of $La_{1-x}Sr_xCoO_{3-\delta}$, which is a popular SOFC cathode material.

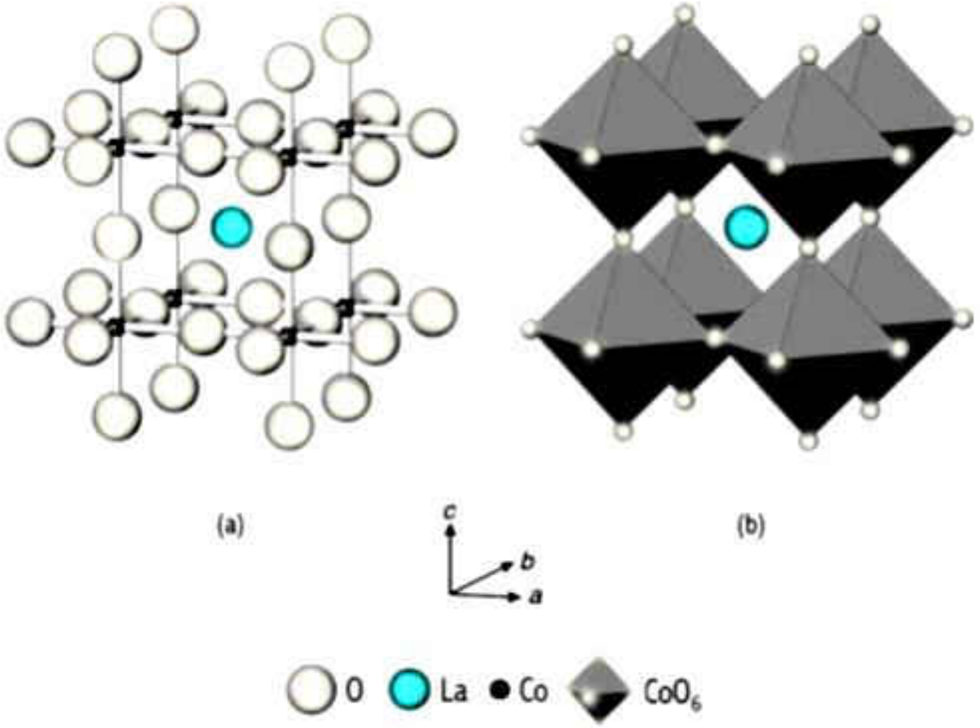

Figure 18: Perovskite structure of $LaCoO_3$ Part (a) of the figure shows the position of each atom in the unit cell – the A cation (La) occupies the central interstitial position; the B cation (Co) occupies the position in the center of the octahedral. Part (b) shows the CoO_6 octahedral structure which is formed at the 8 corners of the unit cell. [79, 80]

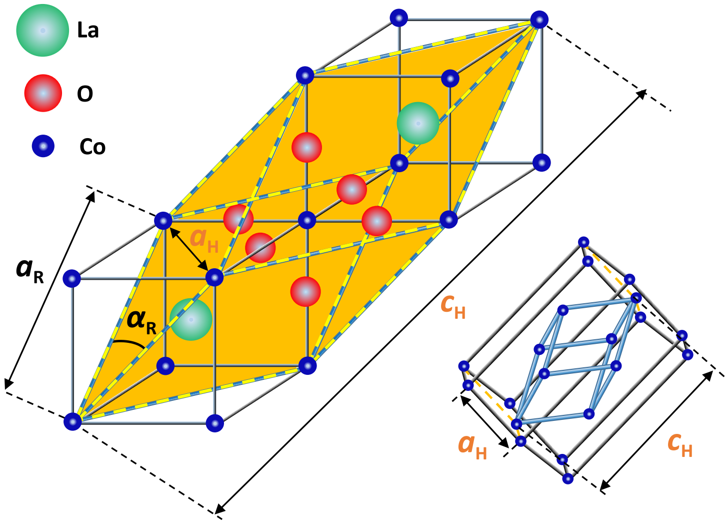

Figure 19: Ferroelastic rhombohedral unit cell $R\bar{3}c$ of $LaCoO_3$. The figure depicts the hexagonal represenation of the rhombohedral unit cell, and a comparison with paraelastic cubic unit cell

1.4.4.2.2 Ferroelastic materials

Ferroelastic materials are part of a group of materials called ‘ferroic’ materials. K. Aizu was the one who defined a ferroic material in his work in 1970 [85] as: “A crystal is provisionally referred to as being "ferroic" when it has two or more orientation states in the absence of magnetic field, electric field, and mechanical stress and can shift from one to another of these states by means of a magnetic field, an electric field, a mechanical stress, or a combination of these”. The ferroic materials group consists of ferroelectric, ferromagnetic and ferroelastic materials. The phenomenon of ferroelasticity is related to the temperature of the material. At temperatures higher than the critical temperature ($T > T_c$) the material is said to be paraelastic and achieves a high-symmetry phase [86]. Under this condition, there is a linear relationship between stress and strain response of the material. At temperatures lower than the critical temperature ($T < T_c$) the material is said to be ferroelastic and has a low symmetry phase and macroscopic spontaneous strain appears in the material even at zero stress. Figure 20 shows the ferroelastic transition of lanthanum cobaltite from cubic to rhombohedral structure with the decrease in temperature. During the transition from paraelastic phase to ferroelastic phase, twins/domains are developed which are responsible for the appearance of spontaneous strain. These twins or domains are basically states that are identical in the crystal structure but with different mechanical strain tensors at zero applied stress [87]. K. Aizu gave a definition of ferroelasticity [87] as: “A crystal is said to be ferroelastic, when it has two or more orientation states in the absence of mechanical stress and can be shifted from one to another of these states by a mechanical stress.” When stress is applied to such a twinned crystal, beyond a particular coercive stress value, one direction of the twins/domains remains stable and grows at the expense of the other directions. This process can be reversed if the direction of stress is reversed (compressive to tensile or vice versa), such that the second direction now remains stable and collapses into the first direction [88]. This process is called ferroelastic domain switching or reorientation and is related to texturing and formation of preferred orientation during application of stress, and this leads to strong anisotropy in elastic properties of the material [88]. This relationship between stress and strain in a ferroelastic material follows a specific pattern - a hysteresis loop (non-linear).

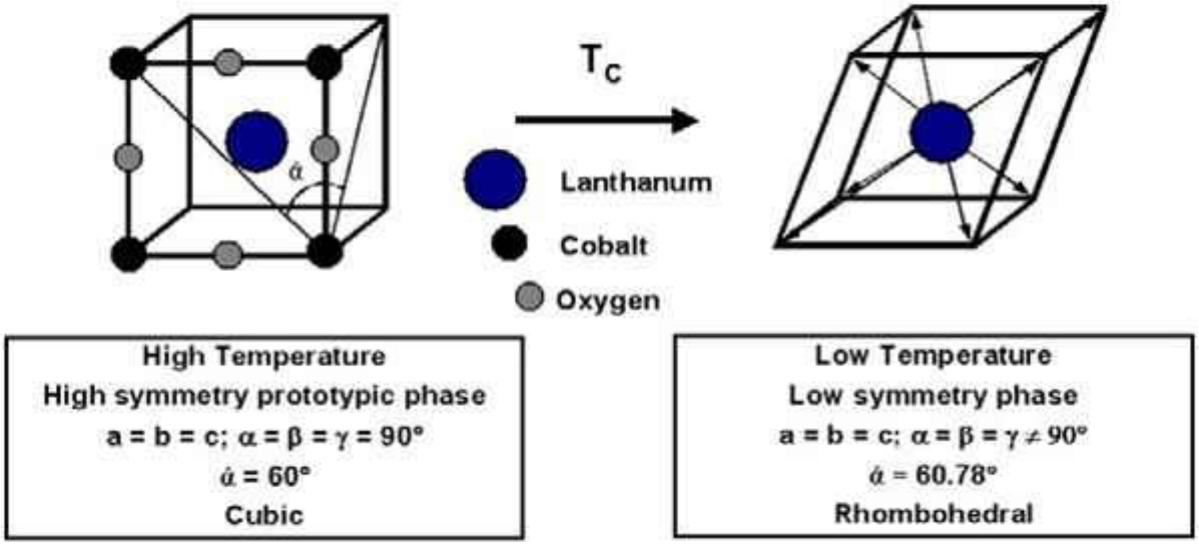

Figure 20. Cubic to rhombohedral ferroelastic phase transition in $LaCoO_3$ when temperature decreases ($T < T_c$) [87]

$LaCoO_3$ based perovskites have multiple applications, including being used as cathode material in solid oxide fuel cells. SOFCs operate at high temperatures (~800°C) and are subjected to thermal and mechanical loads during the cell operation. One of the key issues that needs to be resolved to commercialize SOFCs at a large scale includes the long term thermo-mechanical behavior of the cell's materials [89]. Hence, studies based on the thermo-mechanical behavior of $LaCoO_3$ based cobaltites will be covered in this work.

1.5. Renewable Energy Education

Given the current trend in the world, the renewable energy industry is only going to grow and dominate the energy sector. The goals of most countries, especially the ones part of the United Nations Framework Convention on Climate Change, are to reduce their dependence on fossil fuels and start relying on energy conversion that is more sustainable, economic and clean. As can be seen in Figure 1, the U.S. is focused on expanding on energy saving efforts and implementation of renewables [3]. Accordingly, the U.S. and other countries need to start focusing on educating the public on the different types of renewables and their relevant features/aspects. The end consumer needs to be made familiar and comfortable with the new or enhanced energy conversion and distribution systems/channels. An example of this could be the use of localized solar systems or micro-CHP fuel cell systems to provide localized power and heat, which would be a definite change from the centralized energy conversion and distribution system that most consumers are used to. Equally critical is educating the future workforce of this industry which may include engineers and scientists who will conduct research and development to elevate these technologies, as well as technicians and supporting staff who will carry out the implementation of renewables at a large scale.

Energy literacy is essential in any society, state or country. It is imperative that the decisions makers, policy makers, voters and the end consumers have a fundamental understanding of the different energy technologies. Educating them will give them the ability to understand and make important decisions regarding aspects like - the pros and cons of different options, why a certain renewable energy technology maybe be best for their geographical region, what are the financial investments needed for each technology and what the operating costs would look like, the impact of using a particular technology on the environment around them, whether they should opt for a centralized or decentralized energy conversion and distribution system, etc. One such example is the Task Force on Energy Supply formed in 2009 by the National Conference of State Legislatures. These meetings brought together the pertinent policymakers of all states with energy experts and with the use of the information about energy resources at their disposal; they were able to make decisions that would shape the energy scenario for the next 20 years of the nation. The task force had four meetings between December 2009 and May 2010, and one of the important outcomes of these meetings was a report that was prepared called Meeting the Energy Challenges of the Future: A Guide for Policymakers released in July 2010 [90]. To quote one of the statements in the executive summary of the document – *"Decisions made today will affect energy reliability, security, economic growth and the environment for decades to come. The importance of a functional and resilient electric grid was highlighted during the Northeast blackout of 2003, which left 50 million people without power due to system failure. To address these and other issues, the task force recognized the need for state legislators to have accurate information about energy supply and demand trends, along with knowledge of what new resources will be needed to ensure that production, distribution and delivery of electricity continues to be affordable and reliable"*. This clearly emphasizes the importance of energy literacy among policymakers and decision makers.

Figure 21. A young girl assembling a fuel cell car as part of a course in fuel cells [91]

The U.S. Department of Energy (DOE) is aware of the importance of energy education and has taken a lot of efforts in providing energy literacy. The DOE webpage [92] on energy education has energy, how to find a job in the renewable energy sector; and energy related lesson plans, labs and projects for K-12. A document called the Energy Literacy published by the DOE helps people of all ages understand energy concepts [91]. Figure 21 shows the picture from the guide of a young girl assembling a fuel cell car as part of a lesson on fuel cells. Figure 22 shows the Renewable Energy Competency Model published by CareerOneStop in conjunction with the Department of Energy. It is an interactive pyramid that helps a person find a job or provide a pathway for a career in the renewable energy sector [93].

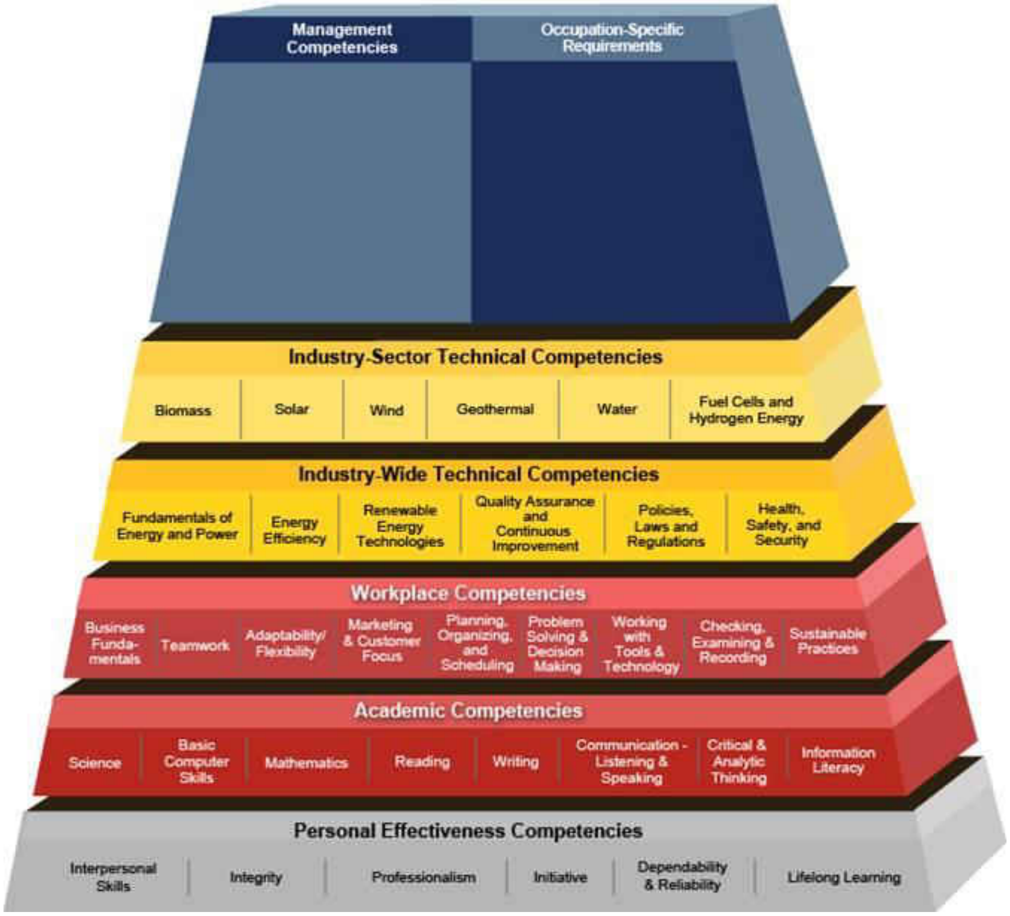

Figure 22. Renewable Energy Competency Model published by CareerOneStop in conjunction with the Department of Energy. It is an interactive pyramid that helps a person find a job or provide a pathway for a career in the renewable energy sector [93]

Kandpal and Broman have done a great job of summarizing the renewable energy educational efforts around the world in their paper [94]. They point out the fact that in the last three decades, a lot of countries around the world have put in efforts to develop renewable energy educational programs. These educational programs were initialized in many countries after the oil crisis in the 1970s. The educational efforts intensified and a lot more countries initialized such programs after the global climate change concerns surfaced in the 1990s [94-96]. Various educational programs have been implemented at different academic levels starting at middle school or high school all the way up to advanced graduate programs. The Florida Solar Energy Center for example offers a number of courses, activities and resources related to solar energy, hydrogen energy and other alternate energy technologies for students at the K-12 level, or university level or even in the form of continuing education [97]. In Sweden, a program called Public Understanding of Renewable Energy (PURE) was started to expand the knowledge of the public or end consumer as suggested by the name of the program [98]. At the North Carolina State, NSF sponsored a program called Future Renewable Electric Energy Delivery and Management (FREEDM) that offers many courses including Research Experience for Undergraduates [99]. These are only a handful of the myriads of programs offered around the globe but possibly we will soon reach the tipping point when most people in the world would become familiar with the renewable energy technologies. Now specifically talking about fuel cells, the fuel cell industry sales exceeded \$1.3 billion in 2014 [100]. According to one prediction, the fuel cell and hydrogen industry worldwide will grow to be a \$180 billion dollar industry by 2050 [101], and generate up to 180,000 job positions by 2020 [102].

To meet the employment demands of the fuel cell industry, educating the current and future generations of engineers and scientists in fuel cells has become of utter significance. Many educational institutions offer courses related to fuel cell or hydrogen technology [103, 104] as seen in Figure 23. Mostly the courses follow the conventional teaching style based on classrooms and books. Furthermore, very few present the educational contents in an inter-connected manner that brings together different perspectives on fuel cell systems.

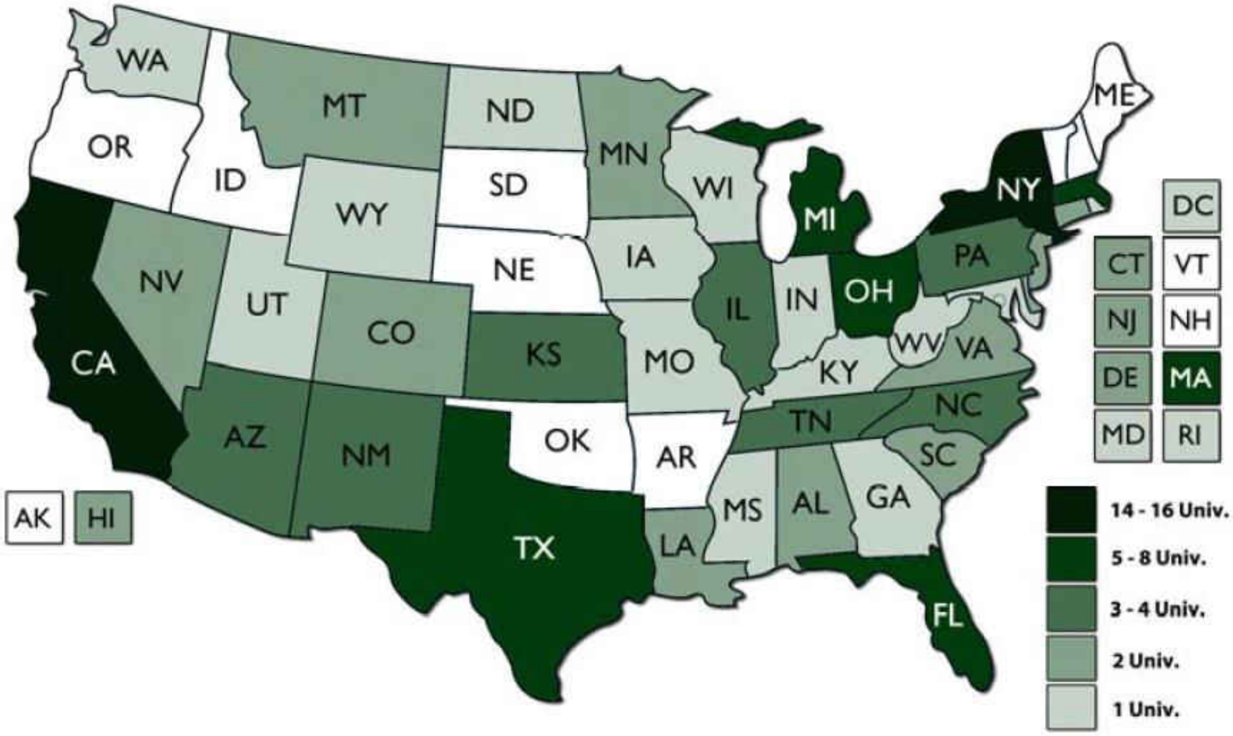

Figure 23. Universities around the country that offer courses related to fuel cells [100]

1.6. Goal of this work

The goal of this work includes the following:

I. Electrolyte: To develop a finite element model that can be used to calculate the residual stresses in layered electrolytes under biaxial loading. Due to their high oxygen ion conductivity and other desirable properties, yttria and scandia stabilized zirconia are the most commonly used electrolyte materials for SOFCs. A unique approach was taken to develop a layered electrolyte design, where 8 mol% Yttria (Y_2O_3) stabilized Zirconia (ZrO_2) [YSZ] and 10 mol% SC_2O_3-1 mol% CeO_2-ZrO_2 [SCSZ] electrolyte layers were combined to form layered electrolytes with the goal to enhance both ionic conductivity and mechanical stability. To measure the mechanical strength of these electrolytes, a standardized test for ceramics was used, called the ring-on-ring biaxial test to measure the biaxial flexure strength of the electrolytes. Finite Element Modeling (FEM) had to be used to calculate the stresses since the experiments carried out were outside the limitations of theoretical equations. In CHAPTER 2: MECHANICAL MODELING OF YSZ/SCSZ/YSZ LAYERED ELECTROLYTES, the modeling approach and the results from the biaxial strength testing will be presented and discussed.

II. Cathode: Pure and doped $LaCoO_3$ can be as cathode material in SOFCs, sensors, catalysis and in oxygen separation. $LaCoO_3$ has received a lot of attention due to properties like ferroelasticity, ferromagnetism, oxygen ion conductivity, mixed ionic and electronic conductivity, catalytic activity and creep behavior. In this work, the experimental details and results of three major experiments related to $LaCoO_3$ will be covered in

III. CHAPTER 3: STUDY OF LaCoO3 AND La0.8Ca0.2CoO3 AS POSSIBLE CATHODE MATERIAL. First, the ferroelastic behavior of $LaCoO_3$ under uniaxial compression will be studied using *in-situ* neutron diffraction. Second, the elastic properties of $LaCoO_3$ will be derived at room temperature using *in-situ* neutron diffraction. Finally, the structural and mechanical behavior of $LaCoO_3$ will be studied at high temperatures using *in-situ* neutron diffraction, X-ray diffraction and Raman Spectroscopy.

IV. Fuel cell educational software: Lastly in CHAPTER 4: FUEL CELL EDUCATIONAL SOFTWARE, the design, development and evaluation of an educational software to teach undergraduate students about fuel cell technology will be presented. The software is designed to be interactive and the different components of the software are inter-connected. The educational content is presented in the form of animations, videos, and text. The purpose of the software is to serve as a supplemental tool used in fuel cell or renewable energy courses, or to get students acquainted with the major aspects of fuel cells. Evaluations were conducted in undergraduate engineering courses at the University of Central Florida.

CHAPTER 2: MECHANICAL MODELING OF YSZ/SCSZ/YSZ LAYERED ELECTROLYTES

2.1. Electrolyte design

The majority of the content of this chapter is published in a paper co-authored by the author [105].

YSZ is the most explored and used electrolyte material for high temperature SOFCs and it is a material of choice for numerous SOFC applications. While YSZ has good ionic conductivity at 1000°C, at lower operational temperatures the ionic conductivity decreases and ohmic losses increase [2]. SCSZ is a better choice for the electrolyte material, as it exhibits much higher ionic conductivity at lower operational temperatures [3], but it exhibits cubic to rhombohedral phase transition which affects both the electrolyte and overall cell performance [4, 5]. In addition SCSZ is more sensitive to the poisoning by impurities present in the fuel [6], which is why any exposure to the anode side could affect its long term operation. This leads to structural instability as well as higher sensitivity to impurities of the SCSZ electrolyte, which degrades the SOFC performance.

Therefore, to utilize the favorable properties of YSZ and SCSZ, a layered electrolyte design has been adopted. The idea of the layered electrolyte design is to place thin YSZ electrolyte layers on the outer surfaces of thin SCSZ electrolyte layers and varying the assembly configuration. Each single layer of YSZ and SCSZ material is a circular disk with a radius of 10mm and a thickness of 30μm. A total of nine electrolyte designs were considered in this research Figure 24. These were 3-, 4- and 6-layered designs using only YSZ or only SCSZ layers stacked one upon the other as well as laminate designs consisting of 1YSZ/2SCSZ/1YSZ, 1YSZ/2SCSZ/1YSZ and 1YSZ/4SCSZ/1YSZ layers [Figure 24]. For the laminate YSZ/xSCSZ/YSZ designs the volume fraction of each of the layers is different which would affect the ionic conductivities of the assembled electrolytes. Besides, as the coefficient of thermal expansion, Young's modulus and Poisson ratios of YSZ and SCSZ slightly differ [106, 107], the appearance of thermal residual stresses in different layers is expected which might increase robustness and mechanical strength of the layered electrolytes. The nine electrolyte designs were produced and tested for ionic conductivity. The design and manufacturing of the layered electrolytes were all carried out by Dr. Yan Chen [49, 108]. The ionic conductivity testing was carried out at the University of South Carolina, by Dr. Xinyu Huang and his research group. Figure 25 shows the ionic conductivity after testing of the five main designs.

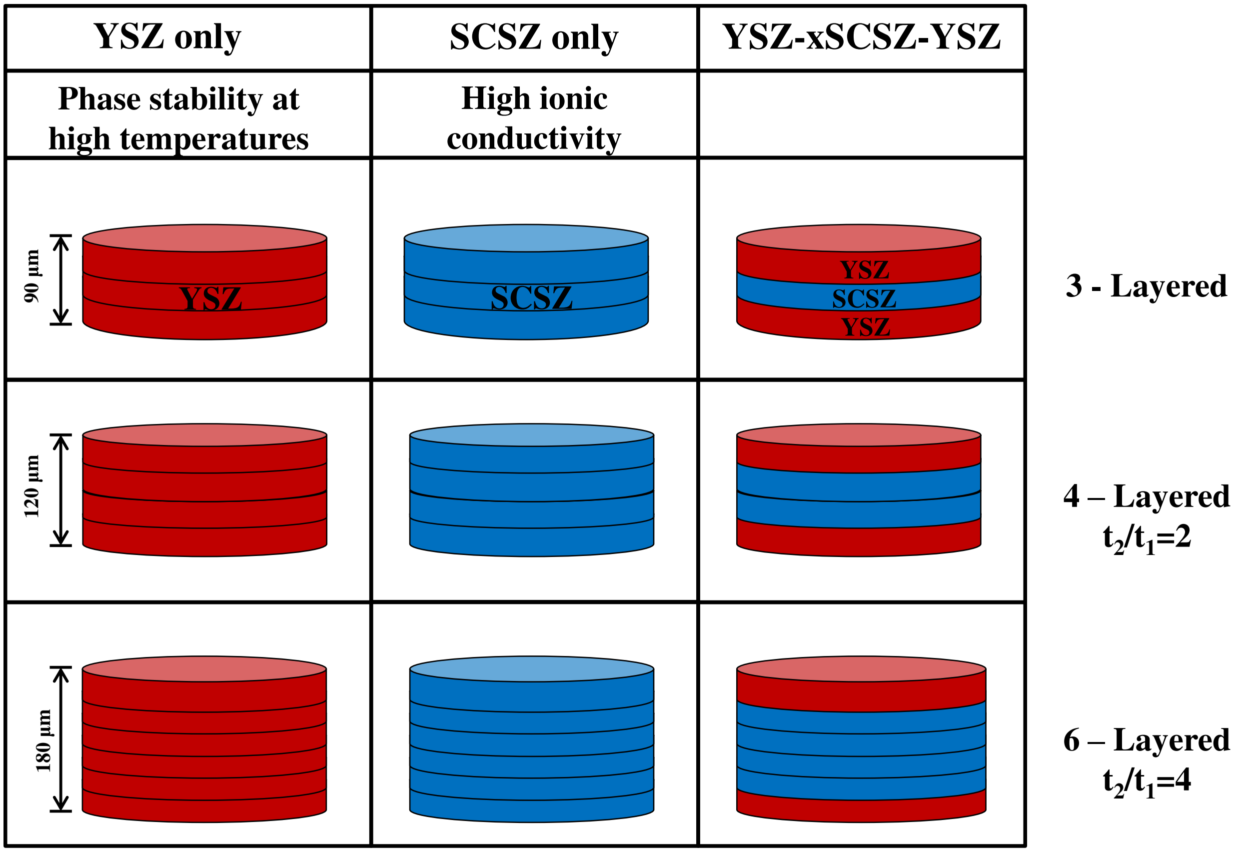

Figure 24.Electrolyte designs [49, 108, 109]

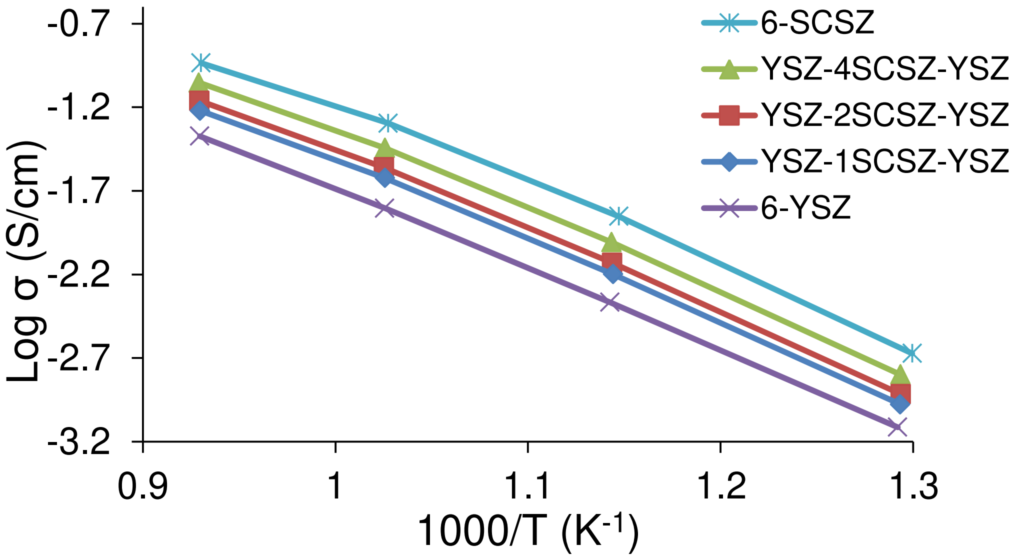

Figure 25: Ionic conductivity of electrolytes [49, 108, 109]

2.2. Mechanical modeling

The simple plate theory does not provide a way of calculating stresses in the electrolyte when the deflection of the electrolyte is beyond that of its own thickness and stress has a non-linear behavior. For this purpose, finite element modeling (FEM) could be used. The FEM software that was employed was COMSOL Multiphysics® 4.3a version with the Structural Mechanics module. The whole modeling process was carried out in COMSOL. To simplify the problem, a 2D axisymmetric model of the electrolyte was developed. The loading and support rings have a line contact with the specimen and in 2D were approximated as distributed point loads. The number of mesh elements was approximately 23000. The non-linear behavior of stresses was accounted for with a feature in COMSOL called Geometric Nonlinearity [110, 111]. This concept can be explained with the help of Figure 26. Consider the beam in the Figure 26 undergoing a large deformation. Particularly notice the infinitesimal cubic element shown at the end of the beam. The beam deforms and along with it the cubic element undergoes stretching, translation and rotation. Also, as it can be seen in the figure, that after deformation the edges of the cube are no longer orthogonal. To solve the problem in FEM, it would be simpler to use two different coordinate systems by combining the Lagrangian and the Eulerian approach. The displacement field of every particle in the solid is defined with components u, v and w, which are defined with respect to a reference frame, **X** = (X, Y, Z). The value of u, v and w describes the displacement of the point relative to its original position. This reference frame **X** is the Lagrangian frame and can also be called the material frame. As the solid deforms, the material frame becomes a non-orthogonal curvilinear coordinate system. A strain tensor called the Green-Lagrangian strain or material strain, ε_{ij}, can be evaluated by taking the derivative of u, v, w with respect to X, Y, Z. As can be seen in the figure, after deformation the three mutually perpendicular edges of the cube are no longer perpendicular and hence a deformed frame called the Eulerian or spatial frame, **x** = (x, y, z), can be defined.

The material or Lagrangian frame **X** is used in all the formulations. This means that the stress, strain and material properties are evaluated with reference to the material configuration, rather than to the spatially varying Eulerian frame **x**. This way the material properties need to evaluated only once for the initial material configuration. To compute strain, consider a particle initially located at $\mathbf{x} = \mathbf{X}$. As the beam deforms the particle is displaced by a magnitude **u** and the new position is given by

$$\mathbf{x} = \mathbf{X} + \mathbf{u}(\mathbf{X}) \tag{1}$$

The line element (one edge) of the infinitesimal cube *d***X** can be mapped to the deformed frame as line element *d***x** and the deformation gradient *F* can be introduced from

$$d\mathbf{x} = \frac{\partial \mathbf{x}}{\partial \mathbf{X}} d\mathbf{X} = \tilde{\mathbf{F}} d\mathbf{X} \tag{2}$$

The deformation gradient tensor F_{ij} accounts for both the material and spatial frames and contains all the information regarding the local deformation of the material. It can be expressed in terms of displacement gradient and identity tensor $\tilde{\mathbf{I}}$, as

$$\tilde{\mathbf{F}} = \nabla \mathbf{u} + \tilde{\mathbf{I}} \tag{3}$$

where

$$\nabla\mathbf{u} = \begin{bmatrix} \frac{\partial u}{\partial X} & \frac{\partial u}{\partial Y} & \frac{\partial u}{\partial Z} \\ \frac{\partial v}{\partial X} & \frac{\partial v}{\partial Y} & \frac{\partial v}{\partial Z} \\ \frac{\partial w}{\partial X} & \frac{\partial w}{\partial Y} & \frac{\partial w}{\partial Z} \end{bmatrix} \text{ and } \tilde{\mathbf{I}} = \begin{bmatrix} 1 & 0 & 0 \\ 0 & 1 & 0 \\ 0 & 0 & 1 \end{bmatrix} \quad [4]$$

The strain is calculated as Green-Lagrangian strain tensor,

$$\tilde{\boldsymbol{\varepsilon}} = \frac{1}{2}\left[(\nabla\mathbf{u})^T + \nabla\mathbf{u} + (\nabla\mathbf{u})^T \nabla\mathbf{u}\right] \quad [5]$$

The stress tensor in the Eulerian frame called the Cauchy or true stress $\tilde{\boldsymbol{\sigma}}$ is easy to define and represents all of the forces that act on a volume element. The stress tensor in the Lagrangian frame can be computed by performing a transformation on the Cauchy stress tensor $\tilde{\boldsymbol{\sigma}}$. This transformation introduces another stress tensor known as second Picola-Kirchoff stress tensor $\tilde{\mathbf{S}}$. Whereas the Cauchy stress tensor relates the forces in the Eulerian frame to the areas in the Eulerian frame, the second Picola-Kirchoff stress tensor relates the forces in the Lagrangian frame to the areas in the Lagrangian frame. The stress tensor can then be expressed as

$$\tilde{\boldsymbol{\sigma}} = J^{-1}\tilde{\mathbf{F}}\tilde{\mathbf{S}}(\tilde{\mathbf{F}})^T \quad [6]$$

where $J = dV / dV_0 = \det(\tilde{\mathbf{F}})$ is the ratio between the current and initial volume, for incompressible material, $J = 1$.

The stress and strain tensors are connected by Hooke's law

$$\tilde{\boldsymbol{\sigma}} = \tilde{\mathbf{C}} : \tilde{\boldsymbol{\varepsilon}} \quad [7]$$

where $\tilde{\mathbf{C}}$ is the 4th order elasticity tensor and ":" stands for double-dot tensor product.

The computation is based on the principle of virtual work which states that under equilibrium condition, the total virtual work from internal strains and stresses is equal to work from external loads. In FEM the body is discretized into many finite elements, and the total virtual work done can be calculated as the sum of virtual works of all these elements.

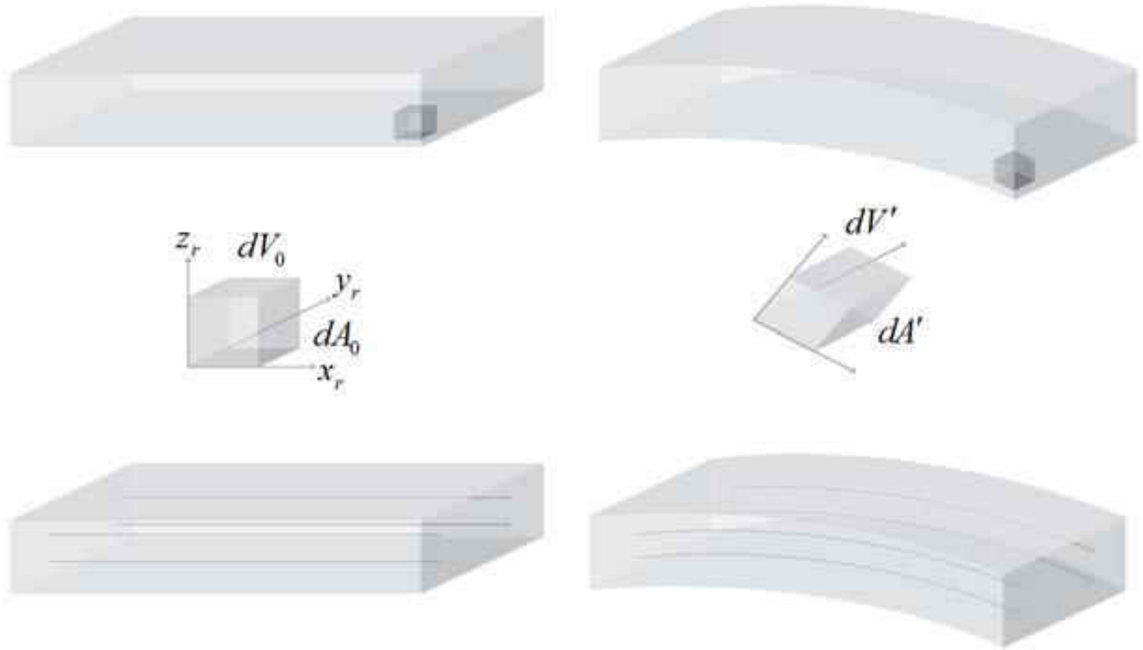

Figure 26: Deformation of a beam. The figures to the left show the undeformed state of the beam and the figures to the right shows the deformed state of the beam. The top figures show the infinitesimal cube at the end of the beam, the center figures show the cubic element before and after deformation and the bottom figures shows lines in the beam parallel to the neutral axis.

2.3. Biaxial strength

2.3.1. Experimental procedure

The biaxial strength testing is crucial for testing electrolytes that are used in electrolyte-supported designs. Two and four layers of SCSZ $[(Sc_2O_3)_{0.1}(CeO_2)_{0.01}\text{-}(ZrO_2)_{0.89}]$ were "sandwiched" between two layers of YSZ [$(Y_2O_3)_{0.08}(ZrO_2)_{0.92}$] to produce 4-layered (Y-2SC-Y) and 6-layered (Y-4SC-Y) electrolytes. The thickness of each layer was designed to be approximately 30μm. Figure 24 shows the design of the layered electrolytes. To perform a comparative study, electrolytes made of pure SCSZ and pure YSZ were produced with the same 4-layered (4SCSZ or 4YSZ) and 6-layered (6SCSZ or 6YSZ) design. The manufacturing procedure of these electrolytes and the microstructural characteristics of the materials are presented in [49].

To study the thermal expansion of YSZ and SCSZ cylindrical specimens of 6mm diameter and 12 mm length were used. These specimens had been uniaxial pressed at 20 MPa, then sintered at 1500ºC for 5 hours to densify. The heating and cooling rate to raise the specimen temperature from room temperature (RT) to 1000ºC and vice versa was 5ºC/min in air. A pushrod dilatometer NETZSCH DIL 402C was used to study the linear thermal expansion of the materials during heating. The possible error in linear expansion measurement is ±1.25nm. The equation to calculate the CTE (α) is

$$\alpha = \frac{1}{L}\frac{dL}{dT} \qquad [8]$$

where L is the length of the specimen at room temperature, T is the temperature. The linear dependency of CTE as a function of time was obtained by taking the time derivative of an approximated second order polynomial $dL/L=AT^2+BT+C$.

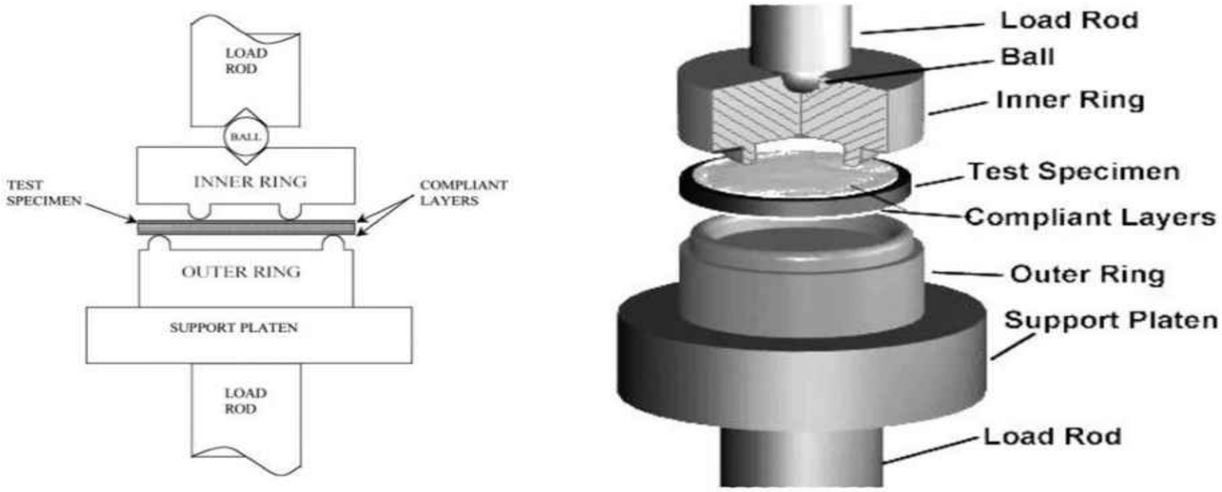

Figure 27. Schematic of a standardized ring-on-ring test following the ASTM C-1499 standard [112]

Figure 28. Photograph of the actual instrument used to carry out the ring-on-ring testing [105, 108]

The standard ring-on-ring testing used for measuring the biaxial flexure strength of ceramics [112] was used to estimate the biaxial strength of the multilayered electrolytes, as seen in Figure 27 and Figure 28. The testing was carried out at Empa, Switzerland, by Dr. Yan Chen [105, 108]. The testing was carried out at RT and at 800°C. The electrolytes produced had a varied thickness of 110-200µm [49]. For testing at RT, the electrolyte specimens of approximately 36mm diameter were loaded between a support ring of 30mm diameter and a concentric loading ring of 12mm diameter. For testing at 800ºC, the electrolyte specimens with an approximate diameter of 31mm were loaded between a support ring of 25mm diameter and a concentric loading ring of 12.5mm diameter. The loading rate (in terms of displacement rate) used for testing at both temperatures was 1.5mm/min constant crosshead displacement rate. The loading and support rings of the room temperature jig are made out of hardened steel and the high temperature jig out of Al_2O_3. The friction between the specimen and the rings are considered to be minimal and hence the friction effect is neglected. For the testing at high temperature (i.e. 800ºC) the specimen were first placed between the loading and support rings and then temperature of the assembly was raised to 800ºC in a furnace, at a heating rate of 2ºC/min. Before testing began, a dwell time of 1 hour was given to allow for a homogeneous temperature distribution in the furnace.

The ring-on-ring test follows the ASTM standard C1499-09. The equation provided that relates load and stress in a linear fashion is given as

$$\sigma_f = \frac{3F}{2\pi t}\left[(1-\nu)\frac{D_S^2 - D_L^2}{2D^2} + (1+\nu)\ln\left(\frac{D_S}{D_L}\right)\right] \qquad [9]$$

where σ_f is the maximum flexure stress, F is the load at fracture, t is the thickness of the specimen, υ is the Poisson's ratio; D_s, D_L and D are the diameter of the support ring, loading ring and the specimen. The linear relationship between load and stress in Equation [2] is only valid when the following conditions are satisfied [112-114]:

$$\frac{D_S}{10} \geq t \geq \sqrt{\frac{2\sigma_f D_S^2}{3E}}, \qquad D - D_S \geq 2t, \qquad \frac{t}{\delta} > 2 \qquad [10]$$

where E is the Young's modulus of the specimen and δ is the maximum deflection at the center of the specimen. When any of the conditions listed above in Equation [3] is not satisfied, as in the case of our experiment the deflection is way higher (δ > t/2 [25]) then a non-linear relationship between is observed [115], and equation [2] is not valid anymore, as presented in Figure 29. Therefore the use of finite element modeling (FEM) is needed to predict and calculate the biaxial stress at a given load.

The numerical modeling to calculate biaxial strength of the specimen was carried out using COMSOL Multiphysics® 4.3a version with the Structural mechanics module. A 2-D axisymmetric model was adopted to minimize computational time and cost. COMSOL Multiphysics was particularly useful in the simulation because it has a feature called geometric non-linearity [116, 117], which helps account for the non-linear behavior of stresses in the material. An unstructured mesh with triangular elements was used to fill the geometry with a total of approximately 23,000 elements. To validate the model, first it was shown that the calculations from the model comply with equation [2] when the conditions in equation [3] were satisfied. The FEM model was further verified by using the same model to solve problems shown in other works [118, 119], the results matched very well.

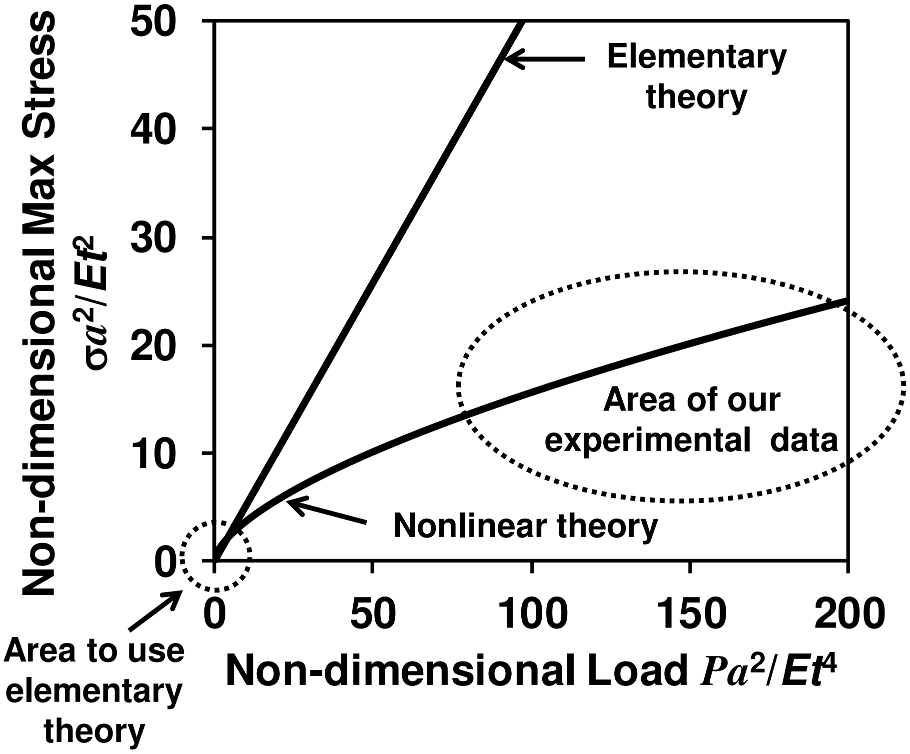

Figure 29. Advantage of using FEM for the calculation of biaxial flexure strength

2.3.2. Results and Discussion

Based on the measurements using the dilatometer, thermal expansion of SCSZ and YSZ from RT to 1000°C are plotted in Figure 30A. As it can be observed, owing to similar fluorite crystal structure of the two materials the difference in thermal expansion between the two materials is quite small. This difference becomes more distinguishable when the CTE is calculated and plotted as seen in Figure 30B. The CTE of SCSZ is lower than that of YSZ below 600°C. The slope of the line of CTE versus temperature for SCSZ is higher than that of YSZ (solid lines), and the CTE value of SCSZ is higher than YSZ beyond 600°C. The experiment was conducted for a maximum temperature of 1000°C, hence a linear extrapolation (dashed lines) had to be done to estimate the CTE at sintering temperature of 1550ºC of the electrolytes. As a way to validate the CTE measurements in this work, the measured averaged CTE value between 25 and 1000°C for YSZ is 10.58×10^{-6} K^{-1} which is in excellent agreement with the averaged CTE value of 10.5×10^{-6} K^{-1} as shown in [120] for the same temperature range. At the temperature range of 300-500ºC, SCSZ undergoes a phase transition cubic-rhombohedral-cubic but this transition requires a considerable amount of time ≈ 12 hours. The heating rate in the experiment from RT to 100ºC is 5ºC/min, which means that the effects of the phase transition may not be seen to reflect on the CTE value. Also to further validate this assumption, it can be seen that the curve of CTE versus temperature plot has an excellent agreement with a second order polynomial (smooth monotonic function) for the whole range of temperature from RT to 1000ºC.

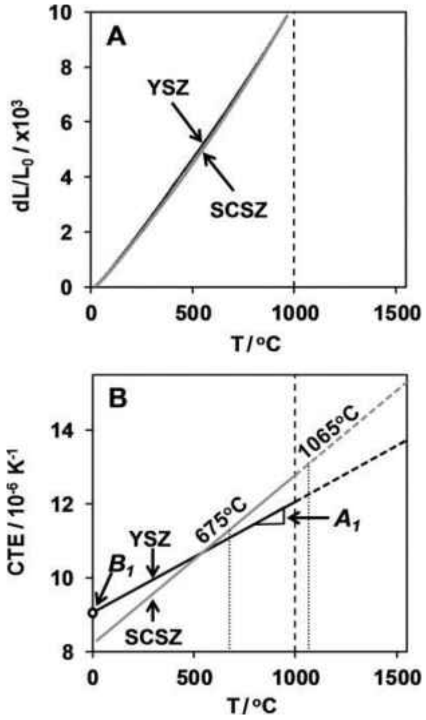

Figure 30. (A) Thermal expansion data of YSZ and SCSZ in the temperature of 20ºC and 1000ºC (B) The values of coefficient of thermal expansion for YSZ and SCSZ. The derived values from experimental data is shown as solid lines, whereas the dashed lines show the linear extrapolation for the temperature range 1000-1550ºC

In order to understand the thermal residual stresses occurring in the layers of the electrolyte, the concept of high thermal compressive stresses and low tensile thermal stress was used [50]. The methodology to calculate thermal residual stresses was adopted from [121]. In each electrolyte layer, the thermal strain and elastic strain add up to give the total strain. The residual stresses in the layers of a two-component material with symmetrical structure, in case of a perfectly rigid bonding, are [122]:

$$\sigma_{r1} = \frac{E_1' E_2' f_2 (\alpha_2 - \alpha_1)\Delta T}{E_1' f_1 + E_2' f_2} \qquad [11]$$

$$\sigma_{r2} = \frac{E_1' E_2' f_1 (\alpha_1 - \alpha_2)\Delta T}{E_1' f_1 + E_2' f_2} \qquad [12]$$

where $E_j' = E_j/(1-\nu_j)$, $f_j = (N+1)t_j/(2t)$, E_j and ν_j is the elastic modulus and Poisson's ratio of *j*-th component, t_j are the thickness of layers of *j*-th component, respectively, α_1 and α_2 are the thermal expansion coefficients of the first and second components, respectively, $\Delta T = T - T_{join}$ is the difference between the current temperature T and the joining temperature T_{join}, and t is the total thickness of the specimen. If α_1 and α_2 are the linear functions of temperature then,

$$(\alpha_1 - \alpha_2)\Delta T = \int_{T_{join}}^{T} (\alpha_1(T) - \alpha_2(T))dT = \left[\left(A_1 \frac{T + T_{join}}{2} + B_1\right) - \left(A_2 \frac{T + T_{join}}{2} + B_2\right)\right]\Delta T \qquad [13]$$

where $\alpha_1(T) = A_1 T + B_1$ and $\alpha_2(T) = A_2 T + B_2$. Hence,

$$(\alpha_1 - \alpha_2)\Delta T = [\alpha_1(<T>) - \alpha_2(<T>)]\Delta T \qquad [14]$$

where $<T>=\frac{T+T_{join}}{2}$ is the average temperature in temperature range from T to T_{join}. Therefore, both values of ΔT and <T> need to be known to arrive at the thermal residual stresses in the layers. Since the biaxial strength measurements were done at room temperature and 800ºC, the thermal residual stresses need to be calculated at these two temperatures. The joining temperature is not known, but the joining temperatures will have to lie between the sintering temperature of 1550ºC and 1200ºC, because creep in YSZ is quite significant above 1200ºC. The joining temperature is hence adjusted based on the biaxial strength and the material strength, and T_{join} = 1330ºC seems to have a good correlation between calculated and experimental values. Then, for room temperature experiments ΔT = –1310°C and <T> = 675°C, and for testing at 800°C ΔT = –530 °C and <T> = 1065 °C. Using these parameters as well as the electrolytes' dimensions (Table 3) the materials' properties (Table 4) the values of in-plane residual stresses calculated using Equations (4) and (5) are presented in Table 5. Figure 31 shows the plot of residual stress [MPa] versus the thickness ratio (t_2/t_1) between the layers. It can be seen that from both RT and 800ºC, as the (t_2/t_1) ratio increases from (t_2/t_1) tends to 0 to (t_2/t_1) = 4, thermal tensile stress in the inner SCSZ layer decreases while the thermal compressive residual stress in the outer YSZ layer increases. For example as shown in Figure 31A at RT, the value of thermal residual compressive stresses in YSZ ranges from 0MPa at (t_2/t_1) tends to 0, to 28MPa at (t_2/t_1) = 4. For the same conditions the value of thermal residual tensile stresses in SCSZ ranges from 42.5MPa at (t_2/t_1) tends to 0, to 14MPa at (t_2/t_1) = 4. As the average <T> is higher and CTEs difference between layers is also larger at 800 °C testing temperature, the values of residual stresses in SCSZ and YSZ layers differ more significantly for tests at 800 °C (Figure 31B).

Table 3. Thicknesses of layers in different designs.

Design	Thickness of YSZ layer t_1, μm	Thickness of SCSZ layer t_2, μm
Y-2SC-Y	30.7 ± 3.0	61.4 ± 5.5
Y-4SC-Y	30.7 ± 3.0	122.8 ± 10.0

Table 4. Material properties

	YSZ (*j*=1)	SCSZ (*j*=2)
Elastic modulus, GPa (room temperature)	202	207
Elastic modulus, GPa (800°C)	137	158
Poisson's ratio	0.31	0.31
A_j, 10^{-6} K^{-2}	3.01 x 10^{-9}	4.58 x 10^{-9}
B_j, 10^{-6} K^{-1}	9.05 x 10^{-6}	8.2 x 10^{-6}

Table 5. Residual stresses and calculated strength in layered electrolytes

From experimental CTEs		Y-2SC-Y	Y-4SC-Y
Room Temperature	Compressive residual stress in YSZ layer, MPa	-21	-28
	Tensile residual stress in SCSZ layer, MPa	21	14
	Calculated biaxial strength, MPa	203	210
800°C	Compressive residual stress in YSZ layer, MPa	-41	-53
	Tensile residual stress in SCSZ layer, MPa	41	26.5
	Calculated biaxial strength, MPa	145	157

2.3.2. Biaxial strength

The standard ring-on-ring testing was used to measure the biaxial strength of the electrolytes, where the circular electrolyte specimen is loaded between a support ring and a loading ring.

Figure 32A shows the load [N] versus testing time [s] plot, and includes two examples of fracture at low load (blue line) and fracture at high load (red line). Figure 32B & Figure 32C shows the fractured specimen at low load, while Figure 32D & Figure 32E shows the fractured specimen at high load. It is evident from the photographs that the specimen fractures into larger number of pieces at high load while it fractures into smaller number of pieces at low load. Finite element modeling using COMSOL was used to simulate the ring-on-ring testing and hence to calculate the biaxial strength or critical stress corresponding to the load at failure. Figure 33 shows a picture of the model. The initial position of the specimen and the load ring is shown as a wire mesh. As the displacement of the load ring and in turn the load increase, tensile stress appears at the bottom of the specimen. The stress value varies from zero to the highest value below the load ring. From the FEM model the biaxial strength of the electrolyte is calculated without accounting for the thermal residual stresses. The actual biaxial strength of the electrolyte accounting for the thermal residual stresses is given by maximum stress at the outer layer minus the corresponding calculated residual stress in the layer. Compressive residual stress (negative value) will increase the effective strength of the laminate. The plots of biaxial strength versus thickness ratios for room temperature and 800ºC is shown in Figure 34. At $(t_2/t_1) = 0$ the biaxial strength of pure YSZ and SCSZ electrolytes are shown. The strength of the Y-2SC-Y and Y-4SC-Y electrolytes is higher than that of the pure YSZ or SCSZ electrolyte; this proves that the presence of compressive stresses on the outer YSZ layer of these electrolytes improves the biaxial strength. This effect of thermal residual stresses contributing to the biaxial strength is more prominent at higher temperatures (800ºC) compared to room temperature. Also, to be noted is that the biaxial strength values are higher at room temperature in comparison to high temperature.

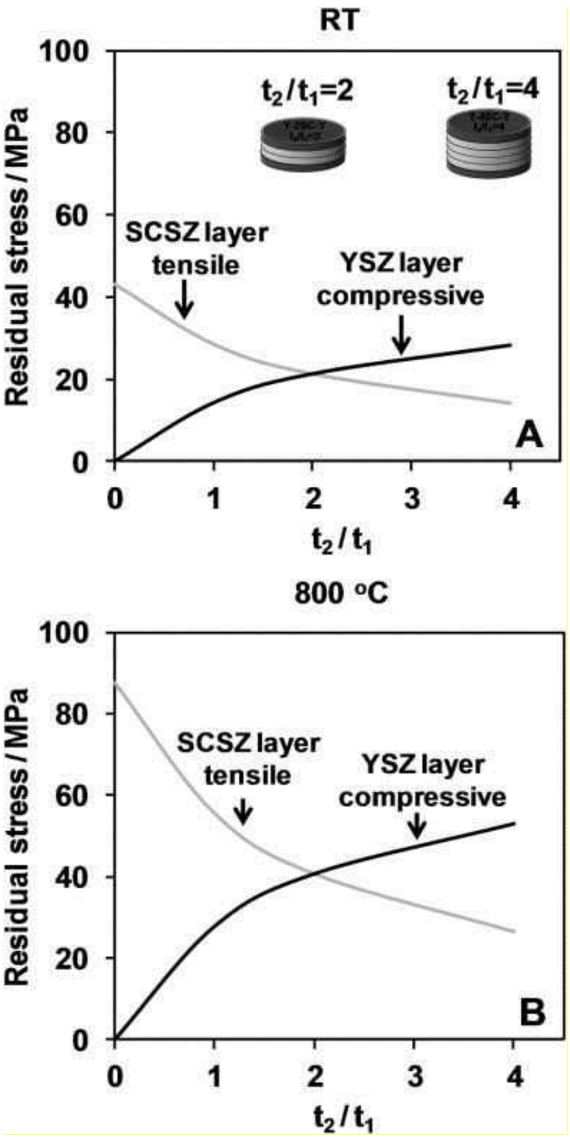

Figure 31. Residual stresses calculated for room temperature (A) and 800°C (B)

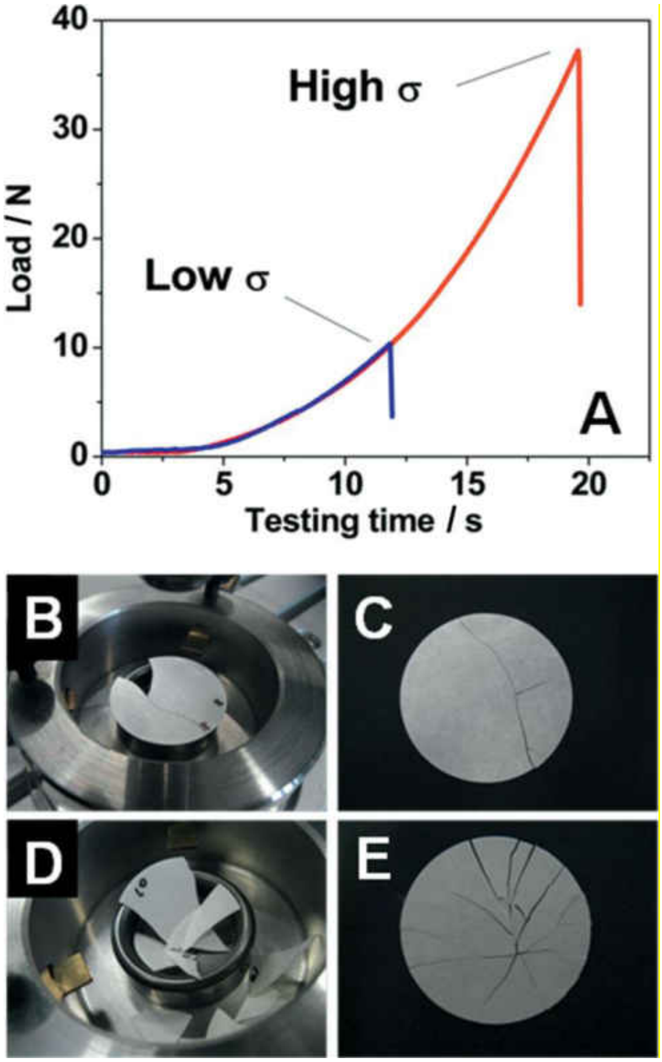

Figure 32. (A) The behavior or load with time is plotted; this data was used in calculating biaxial strength. (B, C) Some electrolytes fractured at relatively lower loads and only broke into a few pieces while (D, E) some electrolyte specimen fractured at relatively higher loads and broke into numerous pieces

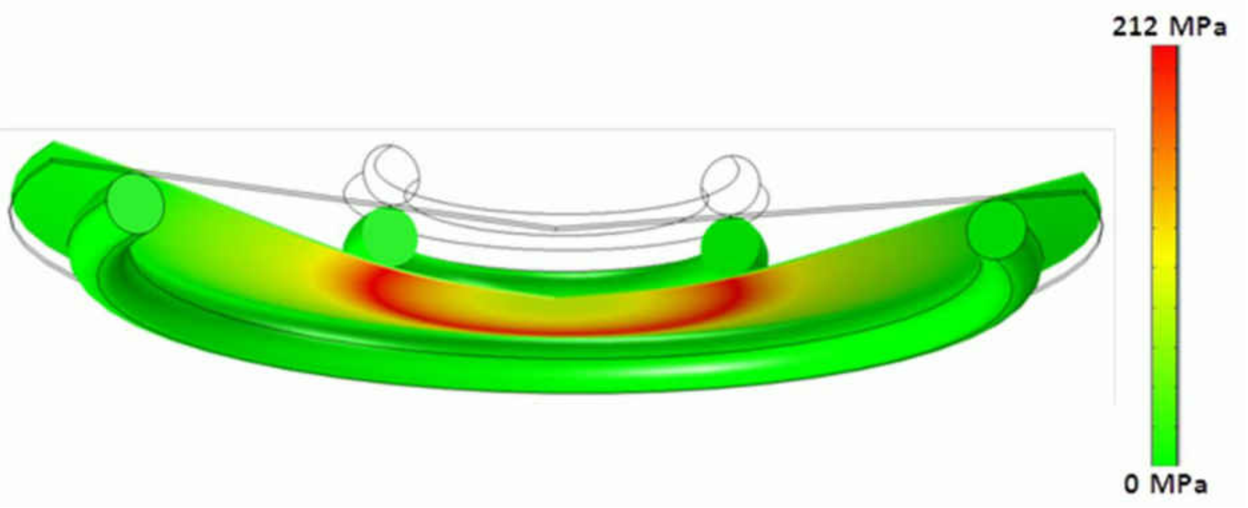

Figure 33. Biaxial flexure strength testing model developed in COMSOL

2.3.3. Conclusion

The purpose of this work was to provide an understanding of the relationship between thermal residual stresses on the biaxial strength of YSZ/SCSZ/YSZ electrolytes for use in Intermediate temperature Solid Oxide Fuel Cells. The electrolytes were designed such that the compressive residual stresses that would appear on the outer YSZ layers, would contribute to an increase in the biaxial strength of the electrolyte. This approach was validated as seen from the results, which shows that the biaxial strength of Y-2SC-Y and Y-4SC-Y electrolytes was higher than that of pure 4YSZ or 6SCSZ electrolytes. The presence of compressive residual stresses contributes to an increase in the biaxial strength of the electrolytes both at room temperature and at 800^{o}C, and the effect of thermal residual stresses seems to be more pronounced at higher temperatures. An excellent correlation between measured and calculated biaxial strength was obtained when the joining temperature was estimated to be equal to 1330^{o}C.

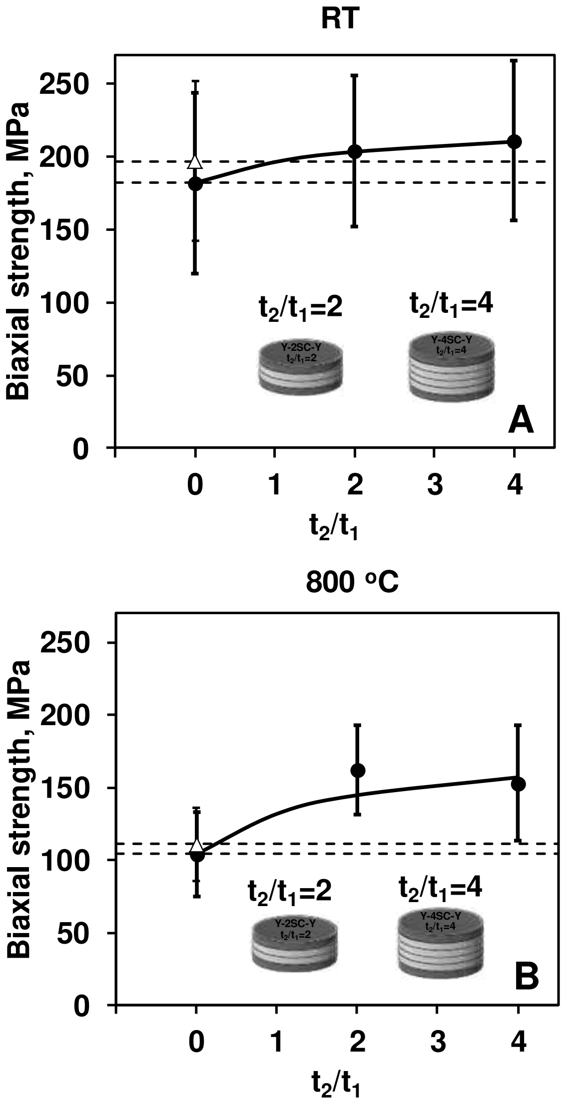

Figure 34. The biaxial strength as a function of the thickness ratio of layered electrolytes at room temperature (A) and 800°C (B). (●: experimental data of biaxial strength for electrolytes where YSZ is an outer layer; Δ: experimental data of biaxial strength of pure SCSZ electrolytes)

CHAPTER 3: STUDY OF $LaCoO_3$ AND $La_{0.8}Ca_{0.2}CoO_3$ AS POSSIBLE CATHODE MATERIAL

3.1. Experimental facility

Figure 35. Spallation Neutron Source at Oak Ridge National Laboratory, Oak Ridge, Tennessee

The neutron diffraction study was conducted at Spallation Neutron Source, Oak Ridge National Laboratory, Oak Ridge, Tennessee. Oak Ridge National Laboratory (ORNL) was established in 1943 as part of the Manhattan project during World War II. After the war, it evolved into a unique and significant research facility with diverse research areas such as energy, biology, engineering, chemistry, physics, environmental and social sciences. With an operating budget of about $1.6 billion it is currently being managed for the U. S. Department of Energy by UT-Battelle, LLC. ORNL has two outstanding neutron scattering facilities - Spallation Neutron Source (SNS) and High Flux Isotope Reactor (HFIR), which are available to researchers and scientists around the world to conduct a vast variety of experiments. SNS (Figure 35) is a one-of-a-kind research facility that provides the most intense pulsed neutron beams in the world for scientific research and industrial development [123]. In fact it holds the Guinness world record for the most powerful pulsed spallation neutron source in the world, by using a proton beam to strike a mercury target with more than 300 kW of energy, it is able to produce 4.8×10^{16} neutrons per second [124]. An ion source produces negatively charged hydrogen ions; these ions are accelerated and passed through a foil to strip of the two electrons which results in protons. These high energy protons are collected and in a ring and released in pulses to strike a mercury target. The process known as spallation releases neutrons from the target. These neutrons are then directed through different beamlines to specialized instruments designed for specific experiments. SNS has 13 instruments available to users around the world, each instrument providing a unique experimental setup. The instrument used for experimentation in this section is called VULCAN. VULCAN is designed for applications in materials science and engineering. They key capabilities of this instrument include the *in-situ* study of crystal structure for amorphous/crystalline materials, stress development, texturing, phase formation, creep behavior, temperature distribution, microstructure change, and residual stress development. It provides load frames, battery chargers, furnaces and other auxiliary equipment, which can be integrated to the experimental setup for in-situ and time-resolved measurements.

3.2. Crystal structure and texture development in $LaCoO_3$

The majority of the content of this section of the chapter is published in a paper co-authored by the author [67].

To study the ferroelastic behavior of $LaCoO_3$ and $La_{0.8}Ca_{0.2}CoO_3$, an experiment was designed such that the samples of these materials were subjected to three cycles of uniaxial loading (and unloading). The macroscopic stress-strain hysteresis curve would reveal a lot of information regarding the materials' properties. Using neutron diffraction technique while the material is subjected to these conditions would help gain knowledge in the evolution of the crystal structure and texture development in the material. Therefore an *in-situ* neutron diffraction study of $LaCoO_3$ and $La_{0.8}Ca_{0.2}CoO_3$ under uniaxial compression was carried out. The following sections will discuss the experimental procedure and the results from the experiment.

3.2.1. Experimental procedure

Pure polycrystalline $LaCoO_3$ samples for the experiment were produced by Praxair Surface Technologies, Specialty Ceramics. The samples were then machined by PermaTech Ceramics to produce cylinders of 6 mm diameter and 12 mm length. The average grain size of the sample was measured to be 2-5μm and the porosity 4%. It was ascertained by neutron diffraction that no secondary phase was identified in the sample. The setup of the experiment at VULCAN for the uniaxial compression is shown in Figure 36. The $LaCoO_3$ sample is loaded between two platens to undergo uniaxial compression. A neutron beam is incident on the sample and in-situ neutron diffraction study can be conducted as the compressive stress on the sample is varied. An extensometer with a gauge length of 9 mm is used to measure macroscopic strain. Three thermocouples (Type K, Omega Engineering) are used to measure the temperature of the sample surface, platen surface and air in the laboratory environment; and water recirculation was utilized to prevent any transfer of thermal energy from the machine to the sample. As the diffracted neutrons are recorded, a diffraction pattern with a d-spacing bandwidth of 0.5 to 2.5 Å is measured, by running a double-disk chopper at 30 Hz speed with a nominal 800 kW power source level. The two detector banks at -90^{o} (Bank 1) and $+90^{o}$ (Bank 2) record the neutrons diffracted by any (hkl) crystal planes with the normal parallel to Q1 and Q2 directions [125, 126]. The neutron diffraction measurements were carried out in the High Intensity (HI) mode with the instrument resolution at 0.45%. An incident beam slit dimensions were 5 mm in width and 3 mm in height, and a pair of 5 mm collimators were used together resulting in a 75 mm^3 gauge volume. Each neutron that is collected carries a time stamp based on the event-based data acquisition mode [127], the data collection is continuous while the sample is under loading. The sample was subjected to two cycles of loading in the load control mode. In the first cycle, a loading rate of -1.3 MPa/min was used until -200 MPa and then a loading rate of -7 MPa/min (kept constant hereafter) was used until a maximum stress value of -900 MPa, followed by unloading until -5 MPa. In the second cycle the sample was loaded to a maximum -700 MPa and unloading up to -5 MPa. The data collection lasted 675 min and 5 min data slicing (run) was chosen based on diffraction statistics, resulting in a total of 135 diffraction patterns (runs). The data analysis namely – chopping (data slicing), binning (allotting each sliced data set to a run – total of 135 runs), single peak fitting and other analysis, was performed using the VDRIVE (VULCAN Data Reduction and Interactive Visualization Software for Event Mode Neutron Diffraction) software [128].

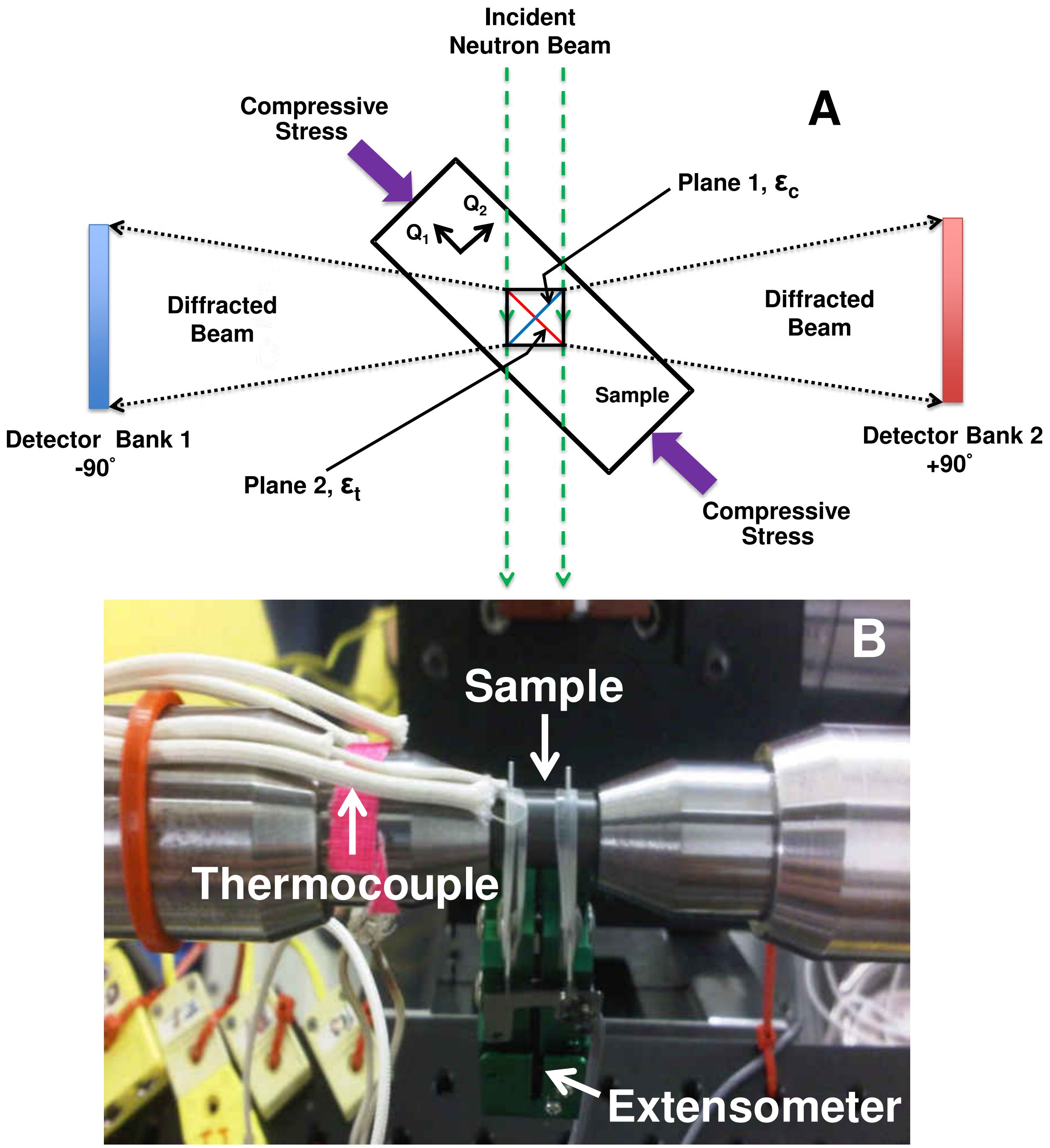

Figure 36: Experimental setup for *in-situ* neutron diffraction of sample under uniaxial compression. (A) Neutron beam is incident on the sample under compression. The two detector banks record the diffracted neutrons. Plane 1 undergoes compressive deformation while plane 2 undergoes tensile deformation. (B) Photograph shows $LaCoO_3$ sample loaded between two platens. An extensometer is used to measure macroscopic strain. Three thermocouples are used to measure temperature of the sample surface, platen surface and the air in the laboratory.

3.2.2. Evolution of crystal lattice under uniaxial compression

3.2.2.1. Macroscopic stress strain results

The stress versus time and the corresponding macroscopic strain versus time plots from the uniaxial compression of $LaCoO_3$ sample are presented in Figure 37 (A). Figure 37 (B) shows the temperature variation of the sample surface, platen surface and air in the laboratory environment. Since the temperatures remain constant with slight variation – air a little short of 23 ^{o}C, sample and platen at 19 ^{o}C, it can be concluded that there was negligible or no transfer of thermal energy from the testing machine to the sample. From Figure 37 (A) one can see that the stress varies linearly with time as expected, the strain however has a non-linear trend which is an indication of the ferroelastic behavior of the sample. Using the stress and strain versus time data, stress versus strain plots of the first and second loading/unloading cycles were made as can be seen in Figure 38. The ferroelastic hysteresis behavior of $LaCoO_3$ can be observed, this is in accordance with previously reported works [65, 66]. The coercive stress, at which the domain switching phenomenon begins, is calculated at 68 MPa. For the first cycle [Figure 38 (A)], the maximum strain at maximum stress of 900 MPa is 0.012, the hysteresis area is computed as 0.79 MPa, the non-recoverable/irreversible strain is equal to 0.0035 and the Young's modulus estimated at the beginning of loading is 76 GPa. This value of Young's modulus is close to the values reported in previous work using other technologies [66]. But when the material is loaded at the maximum stress value of 900 MPa, at the unloading curve, a significant increase in Young's modulus was observed with the value equal to 194 GPa. The hysteresis area in the second cycle [Figure 38 (B)] is equal to 0.12 MPa, which very low compared to the hysteresis area in the first cycle. The Important observation to make is that the loading curve in the second cycle coincides with the unloading curve of the first cycle, which means that in the second cycle there is no non-recoverable/irreversible strain present. The coercive stress and the Young's modulus at the beginning of second loading cannot be determined in a sensible manner, but the Young's modulus at the beginning of second unloading (at maximum compressive stress value of 700 MPa) can be calculated as 184 GPa. Table 6 summarizes these findings below.

The significant jump in the value of Young's modulus at the beginning of unloading in both cycles needs some explanation, but there has been no papers published that report the variation of Young's modulus with applied load; and only a few papers have report the value of Young's modulus for $LaCoO_3$ [66, 129, 130]. One possible explanation of the variation of Young's modulus with applied load could be the formation of preferred crystallographic orientation and the appearance of texture. The following sections will attempt to justify this possibility.

3.2.2.2 Changes in crystallographic orientation

The diffraction collected during the duration of the experiment (675 minutes) corresponds to the rhombohedral space group, $R\overline{3}c$, and the presence of secondary phases or monoclinic distortion can be ruled out. The diffraction pattern collected over the entire spectrum is plotted in Figure 39, at the beginning of loading (A, B) and at the highest 900 MPa applied stress (C, D), with the (*hkl*) interplanar distances subjected to radial compressive strain (Bank 1 – loading direction) (A, C) and the (*hkl*) interplanar distances subjected to lateral tensile strain (Bank 2 – transversal direction) (B, D). The diffraction pattern collected by Bank 1 (A, C) and Bank 2 (B, D) at the beginning of loading shows that the material is isotropic and identical for both banks. However as loading began, different preferred orientations of domains started to appear under the effect of axial compressive stress and the phenomenon of domain switching became very apparent; certain peak intensities started to grow at the expense of others while some peak intensities decreased up to the point of complete disappearance. Such strong texture development and formation of preferred orientations results in the development of anisotropic elastic properties and could be the cause of the large variation in Young's modulus of $LaCoO_3$ with varying applied load. The study could be narrowed down to a few peaks that demonstrated the strongest variations/changes: doublet (006)/(202), doublet (220)/(208) and the single peak (024).

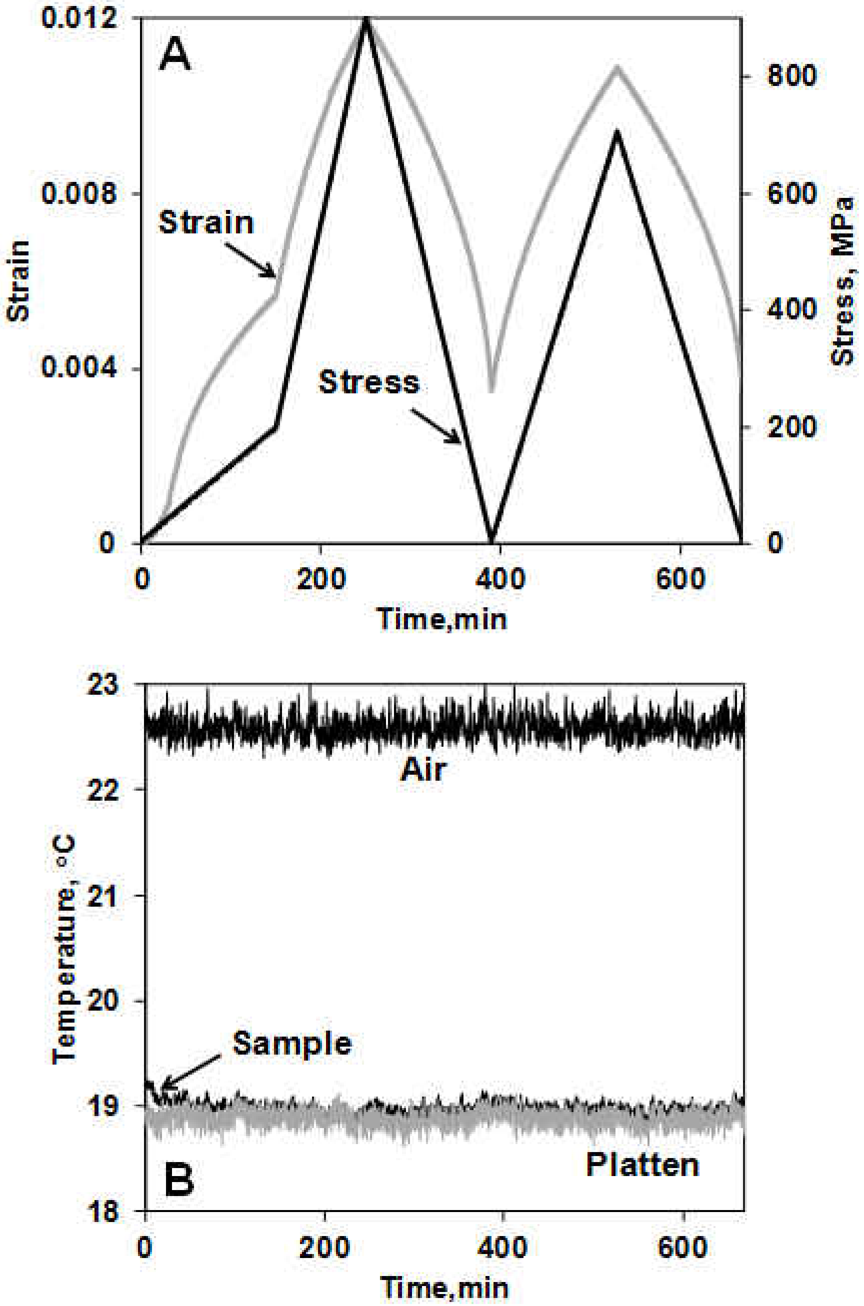

Figure 37: (A) Stress versus time and macroscopic strain versus time plots for the first and second loading/unloading cycles of the sample. (B) Temperature versus time plots for the sample surface, platen surface and the air in the laboratory environment

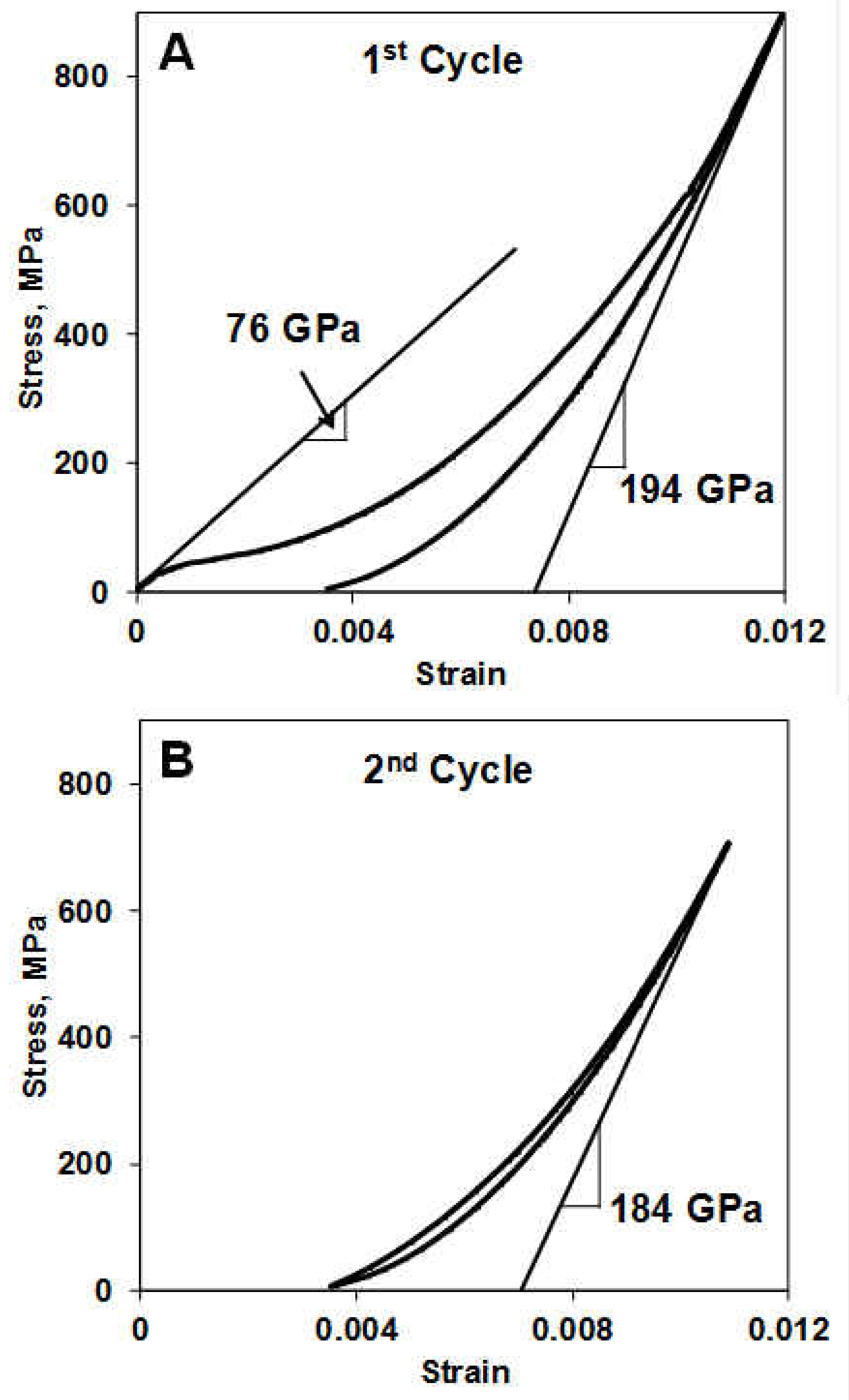

Figure 38 Stress-strain plots of sample for (A) first loading/unloading cycle, large hysteresis loop with non-recoverable strain (B) second loading/unloading cycle, with smaller hysteresis loop and the absence of non-recoverable strain

Table 6: Summary of findings from stress-strain deformation plots of sample for first and second loading/unloading

Parameter	**Value**
Coercive stress, MPa	68
Total maximum strain achieved at 900 MPa maximum stress	0.012
Irreversible strain	0.0035
1st Cycle	
Hysteresis area, MPa	0.79
Young’s modulus at the very beginning of the loading, GPa	76
Young’s modulus measured at the beginning of the unloading curve at 900 MPa applied stress, GPa	194
2nd Cycle	
Hysteresis area	0.12
Young’s modulus measured at the beginning of the unloading curve at 700 MPa applied stress, GPa	184 GPa

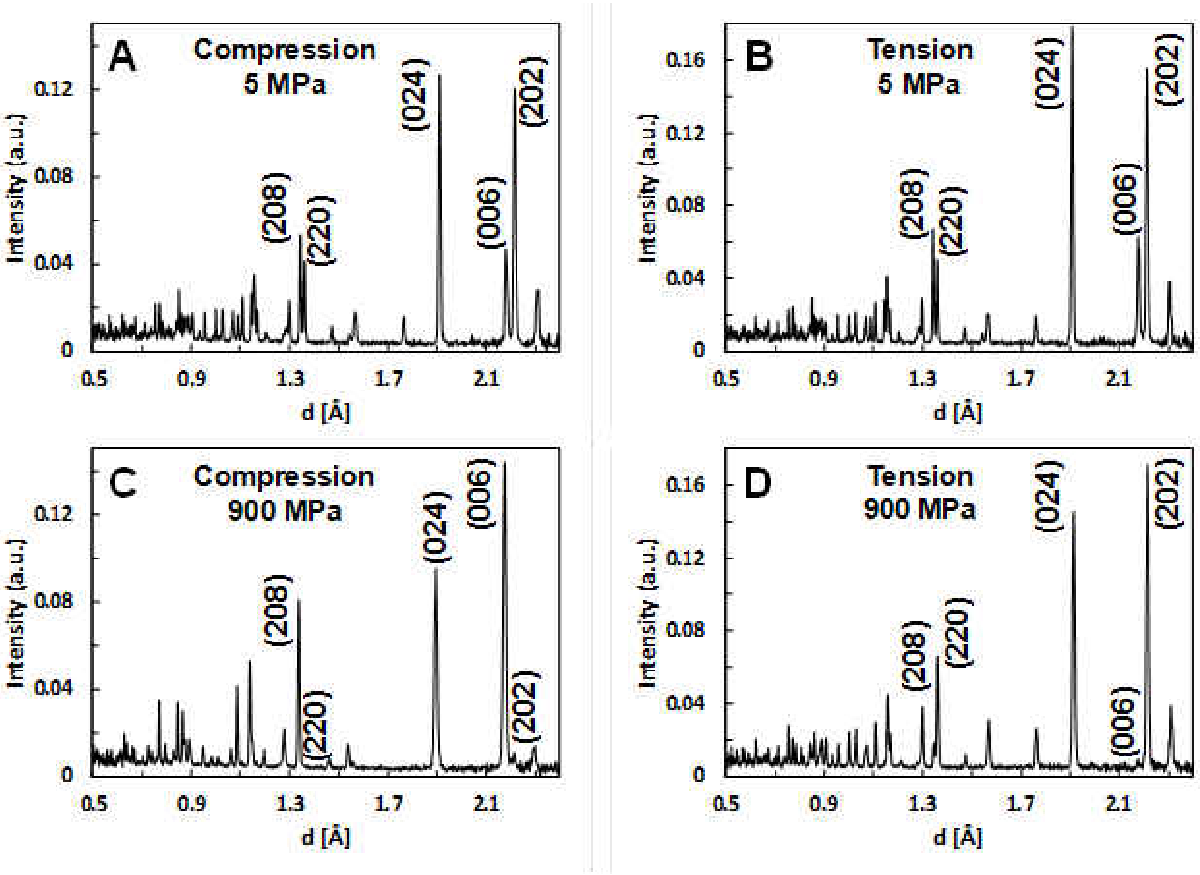

Figure 39: Diffraction pattern collected at the beginning of loading (A, B) and the maximum 900 MPa stress value of first cycle (C, D); collected by Bank 1 (A, C) and Bank 2 (B, D)

3.2.2.3. Study of single peak (024) as a function of applied load

Figure 40 presents the peak profiles of the (024) single peak as collected by Bank 1 (A) and Bank 2 (B). The peak profiles are the beginning of loading (5 MPa) and at the maximum stress value (900MPa) for the first cycle are superimposed to make a comparison. At the high stress value, the peak shifts to lower interplanar spacing, lowers in intensity and broadens under the compressive strain as captured by detector 1 (A, C). Under tensile strain as captured by detector 2 (B, D), at high stress the peak shifts to higher interplanar spacing, lowers in intensity and broadens. Part (C) and (D) of Figure 40 shows a 2-d presentation of the (024) peak position as a function of applied stress for both the first and second cycles of loading and unloading. From part (C) of the figure it can be seen that the (024) peak shifts to the lower interplanar spacing when subjected to compressive strain upon first loading, until the maximum applied stress (900 MPa) and during first unloading the peak shifts back to a higher interplanar spacing. For the second loading similar pattern of shift to lower interplanar spacing is observed until the maximum stress value (700 MPa), and the peak recovers back the higher interplanar spacing upon unloading. The radial compressive deformation which appears parallel to the applied load (Bank 1) causes the (024) peak to shift to lower interplanar spacing, while the tensile strain which appears in the transversal direction perpendicular to the applied load (Bank 2) causes the (024) peak to move to higher interplanar spacing. Figure 41 presents the intensity of the peak accounted for as peak height, full width at half maximum (FWHM) and area, as a function of applied stress for both first and second loading/unloading cycles; parts (A, C, E) as measured by Bank 1 and parts (B, D, F) as measured

by Bank 2. The peak height, FWHM and area are all normalized with respect to the initial peak intensity. As it can be noticed in Figure 41 (E, F) the area of the peak remains constant throughout the loading/unloading process, therefore the change in FWHM and peak height is conserved through the loading/unloading process. The constant peak area means that the volume fraction of (024) crystal planes in the particular direction remains constant during the loading/unloading process. Since the peaks broaden as the load increases it is possible that new domains appear in $LaCoO_3$, but as the load is reduced the FWHM returns to original value and these domains then disappear.

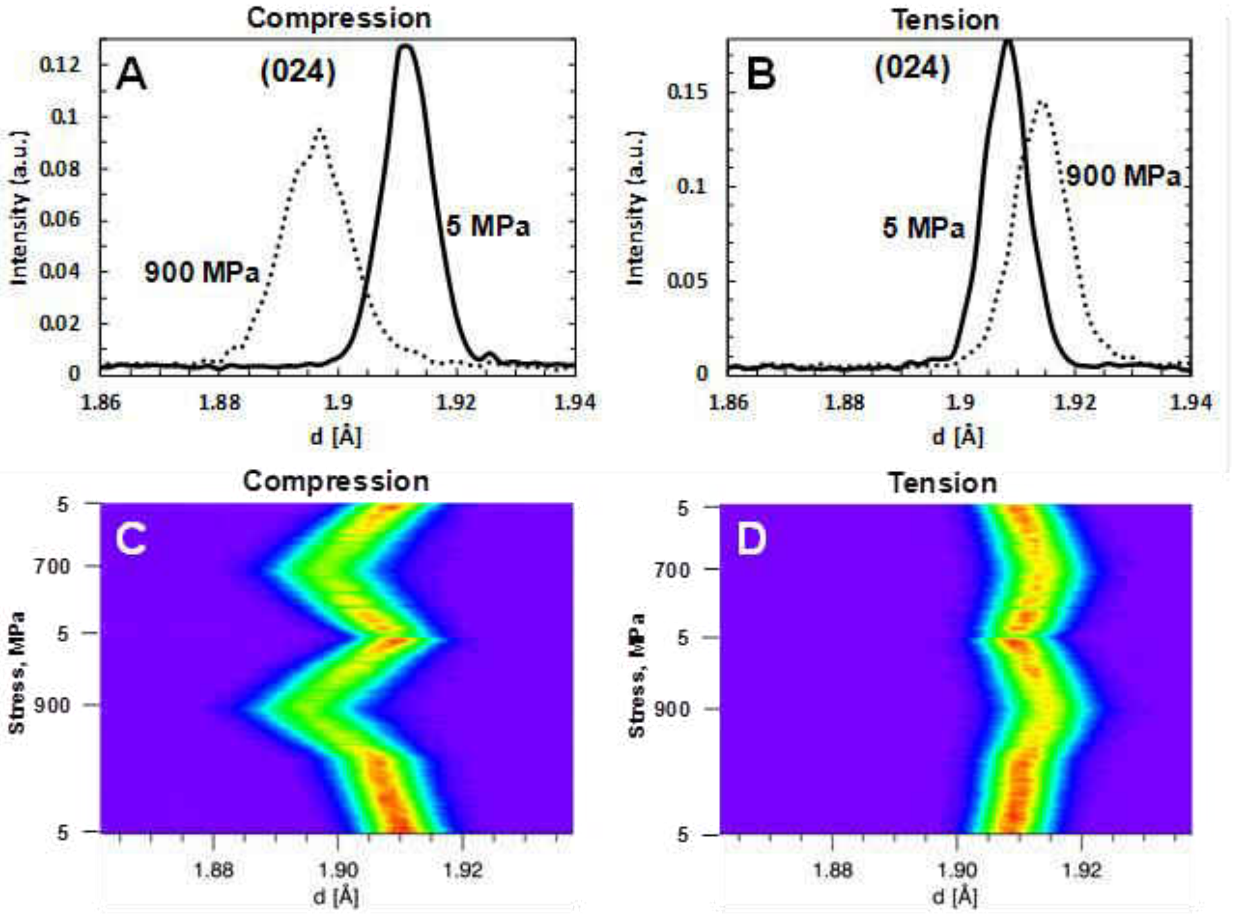

Figure 40: (A, B) Peak profiles of (024) peak at 5 MPa and 900 MPa of first loading measured by detector 1 (A) and detector 2 (B). Part (C) and (D) is a 2-d presentation of the interplanar spacing of (024) peak as a function of applied stress measured at Bank 1 (C) and Bank 2 (D)

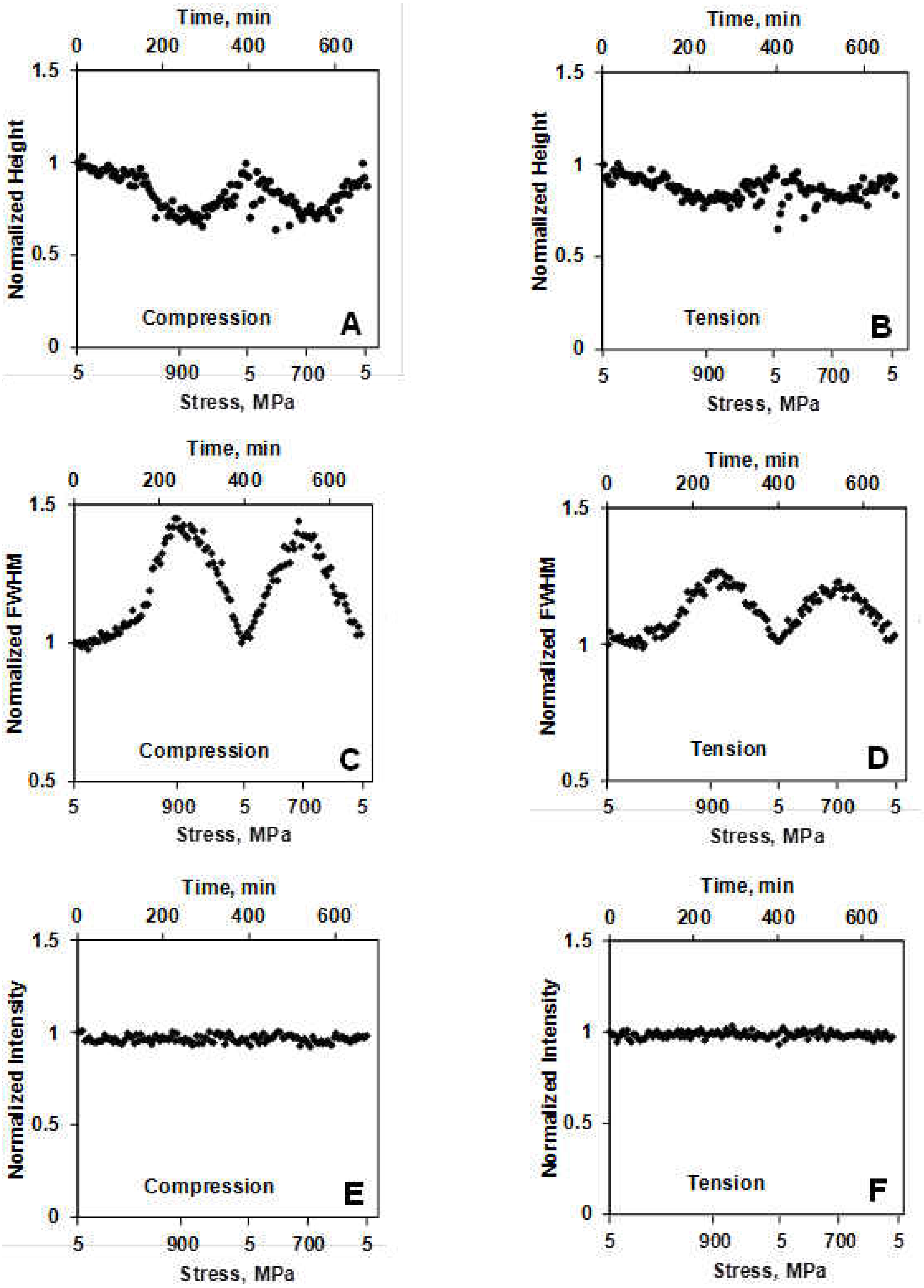

Figure 41: Normalized height, FWHM and area of peak intensity as a function of applied stress for the two loading/unloading cycles, as measured by Bank 1 (A, C, E) and Bank 2 (B, D, F)

3.2.2.3 Study of (006)/(202) and (220)/(208) doublets as a function of applied load

In the case of the single peak (024) the intensity reduced as applied load increased, but never completely disappeared. In the case of doublets the evolution of peak intensities is a lot more dramatic as can be seen in Figure 42. The intensities of the (006) and (208) peaks increases and the interplanar spacing decreases with increase in the applied compressive stress (loading direction) (Figure 42A, C). In the transversal direction, when tensile strain appears the intensities of (006) and (208) peaks decreases and vanishes at high stress values (Figure 44B, D). The opposite trend was observed for the (202) and (220) peaks, the peaks' intensities decreases in the loading direction upon increase of load and vanishes at high stress values, as seen in (A,C). Similar results were reported in the work of Vullum et al [131]. The evolution of peak intensities as a function of applied stress depends on the Miller indices of the reflections and the direction of the diffracted neutron beam relative to the stress axis, similar results was shown for the study of $La_{0.8}Ca_{0.2}CoO_3$ [131]. Another important result to notice is the intensity ratio of the doublet peaks. To verify the correlation between the preferred crystallographic orientation and texture formation, appearance of hysteresis and macroscopic irreversible strain in $LaCoO_3$, the intensity ratio (006)/(202) doublet (Figure 43 E, F) and (208)/(220) (Figure 45 E, F) doublet peaks were plotted as a function of applied stress. As it can be seen the intensity ratio of (202)/(006) and (220)/(208) decreases and approaches a value of zero in the loading direction, while the (006)/(202) ratio decreases and approaches a value of zero in the transversal direction. The intensity ratio of (208)/(220) peak ratio did not approach zero value in the transversal direction, but reduced significantly and followed the same trend as the other peak ratios. The key observation to make from the intensity ratio versus applied stress plots, is that during the first cycle after loading and unloading less than half of the intensity ratios were recovered, but for the second cycle the intensity ratios were almost fully recovered. Therefore, the first loading process introduced certain irreversible crystallographic changes in $LaCoO_3$ structure, causing texture formation. This is the reason that the hysteresis area in the first cycle is larger and irreversible macroscopic strain is produced. However, once the preferred orientations are already formed (in the first cycle), further loading and unloading of the material resulted in completely recoverable domains/twin motion and thus the area of the hysteresis loop for the second cycle is much smaller, the loop is closed and there is no non-recoverable strain produced.

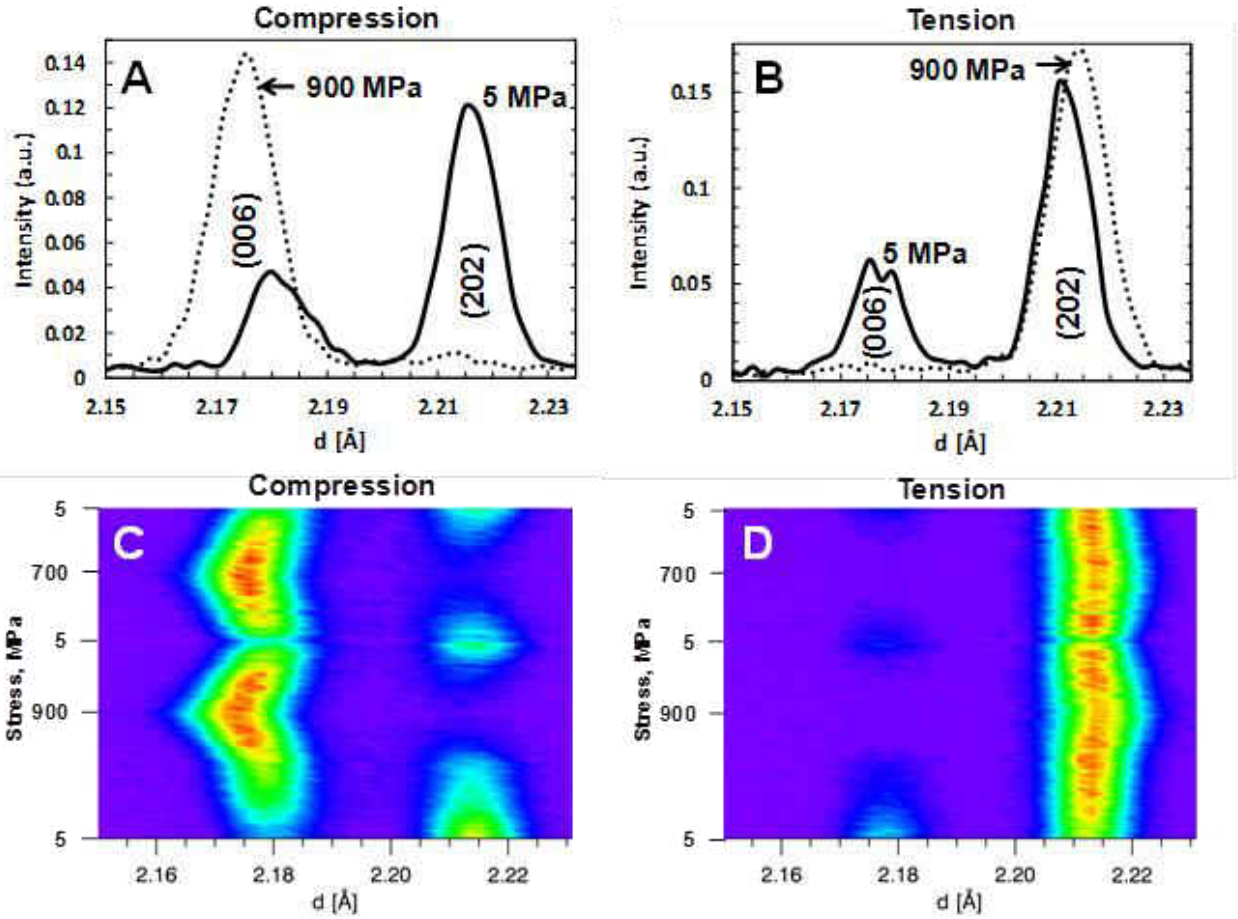

Figure 42. (A, B) Peak profiles of (006) and (202) peaks at 5 MPa and 900 MPa of first loading measured by detector 1 (A) and detector 2 (B). Part (C) and (D) is a 2-d presentation of the interplanar spacing of (006) and (202) peaks as a function of applied stress measured at Bank 1 (C) and Bank 2 (D)

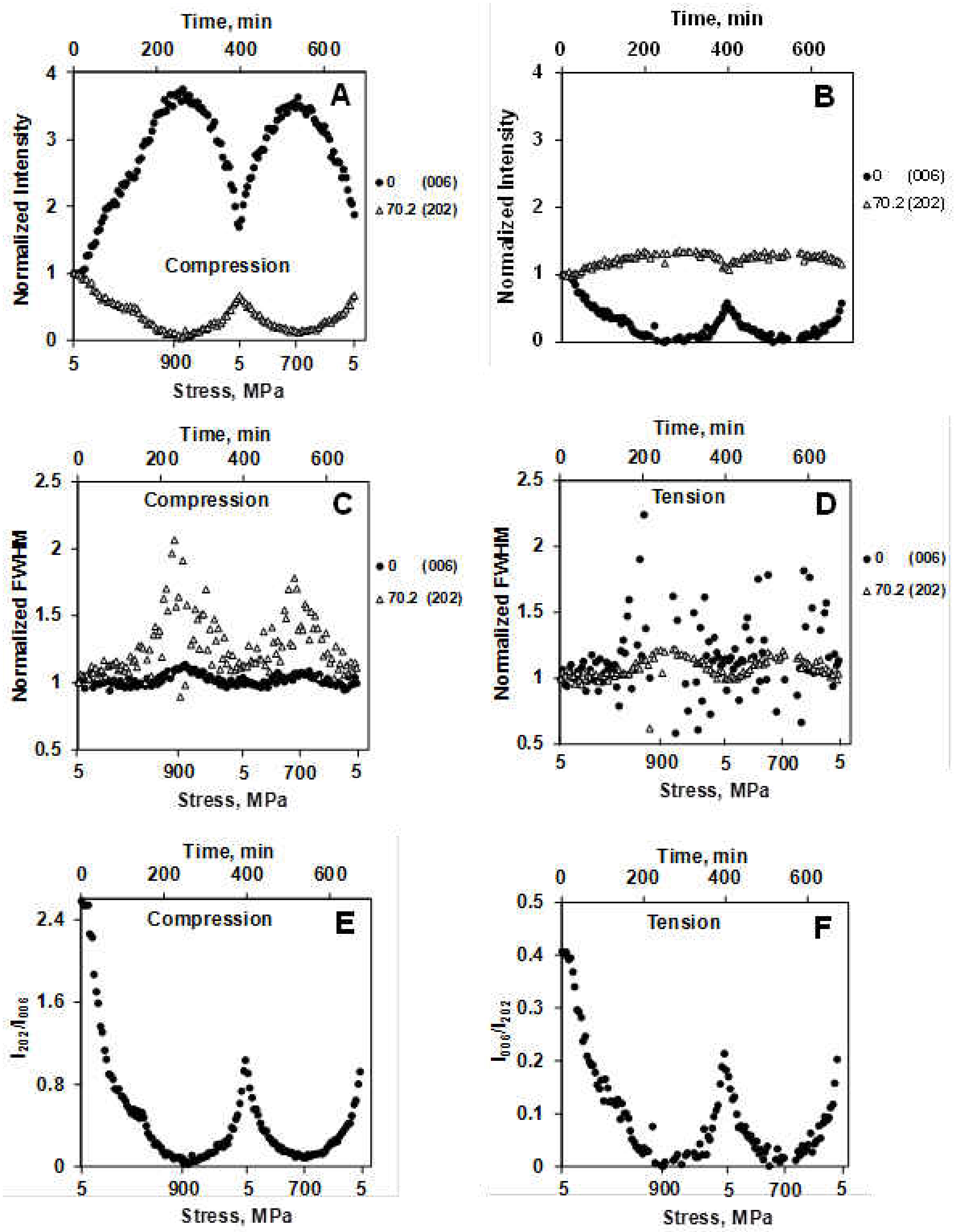

Figure 43: Normalized peak intensity and normalized FWHM for (006) and (202) peaks as a function of applied stress for the two loading/unloading cycles, measured by Bank 1 (A, C) and Bank 2 (B, D). Intensity ratios of (006) and (202) peaks as function of applied stress, measured by Bank 1 (E) and Bank 2 (F)

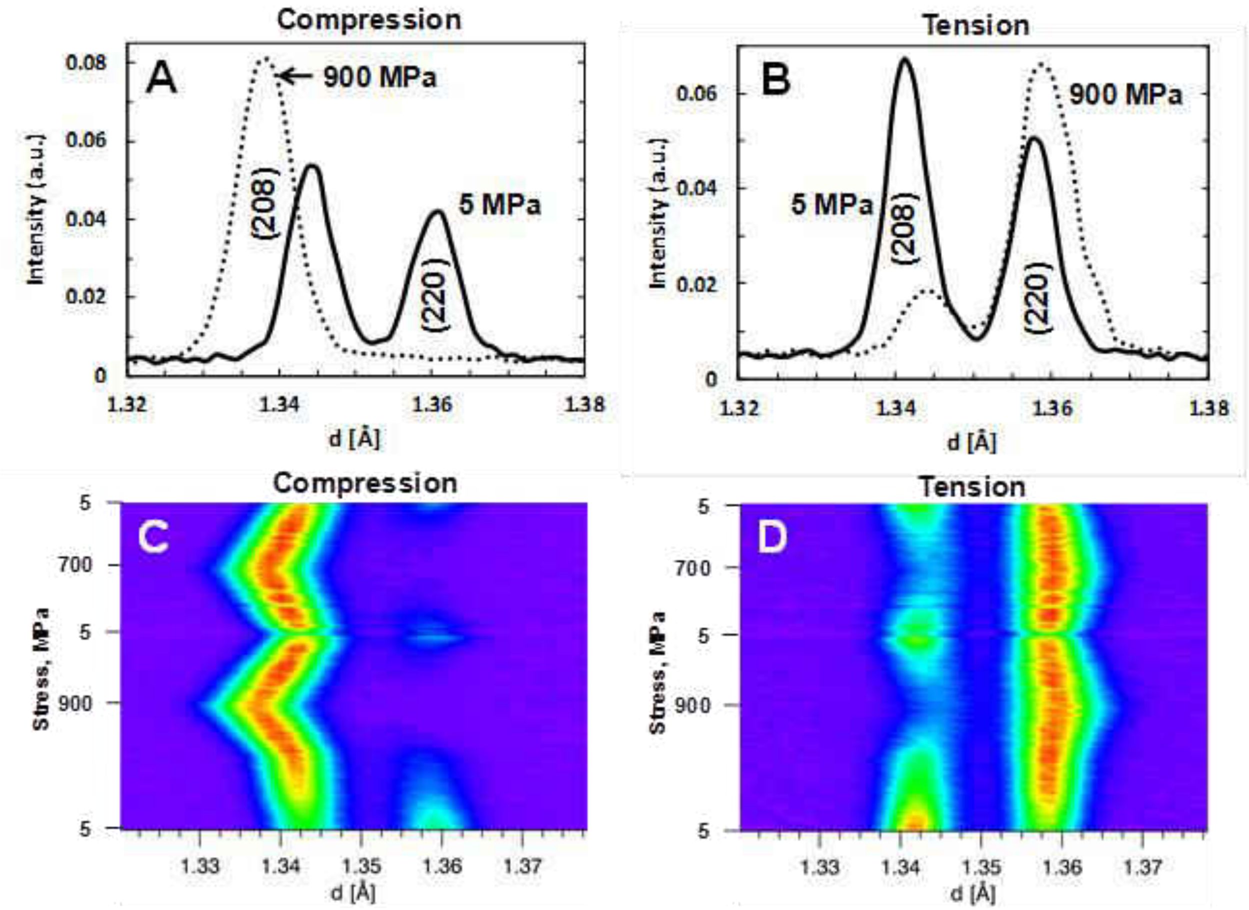

Figure 44: (A, B) Peak profiles of (208) and (220) peaks at 5 MPa and 900 MPa of first loading measured by detector 1 (A) and detector 2 (B). Part (C) and (D) is a 2-d presentation of the interplanar spacing of (208) and (220) peaks as a function of applied stress measured at Bank 1 (C) and Bank 2 (D)

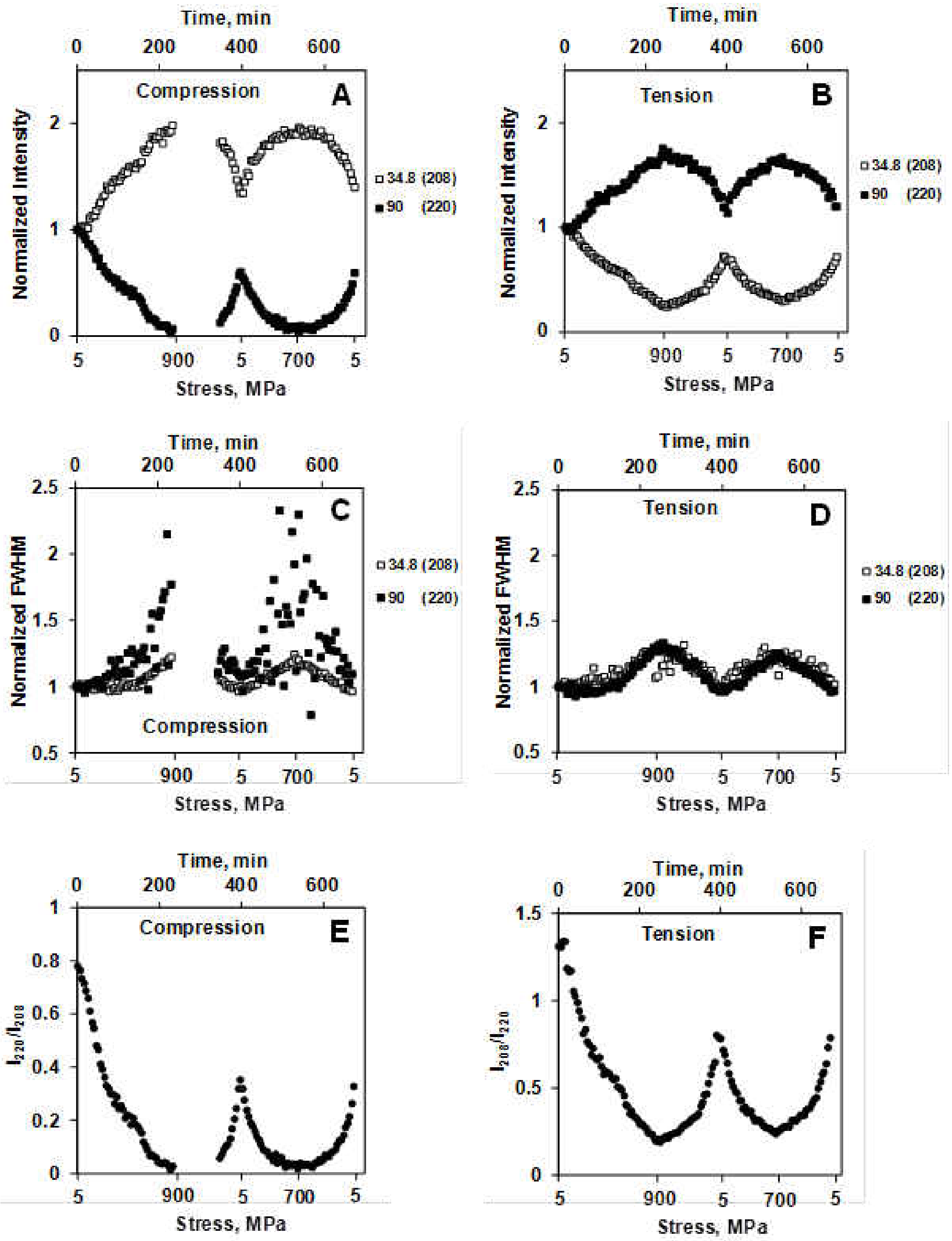

Figure 45: Normalized peak intensity and normalized FWHM for (208) and (220) peaks as a function of applied stress for the two loading/unloading cycles, measured by Bank 1 (A, C) and Bank 2 (B, D). Intensity ratios of (208) and (220) peaks as function of applied stress, measured by Bank 1 (E) and Bank 2 (F)

3.3. Elastic properties of $LaCoO_3$ at room temperature

The majority of the content of this section of the chapter is published in a paper co-authored by the author [68].

The mechanical properties of $LaCoO_3$ ceramics have been extensively investigated in the past decade and ferroelastic deformation along with time dependent room temperature creep have been reported [64, 132-134]. However, only a few publications have reported the elastic properties of $LaCoO_3$, where Young's and bulk moduli were investigated as a function of temperature and stress[129, 135]. The results reported showed that the Young's modulus, measured from the slope of a stress-strain deformation curve, was equal to 76 GPa at the very beginning of uniaxial compression, but increased by almost 2.5 times to 194 GPa when measured at the beginning of unloading from a compressive stress of 900 MPa [67]. The texture and formation of preferred domain orientation during uniaxial compression was studied and it was shown that at high applied stress there was a significant growth of ferroelastic domains with a preferred crystallographic orientations at the expense of other domain orientations. Upon unloading in the first cycle, partial recovery/reappearance of other crystallographic domains was observed. However, the preferred domain orientation and the texture formed in $LaCoO_3$ remained after the load was removed. This domain switching phenomenon was responsible for the hysteresis during a loading/unloading cycle as well as for the appearance of irreversible strain upon unloading since not all domains/twins were recovered to their initial state before deformation. Elastic anisotropy was introduced during such uniaxial loading, therefore the elastic properties of the polycrystalline $LaCoO_3$ are also expected to change. As texture formation is inevitably connected to the growth of preferred crystallographic orientation and an increase of the volume fraction of certain domains, if the elastic constants are known then it would be possible to estimate the anisotropy and calculate the elastic properties of polycrystalline $LaCoO_3$ in different crystallographic directions. Using neutron diffraction the lattice parameters can be calculated as a function of applied compressive stress and other crystal structure analysis can be performed. This makes available the possibility to evaluate the elastic constants and calculate the elastic properties of pure $LaCoO_3$. Here we report our results of the aforementioned evaluations along with an estimation of the elastic anisotropy present in $LaCoO_3$.

3.3.1 Experimental and Methodology

The properties of the polycrystalline $LaCoO_3$ material and the conditions for the *in-situ* uniaxial compression neutron diffraction experiments have been described in our previous work [67, 135, 136]. The properties of the $LaCoO_3$ ceramics are listed in Table 7. Most of the calculations performed in the current paper were done utilizing the neutron diffraction results obtained in [67]. The present evaluation used the loading data during the neutron diffraction. Some of the data used is from a separate study in which tests were performed using uniaxial compression of $LaCoO_3$ to verify the change of the Young's modulus as a function of applied stress when no neutron radiation was present [137]. In the current study, to determine the Young's modulus of $LaCoO_3$ using the slope of the unloading stress-strain deformation plots, the following uniaxial compression experiments were performed. The uniaxial loading/unloading cycling was done using cylindrical samples of 6 mm in diameter and 12 mm height, in a servohydraulic testing machine (Instron 8511) with a 20 kN load cell under load control with a loading rate of 180 MPa/min. The compression stress with a cyclic stress step of 33 MPa was applied parallel to the axis of the cylindrical samples. The axial strain was measured using three strain gauges mounted on the surface of each sample. The total strain was determined by averaging the signals from the three strain gauges.

In addition to uniaxial compression, the impulse excitation technique was used to measure Young's and shear moduli of $LaCoO_3$. The Young's modulus E_0 and shear modulus G_0 of the material were measured at room temperature on two samples, each. The samples had a length of ~36 mm, a width of ~8.0 mm and a height of ~1.5 mm. For each sample the density was calculated from its size and weight. The E_0 and G_0 measurements were performed in accordance to standard EN 843-2, Method D: Impulse excitation using a Grindo-Sonic Mk5 Industrial (Lemmens, Belgium) with a homemade sample holder [138]. Using E_0 and G_0, the Poisson's ratios ν were calculate in using equation $\nu = \frac{E_0}{2G_0} - 1$.

For the collected neutron diffraction patterns, the classification of the (hkl) peaks and their intensities in $LaCoO_3$ was adopted from [131], where the domains' volume fractions as a function of applied stress was analyzed with respect to the angle between the normal to the individual (hkl) diffraction plane and the c hexagonal axis. The peak's classification was adopted to differentiate peaks with diffraction planes with the angles less than 45°, and the peaks with (hkl) planes with the angles higher than 45° [131].

For each (hkl) plane the lattice strains $\varepsilon_{hkl}^{D1}(\sigma^{(i)})$ and $\varepsilon_{hkl}^{D2}(\sigma^{(i)})$ are calculated as a function of applied compressive stress, where

$$\varepsilon_{hkl}^{D1}(\sigma^{(i)}) = \frac{d_{hkl}^{D1}(\sigma^{(i)}) - d_{hkl}^{D1}(\sigma^{(0)})}{d_{hkl}^{D1}(\sigma^{(0)})} \qquad [15]$$

$$\varepsilon_{hkl}^{D2}(\sigma^{(i)}) = \frac{d_{hkl}^{D2}(\sigma^{(i)}) - d_{hkl}^{D2}(\sigma^{(0)})}{d_{hkl}^{D2}(\sigma^{(0)})} \qquad [16]$$

where $d_{hkl}^{D1}(\sigma^{(i)})$ and $d_{hkl}^{D2}(\sigma^{(i)})$ are the spacing of the various (hkl) lattice planes measured by Detector 1 and 2 (parallel and perpendicular to the applied stress), respectively, and i indicates the corresponding applied stress $\sigma^{(i)}$ (or run).

For the calculations of the a_i^{D1}, c_i^{D1}, a_i^{D2}, and c_i^{D2} lattice parameters as a function of applied stress, the procedure used was as shown in the work by Daymond et al [139]. Six peaks, (006), (018), (208), (024), (202), and (220), were used for the calculations using their known $d_{hkl}^{D1}(\sigma^{(i)})$, $d_{hkl}^{D2}(\sigma^{(i)})$ and (hkl) Miller indices with a valid assumption that a_i^{D1}, c_i^{D1}, a_i^{D2}, and c_i^{D2} parameters are the same for all peaks under consideration (Table 8). Taking this assumption into account, the a_i^{D1}, c_i^{D1}, a_i^{D2}, and c_i^{D2} lattice parameters can be determined by using the least squares method for the following expressions

$$\sum_{hkl}\left[\frac{1}{(d_{hkl}^{D1}(\sigma^{(i)}))^2}-\frac{4}{3}\left(\frac{h^2+hk+k^2}{(a_i^{D1})^2}\right)-\frac{l^2}{(c_i^{D1})^2}\right]^2 \qquad [17]$$

$$\sum_{hkl}\left[\frac{1}{(d_{hkl}^{D2}(\sigma^{(i)}))^2}-\frac{4}{3}\left(\frac{h^2+hk+k^2}{(a_i^{D2})^2}\right)-\frac{l^2}{(c_i^{D2})^2}\right]^2 \qquad [18]$$

Since two detectors were used for the collection of diffraction patterns [67], the a_i^{D1} and c_i^{D1} lattice parameters determined from reflections parallel to the applied stress direction collected by Detector 1 were from the lattice planes under compression, and a_i^{D2} and c_i^{D2} lattice parameters determined from reflections perpendicular to the applied stress direction were collected from the lattice planes under tension collected by Detector 2. Once a_i^{D1}, c_i^{D1}, a_i^{D2}, and c_i^{D2} lattice parameters are determined both for tension and for compression, the average lattice strains

$\varepsilon_{ave}^{D1}(\sigma^{(i)})$ and $\varepsilon_{ave}^{D2}(\sigma^{(i)})$ for the i applied stress can be found by averaging the strains connected with a_i and c_i lattice parameters [139] by using the expressions

$$\varepsilon_{ave}^{D1}(\sigma^{(i)}) = \frac{2\varepsilon_a^{D1}(\sigma^{(i)}) + \varepsilon_c^{D1}(\sigma^{(i)})}{3} \qquad [19]$$

$$\varepsilon_{ave}^{D2}(\sigma^{(i)}) = \frac{2\varepsilon_a^{D2}(\sigma^{(i)}) + \varepsilon_c^{D2}(\sigma^{(i)})}{3} \qquad [20]$$

where

$$\varepsilon_a^{D1}(\sigma^{(i)}) = \frac{a_i^{D1} - a_0^{D1}}{a_0^{D1}} \qquad [21]$$

$$\varepsilon_c^{D1}(\sigma^{(\mathrm{i})}) = \frac{c_i^{D1} - c_0^{D1}}{c_0^{D1}} \qquad [22]$$

$$\varepsilon_a^{D2}(\sigma^{(i)}) = \frac{a_i^{D2} - a_0^{D2}}{a_0^{D2}} \qquad [23]$$

$$\varepsilon_c^{D2}(\sigma^{(\mathrm{i})}) = \frac{c_i^{D2} - c_0^{D2}}{c_0^{D2}} \qquad [24]$$

As it was shown in the work of Daymond [140],^{13} the average lattice strain $\varepsilon_{ave}^{D1}(\sigma^{(i)})$ coincides well with continuum elastic strain measured during macrodeformation, therefore the equation

$$\sigma^{(i)} = E_i \varepsilon_{ave}^{D1}(\sigma^{(i)}) \qquad [25]$$

can be utilized to determine the Young's modulus of the material under investigation

$$E_i = \sigma^{(i)} / \varepsilon_{ave}^{D1}(\sigma^{(i)}) \qquad [26]$$

The straightforward route to determine Young's moduli in different crystallographic direction, which in turn would determine the anisotropy of the material, would be to utilize

$$\sigma_{hkl}^{(i)} = E_{hkl}\varepsilon_{hkl}^{D1}(\sigma^{(i)}) \qquad [27]$$

where $\sigma_{hkl}^{(i)} = \sigma^{(i)} + \sigma_{hkl}^{m}$ is average stress along loading direction in the domains with (hkl) planes oriented normal to the loading direction, E_{hkl} is Young's modulus measured in the direction normal to the (hkl) planes, σ_{hkl}^{m} is local misfit stress generated by the grain anisotropy. However, Eq. (11) is not valid if instead of $\varepsilon_{ave}^{D1}(\sigma^{(i)})$, the $\varepsilon_{hkl}^{D1}(\sigma^{(i)})$ of individual crystallographic spacing of the grain is used. The reason that Eq. (11) is not valid, when individual $\varepsilon_{hkl}^{D1}(\sigma^{(i)})$ are used, is the presence of local misfit stress σ_{hkl}^{m}, generated by the grain anisotropy. Such misfit stress depends on grain morphology and its surrounding, the grain boundaries' properties and the history of ferroelastic deformation the grain experienced during loading. Since σ_{hkl}^{m} is unknown and cannot be measured, the following approach was used in the present paper to determine Young's modulus of $LaCoO_3$ as a function of crystallographic orientation. If one considers that the macroscopic applied stress $\sigma^{(i)}$ is imposed on the bulk sample then the stress balance can be written as [140]

$$\sigma^{(i)} = \sum_{hkl} f_{hkl}^{(i)}\sigma_{hkl}^{(i)} = \sum_{hkl} f_{hkl}^{(i)} E_{hkl}\varepsilon_{hkl}^{D1}(\sigma^{(i)}) \qquad [28]$$

where $f_{hkl}^{(i)}$ represents the fraction of grains in the volume with orientation (hkl) planes normal to the loading direction. The volume fraction of (hkl) domains normal to loading direction for a specific applied stress (run) *i* can be estimated by

$$f_{hkl}^{(i)} = \frac{I_{hkl}^{D1}(\sigma^{(i)}) / I_{hkl}^{D1}(\sigma^{(0)})}{\sum_{hkl} I_{hkl}^{D1}(\sigma^{(i)}) / I_{hkl}^{D1}(\sigma^{(0)})} \qquad [29]$$

where $I_{hkl}^{D1}(\sigma^{(i)})$ is the intensity of the (hkl) diffraction peak collected by Detector 1 for the run i, $I_{hkl}^{D1}(\sigma^{(0)})$ is the intensity for the run 0. The stress balance (14) assumes the summation over all possible crystallographic directions. However, in practice, the main characteristic crystallographic orientations can be used to obtain good representation of stress balance [140]. As it was investigated in in the work of Daymond [140], the number of peaks used to calculate the average lattice strain can be as low as five, where results from use of five (hkl) peaks are indistinguishable compared to the results from using seven peaks or more. Therefore, only six peaks of LaCoO3 were included for average lattice strain analysis. Thus, as $\sigma_{hkl}^{(i)}$ is unknown *a priori*, it will be replaced with $E_{hkl}\varepsilon_{hkl}^{D1}(\sigma^{(i)})$, as it was specified in (14).

For single crystal with $R\bar{3}c$ rhombohedral symmetry, the relationship between elastic stresses and strains can be expressed as [141]

$$\begin{bmatrix} \varepsilon_1 \\ \varepsilon_2 \\ \varepsilon_3 \\ \gamma_4 \\ \gamma_5 \\ \gamma_6 \end{bmatrix} = \begin{bmatrix} S_{11} & S_{12} & S_{13} & S_{14} & 0 & 0 \\ S_{12} & S_{11} & S_{13} & -S_{14} & 0 & 0 \\ S_{13} & S_{13} & S_{33} & 0 & 0 & 0 \\ S_{14} & -S_{14} & 0 & S_{44} & 0 & 0 \\ 0 & 0 & 0 & 0 & S_{44} & 2S_{14} \\ 0 & 0 & 0 & 0 & 2S_{14} & 2(S_{11}-S_{12}) \end{bmatrix} \begin{bmatrix} \sigma_1 \\ \sigma_2 \\ \sigma_3 \\ \sigma_4 \\ \sigma_5 \\ \sigma_6 \end{bmatrix} \qquad [30]$$

where S_{11}, S_{33}, S_{44}, S_{12}, S_{13}, S_{14} are six independent elastic compliance coefficients, $\varepsilon_1 = \varepsilon_{11}$ $\varepsilon_2 = \varepsilon_{22}$ $\varepsilon_3 = \varepsilon_{33}$ $\gamma_4 = \varepsilon_{23} + \varepsilon_{32}$ $\gamma_5 = \varepsilon_{13} + \varepsilon_{31}$ $\gamma_6 = \varepsilon_{12} + \varepsilon_{21}$ are strain components, $\sigma_1 = \sigma_{11}$ $\sigma_2 = \sigma_{22}$ $\sigma_3 = \sigma_{33}$ $\sigma_4 = \sigma_{23}$ $\sigma_5 = \sigma_{13}$ $\sigma_6 = \sigma_{12}$ are stress components using Voigt notation. For rhombohedral $R\bar{3}c$ symmetry the Young's modulus in the direction perpendicular to (hkl) plane, E_{hkl}, can be expressed by the following equation [141]

$$E_{hkl} = \left\{ \frac{(h_n^2 + k_n^2 - h_n k_n)^2 (a_i^{D1})^4 S_{11} + l_n^4 (c_i^{D1})^4 S_{33} + (h_n^2 + k_n^2 - h_n k_n) l_n^2 (a_i^{D1} c_i^{D1})^2 (S_{44} + 2S_{13}) + 3\sqrt{3} h_n k_n l_n (h_n - k_n)(a_i^{D1})^3 c_i^{D1} S_{14}}{\left[(h_n^2 + k_n^2 - h_n k_n)(a_i^{D1})^2 + l_n^2 (c_i^{D1})^2 \right]^2} \right\}^{-1} \qquad [31]$$

where S_{11}, S_{33}, S_{44}, S_{13}, and S_{14} are elastic compliance coefficients, $h_n = \frac{2}{3(a_i^{D1})^2}(2h+k)$, $k_n = \frac{2}{3(a_i^{D1})^2}(h+2k)$, and $l_n = \frac{l}{(c_i^{D1})^2}$ are indices of the corresponding crystallographic directions in a hexagonal coordinate system.

Equation [31] has a dependence on lattice parameters. However, this represents a dependence of E_{hkl} on *a/c* ratio of lattice parameters, as one can see after simple transformations of Eq. [31]. Besides, for directions parallel to the c-axis (h_n=k_n=0) and for all directions perpendicular to c-axis (l_n=0) there is no dependence of E_{hkl} on *a*, *c* or *a/c*, which can be easily verified for equation [31]. Additionally, in this case the difference between *a/c* ratio at zero stress and at maximum applied stress (i.e. maximum variation) is less than 0.1 %, thus a variation of parameter *a/c* with applied stress can be considered to be negligible. Therefore no dependence of E_{hkl} on *a*, *c* or *a/c* is found.

Using Eqs. [28] and [31] the compliance coefficients S_{11}, S_{33}, S_{44}, S_{13}, and S_{14} can be determined by finding the minimum of the following expression:

$$\sum_i \left[\sigma^{(i)} - \sum_{hkl} f_{hkl}^{(i)} E_{hkl} \varepsilon_{hkl}^{D1}(\sigma^{(i)}) \right]^2 \qquad [32]$$

In such a way the macroscopic stress $\sum_{hkl} f_{hkl}^{(i)} E_{hkl} \varepsilon_{hkl}^{D1}(\sigma^{(i)})$ calculated from stress balance becomes the closest one to the applied stress $\sigma^{(i)}$.

The estimation of the upper and lower bounds of Young's modulus was also performed using the standard procedure [142]. In general, if the polycrystal is treated as a composite and domains with orientation (hkl) planes normal to the loading direction as separate phase, we can find upper and lower bounds for its Young's modulus using

$$E_i^{(V)} = \sum_{hkl} f_{hkl}^{(i)} E_{hkl} \qquad [33]$$

$$E_i^{(R)} = \left[\sum_{hkl} (f_{hkl}^{(i)} / E_{hkl}) \right]^{-1} \qquad [34]$$

Eq. (19) determines an upper bound according to Voigt [142], where strains are considered to be constant, to estimate the Young's modulus of the composite by the rule of mixtures for stiffness components. Eq. (20) determines a lower bound according to Reuss [142], where stresses are considered to be constant in a composite, to estimate the Young's modulus by the rule of mixtures for compliance components. For the calculations of the upper and lower bounds of Young's modulus of $LaCoO_3$ as a function of applied stress, the following procedure was developed. Eq. (17) was used for calculation of E_{hkl}, for the specific (hkl) directions using the elastic constants presented in Table 9. These E_{hkl} values do not depend on the applied stress. Then, using Eq. (15), the f_{hkl} volume fraction of relevant domains with orientation of their (hkl) planes normal to the loading direction are calculated as a function of applied stress. The f_{hkl} values are stress dependent and will increase/decrease as a function of applied stress. After E_{hkl} and f_{hkl} are calculated, the upper and lower bounds of Young's modulus of $LaCoO_3$ are estimated using Eq. (19) and Eq. (20) respectively. Therefore, stress independent elastic constants and stress dependent volume fraction of domains were employed for the calculation of the upper and lower bounds of the Young's modulus.

3.3.2 Results and discussion

Examples of the diffraction patterns of $LaCoO_3$ collected at selected stress levels by Detector 1 in the direction parallel to the stress axis and by Detector 2 perpendicular to the stress axis are shown in Figure 45A and B. As already discussed in previous work [67], the material was initially isotropic at the beginning of loading as confirmed by the identical diffraction patterns recorded by the two detectors. However, the formation of preferred orientation was quickly detected when loading started. The rhombohedral angle of this material is 60.8°. The rhombohedral lattice constant is 5.37 Å. The evolution of the peak intensities depended on the Miller indices of the reflections and on the strain experienced by the lattice – compressive (Detector 1) or tensile (Detector 2). The (202) peak intensity decreased and (006) peak intensity increased for Detector 1 when the applied stress increased along the direction of detector D1. When the sample experienced tensile macroscopic strain in the direction perpendicular to the applied stress (D2), the (202) peak intensity increased and (006) peak vanished at high applied stress. Similar behavior was reported to occur in $La_{0.8}Ca_{0.2}CoO_3$ upon uniaxial compression [131].

In the paper by Vullum et al, the (*hkl*) peaks of $LaCoO_3$ were classified according to the orientation of the corresponding diffraction planes with respect to the *c*-axis and the reorientation of the domains was analyzed according to the angle between the loading direction and the *c*-axis of the domain. These angles for characteristic diffraction planes used for analysis in this paper are presented in Table 8. In the case when the diffraction planes are perpendicular to the stress axis, the intensity of reflections increases with stress for diffraction planes with the angle between their normal and *c*-axis of less than 45°; while the intensity of reflections decreases with stress for diffraction planes with the angle between their normal and *c*-axis of higher than 45°. In the case when diffraction planes are parallel to the stress axis, the intensity of reflections increases for diffraction planes with the angle between their normal and *c*-axis higher than 45°, while the intensity decreases for diffraction planes with the angle between their normal and *c*-axis less than 45°. The reorientation of the domains increases the volume fraction of domains that have their *c*-axis more parallel to the stress axis. The volume fraction of domains with the angle between their *c*-axis and the loading direction of less than 45° increases at the expense of that of the domains with the angle between their *c*-axis and the loading direction higher than 45° due to domain reorientation.

The evolution of peaks intensities and strain development in selected (*hkl*) reflections as a function of applied stress is shown in Figure 47. The peak intensities were measured as the area below the reflection, and are presented after normalizing the intensity with the initial intensity of each reflection at the beginning of loading. According to the orientation of the peaks relative to the *c*-axis, the intensities of the peaks can increase, decrease or remain constant upon increase of applied stress. The intensities of the peaks collected by both Detector 1 and Detector 2 are presented in Figure 47A and B. It is obvious from Figure 47A that the intensities of the peaks from diffraction planes with the angle between their normal and *c*-axis less of less than 45° grow under compression, while the intensities of peaks from diffraction planes with the angle between their normal and *c*-axis of more than 45° decrease, as was measured by Detector 1. At the same time, the opposite changes in the intensities of the peaks are observed when planes are under tension, as measured by Detector 2. The intensity of the (024) peak remains constant and independent of applied stress both for compression and tension directions. The increase/decrease of the peaks' intensities indicates the increase/decrease of the volume fraction of mobile ferroelastic domains, due to domain movement and reorientation. The reorientation causes the increase of the volume fraction of domains that have their *c*-axis aligned more closely to the stress axis, such as the intensities of the peaks with high values of the Miller index *l* (and low *h* and *k*) increase, while the intensities of the reflections with high *h* and *k* values decrease. Exactly the same results are reported for $La_{0.8}Ca_{0.2}CoO_3$ and more description of the domain switching related to the $LaCoO_3$ based perovskites can be found in the work of Vullum et al [131].

The individual $\varepsilon_{hkl}^{D1}(\sigma^{(i)})$ and $\varepsilon_{hkl}^{D2}(\sigma^{(i)})$ strains for six crystallographic planes under consideration calculated from the data obtained by Detector 1 and Detector 2 are shown in Figure 472C and D. Five of the planes, (006), (018), (208), (202), and (220) belong to the doublets, whose intensities changed significantly depending on the orientation angle of the plane normal either parallel or perpendicular to the applied load, and one of the planes, (024), a singlet for which intensity did not change as applied load increased to 900 MPa. Each of the $\varepsilon_{hkl}^{D1}(\sigma^{(i)})$ and $\varepsilon_{hkl}^{D2}(\sigma^{(i)})$ strains represent the response of a family of domains oriented such that the given (*hkl*) lattice plane normal is parallel (Figure 47C) and perpendicular (Figure 47D) to the loading direction. The response of each individual plane under consideration deviates from linear behavior and does not represent a linear elastic response due to internal stresses, as the way one would expect the lattice to deform.

The authors do not treat the non-linear stress-strain response (Figure 47 C and D) as due to the presence of plastic deformation, but consider it as an effect of unknown internal stresses identified as local misfit stresses generated by the grain anisotropy. Lattice strain is treated as a linear function of total stress, which consists of a sum of the applied stress with a known value and a local internal stress with an unknown value. However, since the term is connected with internal stress, the strain shows a non-linear behavior as a function of applied stress. It is important to understand that an internal stress is not constant but is an unknown function of applied stress. Note that the domain wall motion can affect the accommodation of the internal stress.

The Young's moduli E_{hkl}, if calculated from the slopes of applied stress – lattice strain dependence, provide non-realistic values, such as E_{006}= 250 GPa, E_{018}= 110 GPa, E_{208}= 180 GPa, E_{024}= 80 GPa, E_{202}= 300 GPa, and E_{220}= 140 GPa, which are very different from the elastic modulus of isotropic polycrystalline $LaCoO_3$, which is 76 GPa as measured by an impulse excitation technique. They are not realistic because in addition to the applied stress $\sigma^{(i)}$, there is an additional local misfit stress σ_{hkl}^{m}, such that the stress $\sigma_{hkl}^{(i)}$ acting in each domain is a sum of the $\sigma^{(i)}$ and σ_{hkl}^{m} stresses. The local misfit stress σ_{hkl}^{m} is generated by the domain anisotropy and the misfit of the specific domain with the neighboring domains. This misfit stress can be more easily accommodated by the doublet planes which are mobile, easy to restructure and can participate in the domain switching, therefore, the resulting lattice strain calculated for (006)/(202), (208)/(220), and (018) planes is significantly lower, especially at high loads, in comparison with lattice strain which is calculated for the (024) plane. It indicates that the misfit stress will play a much stronger role in the deformation of crystallographic planes where no extra mechanisms of stress accomodations, such as domain switching, are present. The domain wall motion does not directly affect the value of Young's modulus. The domain wall motion can affect the accommodation of internal stress, with the internal stress affecting a non-linear dependence of strain as a function of applied stress. What is clear from calculations of the lattice strain of individual planes, is that the Young's modulus cannot be determined correctly using the data presented in Figure 47C, because the applied stress values do not correspond to the stress level located at each individual domain.

To calculate E_{hkl} and average lattice strains parallel and perpendicular to the loading direction the a_i^{D1}, c_i^{D1}, a_i^{D2}, and c_i^{D2} lattice parameters have to be determined. For these calculations Eqs. (3) and (4) were utilized by averaging the d spacing data of six peaks using data collected from Detectors 1 and 2 measurements. The results of the calculations are presented in Figure 48A and B. As one can see from the Figure 48 a decrease of the a_i^{D1} and c_i^{D1} lattice parameters is observed when the planes are oriented perpendicular to the applied compressive stress, and when subjected to a tensile deformation an increase of the a_i^{D2} and c_i^{D2} lattice parameters is observed for the planes with parallel orientation toward applied stress direction. Once the a_i^{D1}, c_i^{D1}, a_i^{D2}, and c_i^{D2} lattice parameters of $LaCoO_3$ were determined, the average lattice strains $\varepsilon_{ave}^{D1}(\sigma^{(i)})$ and $\varepsilon_{ave}^{D2}(\sigma^{(i)})$ were also calculated (Figure 48C). As already mentioned in Section 2 of this paper, the average lattice strain $\varepsilon_{ave}^{D1}(\sigma^{(i)})$ coincides well with the continuum elastic strain measured by the extensometer during loading of the cobaltite, which is reported in previous work [67]. Therefore it can be easily utilized for Young's modulus estimation of $LaCoO_3$ polycrystal as a function of applied stress. It is worth mentioning that while the average lattice strain versus applied stress data provide a small scatter of the experimental data points at lower stress levels, when the stress reaches 700 – 900 MPa the scatter of the data becomes much more significant. A similar trend is also reported in the work of Daymond [140], where the magnitude of the error in measuring of average elastic lattice strain was reported to be as high as 16% at high applied stress level. In this case a larger scattering of the data is connected with a higher loading rate and broader stress interval for a given collection time (time interval to average neutron response) at higher stress levels.

As the average lattice strain was determined for planes under compressive and tensile deformations, as measured by Detectors 1 and 2, this would give us a chance to determine the Poisson's ratio ν by dividing the lateral strain $\varepsilon_{ave}^{D2}(\sigma^{(i)})$ by the radial strain $\varepsilon_{ave}^{D1}(\sigma^{(i)})$. If we directly use the experimental strain values, as presented in Figure 48C to calculate ν, a very large scattering of the experimental Poisson's ratio data points occurs (Figure 48D). If we fit $\varepsilon_{ave}^{D1}(\sigma^{(i)})$ and $\varepsilon_{ave}^{D2}(\sigma^{(i)})$ with straight lines, then the ratio of the slopes of these lines provides us with a Poisson's ratio ν value equal to 0.45. Note that using $\varepsilon_{a}^{D1}(\sigma^{(i)})$ and $\varepsilon_{a}^{D2}(\sigma^{(i)})$ we obtain Poisson's ratio equal to 0.5, and using $\varepsilon_{c}^{D1}(\sigma^{(\mathrm{i})})$ and $\varepsilon_{c}^{D2}(\sigma^{(\mathrm{i})})$ we have ν=0.32. The experimentally measured value of $LaCoO_3$ Poisson's ratio by impulse excitation technique is equal to 0.32. The fitting straight line for $\varepsilon_{ave}^{D1}(\sigma^{(i)})$ with the slope corresponding to ratio 0.32 is also shown in Figure 48C, along with the values of Poisson's ratio calculated using $\varepsilon_{a}^{D1}(\sigma^{(i)})$, $\varepsilon_{a}^{D2}(\sigma^{(i)})$ and $\varepsilon_{c}^{D1}(\sigma^{(i)}), \varepsilon_{c}^{D2}(\sigma^{(i)})$. The ultimate ν=0.5, the ratio 0.45 and Poisson's ratio 0.32 measured by acoustic technique are shown in Figure 48D. The acoustic technique allows the measurement of Young modulus *E* and shear modulus *G* of material with the Poisson's ratio calculated as *E/2G-1*. Since it is not known if the Poisson's ratio would change as the applied stress increases, it might be that the obtained values are valid only at the beginning of loading, where the applied stress is small and the material is isotropic. The value of Poisson's ratio of 0.45 presented is quite large indeed. Inelastic deformation (non-linearity of strain-stress dependence), low accuracy of lattice strain determination, effect of internal stresses can all contribute to the high value reported. Therefore, more research is required to clarify the dependence of Poisson's ratio of $LaCoO_3$ on applied compressive stress.

For pure hexagonal structure there are five non-zero compliance coefficients. While the $R\overline{3}c$ rhombohedral structure of $LaCoO_3$ can be described using a hexagonal unit cell, strictly speaking it does not possess hexagonal symmetry since it does not have a 6-fold symmetry and only a 3-fold rotational symmetry about the c-axis. Therefore, for $R\overline{3}c$ rhombohedral structures six non-zero compliance coefficients exist, but in order to determine E_{hkl} one needs to know only five of them. If we know the compliance coefficients S_{11}, S_{33}, S_{44}, S_{13}, S_{14}, and a_i^{D1} and c_i^{D1} lattice parameters, we can easily determine the Young's modulus of the compounds in a specific crystallographic direction, which is perpendicular to the (hkl) plane of interest. The values of five compliance coefficients have been estimated using Eqs. (17) and (18) (Table 9). Figure 49A shows the calculated values of E_{hkl} as a function of angle between plane normal and the c-axis of the lattice. The solid line, also presented in Figure 49A, is given for guidance and corresponds to the theoretical dependence of Young's modulus versus plane orientation angle for 6-fold hexagonal structure. As one can see, there is perfect agreement between 3-fold $LaCoO_3$ and 6-fold hexagonal lattice for the planes with 0^{o} and 90^{o} angle, as is predicted by theory. However, the discrepancies between the two structures exists for (018), (208), (024), and (202) planes, since to elastically characterize the linear elastic properties of $R\overline{3}c$ rhombohedral structure more non-zero compliance coefficients are needed compared to the hexagonal structure. As one can see from Figure 49A, the directions perpendicular to (006), (018), and (208) planes have higher elastic moduli in comparison with directions perpendicular to the (024), (202), and (220) planes. The volume fraction of (006), (018), and (208) domains increases when a uniaxial compressive stress is applied. From macroscopic stress-strain deformation plots one can see that the Young's modulus of the $LaCoO_3$ polycrystal increased significantly when the stress was high, such as 900 MPa[7] and severe texture in $LaCoO_3$ is present. Such an increase in the Young's modulus of the polycrystalline material can be easily explained by the increase of the volume fraction of single domains with high Young's moduli along the loading direction.

Since the average lattice strain $\varepsilon_{ave}^{D1}(\sigma^{(i)})$ corresponds well with the elastic portion of the total macroscopic strain, the Young's modulus as a function of applied stress for $LaCoO_3$ can be determined utilizing Eq. (12). The results of such calculations are presented in Figure 49B as circles. As one can see from Figure 49B a rather significant increase of Young's modulus is reported when the applied stress increases from about 5 MPa at the beginning of the loading to the maximum compressive stress of 900 MPa. The Young's modulus value measured at the beginning of loading, where the material is still isotropic is shown in Figure 46, corresponds well with the values measured both by impulse excitation technique and from the slope of the macroscopic stress-strain deformation curve published in previous work [67]. The results shown in Figure 49B at zero applied stress, provide the Young's modulus value equal to 76 GPa, as it was reported in earlier publications [67, 134]. As the texture and domain reorientation developed very fast at small applied stress [67], the fast increase in the Young's modulus to ~145-150 GPa at small applied stress (30-50 MPa) can be seen in Figure 49B. As the $\sigma^{(i)}$ values grow to the maximum compressive stress (900 MPa), an increase of the Young's modulus is further observed. For comparison, the value of Young's modulus calculated as a slope of the macroscopic stress-strain deformation curve measured by the extensometer during neutron diffraction experiments at 900 MPa while unloading began is also presented in Figure 49B as squares. It is important to notice here that excellent coincidence was found not only for

Young's modulus values obtained from the extensometer and average lattice strain measurements, but it is also equal to the measured portion of macroscopic elastic strain, equal to 0.0046 at 900 MPa, from the macroscopic stress-strain deformation plot and the calculated value of average lattice strain $\varepsilon_{ave}^{D1}(\sigma^{(i)})$, equal to 0.0044 at the same applied stress, which shows an excellent coincidence too. For estimation of the upper and lower bounds of the Young's modulus of polycrystalline $LaCoO_3$ the compliance coefficients presented in Table 9 along with the intensities of (*hkl*) peaks reported in previous work[7] were used. The Eqs. (19) and (20) were employed in these calculations. As one can see there is a perfect match between predicted upper and lower bounds and the elastic modulus values measured utilizing average lattice strain $\varepsilon_{ave}^{D1}(\sigma^{(i)})$ as well as two experimental data points obtained at the beginning of loading and 900 MPa applied stress from the macroscopic measurements. Such good coincidence of the experimental and calculated results verify the validity of the compliance coefficients and significant elastic anisotropy of the $LaCoO_3$ ceramic formed during uniaxially compressed samples.

For further independent verification of the formation of elastic anisotropy, several $LaCoO_3$ samples have been uniaxially compressed where the incremental increase in load was applied during cycling and no neutron diffraction was performed during compression. It was found that Young's modulus of such samples was equal to 76 GPa at the beginning of loading, which is the same value as it was measured for other isotropic $LaCoO_3$ ceramics. However, instead of showing a rather sharp increase in elastic modulus at small 30-50 MPa loads as it is seen for the sample under neutron irradiation, the Young's modulus remains almost constant or slightly decreases as the applied stress increased to 130 MPa, and the Young's modulus slowly increases its values as the applied stress increased further. At a high applied stress (700 MPa) the Young's modulus was measured to be equal to 140 GPa which is significantly lower than the values measured during neutron diffraction experiments. While there is a clear difference between material behavior when neutron radiation is present or absent, the reason for such discrepancies is not well understood. At least two factors can contribute: first factor is radiation effect on the domain walls' movement and texture formation, and the second factor is different loading rates used in the experimental procedure. It is fair to expect that bombardment of $LaCoO_3$ by neutrons may produce defects, as it was reported for SiC or B_4C and many other ceramics, and alleviate domain movement making domain boundaries much more mobile and texture easier to form. However, the energies of thermal neutrons used in the current experiment at SNS are fairly low (<400 meV), comparable to those of phonons, thus it is not likely that such significant differences in the domain walls' mobilities and stiffening of the $LaCoO_3$ would be caused by the neutron radiation. At the same time, the loading rate of the $LaCoO_3$ sample during neutron diffraction experiments was equal 1.3 MPa/min which was more than 100 times slower in comparison with 180 MPa/min used for separate cyclic uniaxial compression where no neutrons were present. This material exhibits time dependent mechanical behavior, i.e., it is rate sensitive. As there was more time allowed for domains switching in the latter, this also might contribute to the formation of stronger elastic anisotropy at lower applied stresses, causing the discrepancies between the experimental results.

An assumption is made that the initial state of $LaCoO_3$ is isotropic as it is a polycrystalline material, therefore no texture is present. The isotropic material shows a certain value of Young's modulus. After loading, texture develops which affects the modulus values. Therefore comparison of these values is of importance for better understanding of the material's behavior. The elastic modulus measured by excitation technique corresponds to the initial state of the material before loading (without texture). The loading modulus (from neutron diffraction data) in Figure 49 is a theoretical estimation of elastic modulus in the compression direction where a corresponding texture is taken into account at different applied stresses. The unloading modulus is an experimental value of the elastic modulus of $LaCoO_3$ in the compression direction corresponding to certain applied stress and formed texture. This value was measured at the beginning of unloading and, in fact, corresponded to the Young's modulus of the textured material obtained during loading up to a certain stress value. This way, the different values of Young's modulus can compared.

3.3.3. Conclusions

Elastic anisotropy in originally isotropic polycrystalline $LaCoO_3$ perovskite during the uniaxial compression has been studied. The texture formation and preferred domain orientation has been investigated. The lattice strains of individual (*hkl*) planes as well as average lattice strain were determined both for the planes oriented perpendicular and parallel to the loading direction. Utilizing average lattice strains as well as lattice strains along *a* and *c* crystallographic directions, an attempt was made to determine the Poisson's ratio, which was then compared to the Poisson's ratio value measured by impulse excitation technique. The elastic constants were calculated and Young's moduli of $LaCoO_3$ single crystal in different crystallographic directions were estimated. The verification of the obtained results were performed by estimation of the upper and lower bounds of elastic modulus of polycrystalline material as a function of applied compressive stress, which showed an excellent coincidence with Young's modulus values calculated from average lattice strain and macroscopic stress-strain deformation plot of sample used in neutron diffraction experiment. The question remains if neutron radiation or loading rates affect the elastic anisotropy of the material during uniaxial compression.

Table 7. Bulk properties of $LaCoO_3$ polycrystalline perovskite.

Property	**Value**
Porosity, %	4
Average grain size, µm	2-5
Young's modulus, GPa	76
Shear modulus, GPa	28.7
Poisson ratio	0.32

Table 8. Assignment of (*hkl*) planes to their respective orientation angles between the normal to diffraction plane and the c-axis.

Diffraction plane	**Angle (º)**
(006)	0
(018)	19.2
(208)	34.8
(024)	54.3
(202)	70.2
(220)	90

Table 9. The estimated compliance coefficients for $LaCoO_3$ single crystal, determined from experimental data for polycrystalline material.

Compliance Constants, GPa^{-1}				
S_{11}	S_{33}	S_{44}	S_{13}	S_{14}
$2.9x10^{-2}$	$3.81x10^{-3}$	$7.69x10^{-3}$	$-1.59x10^{-3}$	$-9.6x10^{-3}$

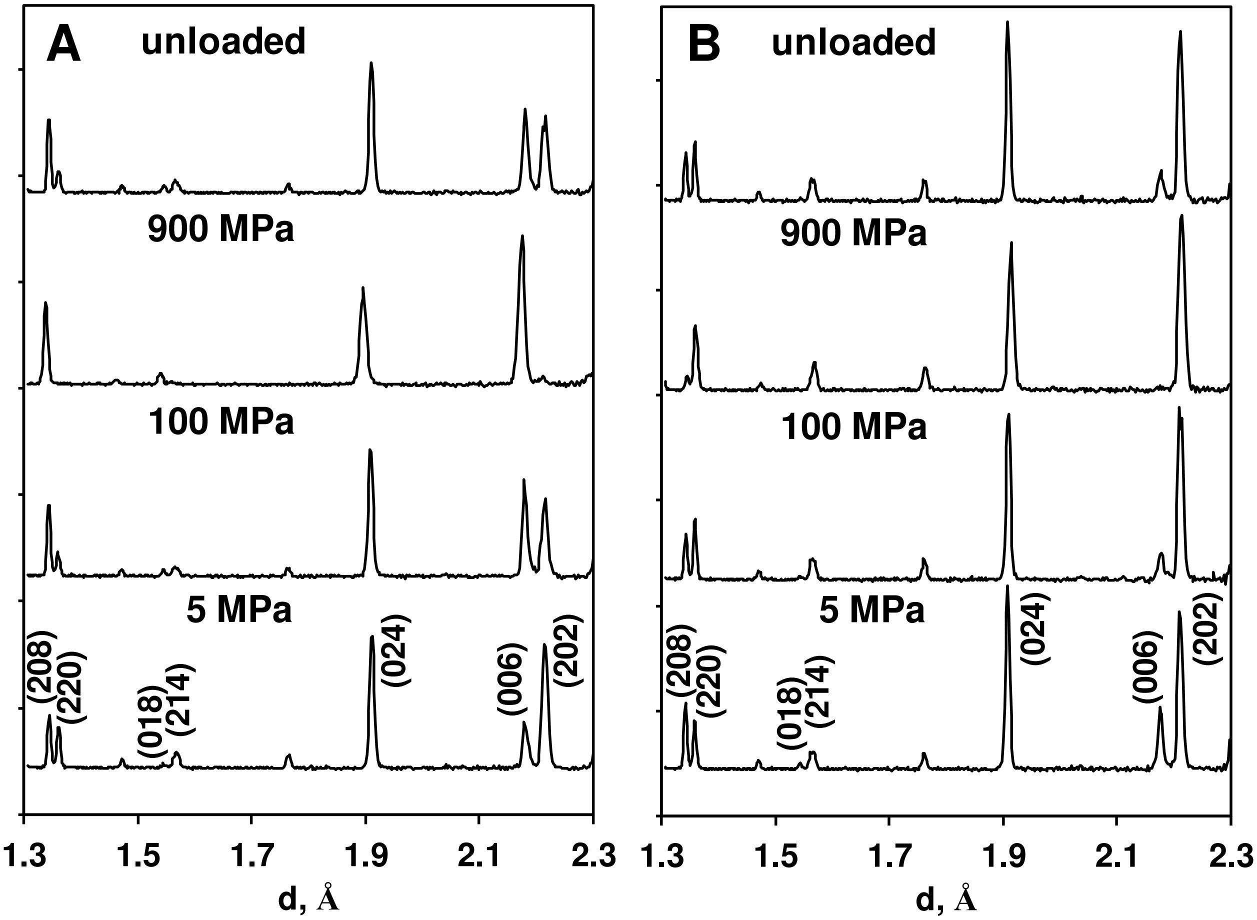

Figure 46. Neutron diffraction patterns of polycrystalline $LaCoO_3$ collected at different stress levels (5, 100, and 900 MPa) during uniaxial compression and after removal stress. (A) Diffraction patterns collected by Detector 1 in compression; (B) Diffraction patterns collected by Detector 2 in tension.

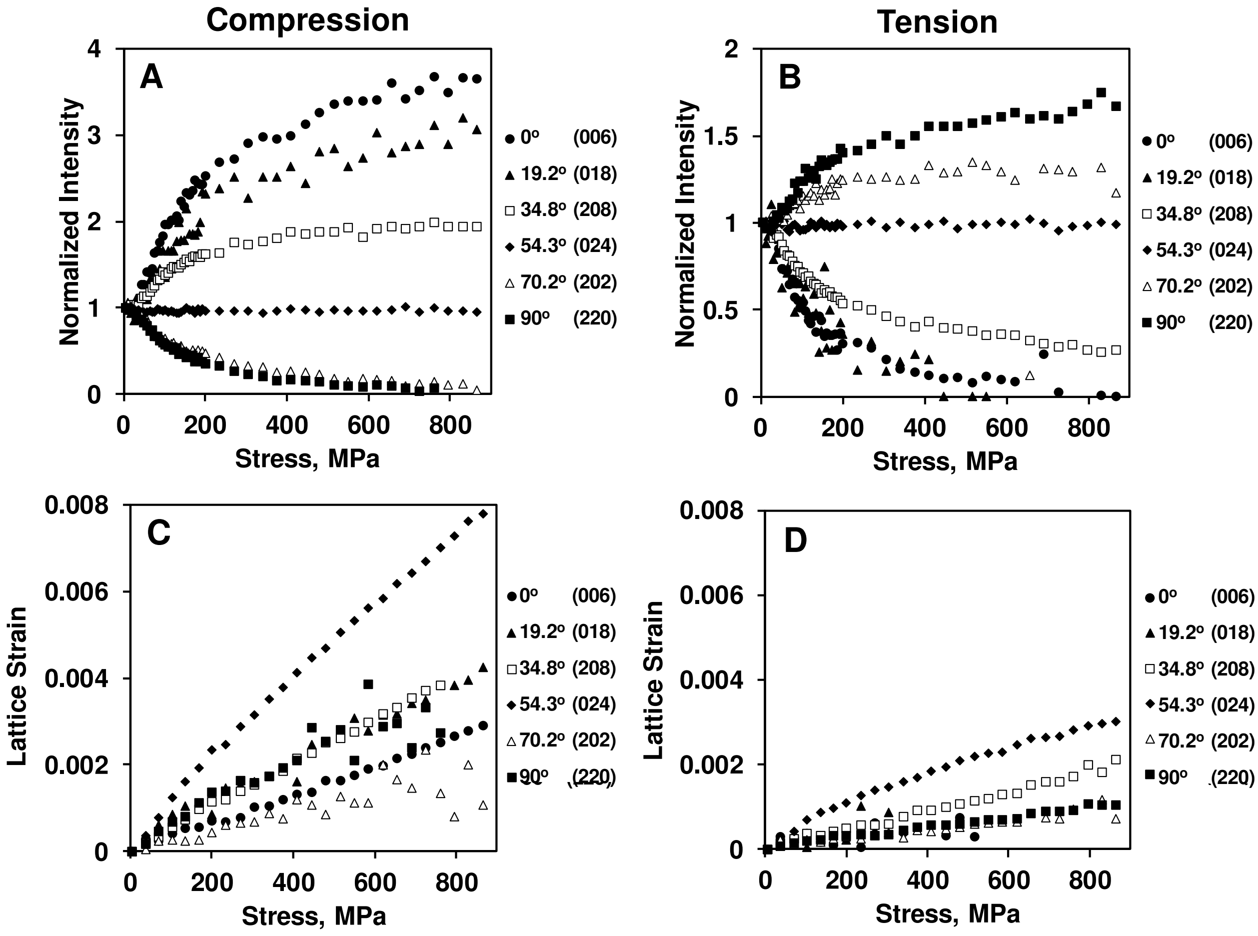

Figure 47. (A and B) Intensities of (006), (018), (208), (024), (202), and (220) diffraction peaks normalized by the intensity of the corresponding peak at the beginning of the loading. (C and D) The calculated lattice strain for six selected peaks. (A, C) Data collected by Detector 1; (B, D) Data collected by Detector 2.

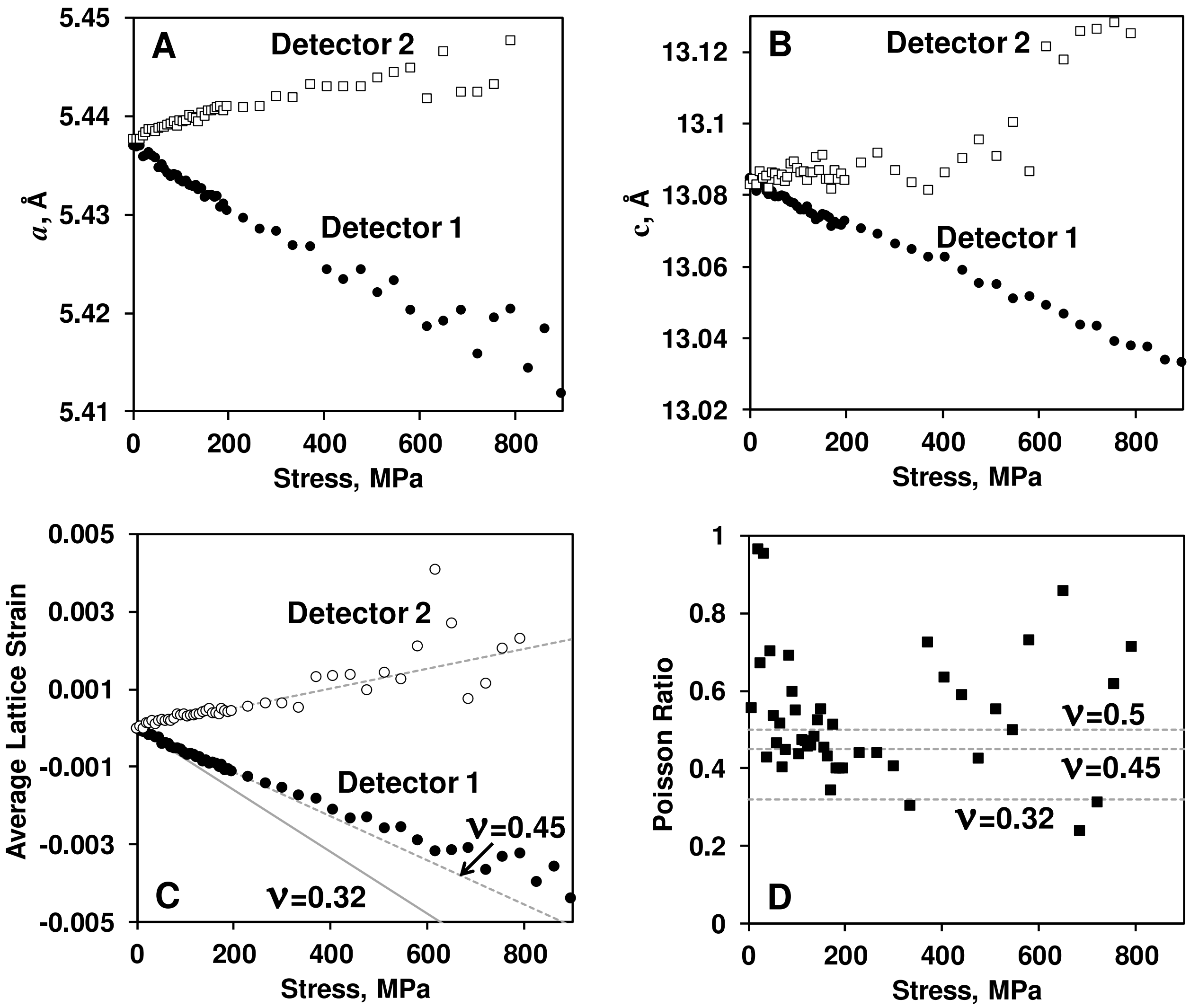

Figure 48. The a_i^{D1} and a_i^{D2} (A) and the c_i^{D1} and c_i^{D2} (B) lattice parameters of LaCoO3 presented as a function of applied stress. (C) The average lattice strain, calculated using the a_i^{D1}, c_i^{D1}, a_i^{D2}, and c_i^{D2} lattice parameters as a function of applied stress. The best fit lines are also shown to indicate the average radial and lateral strain values used for calculation of Poisson's ratio. In addition, radial strain value which can correspond to the measured Poisson's ratio by impulse excitation technique is also shown for clarity. (D) Poisson's ratio as a function of applied stress.

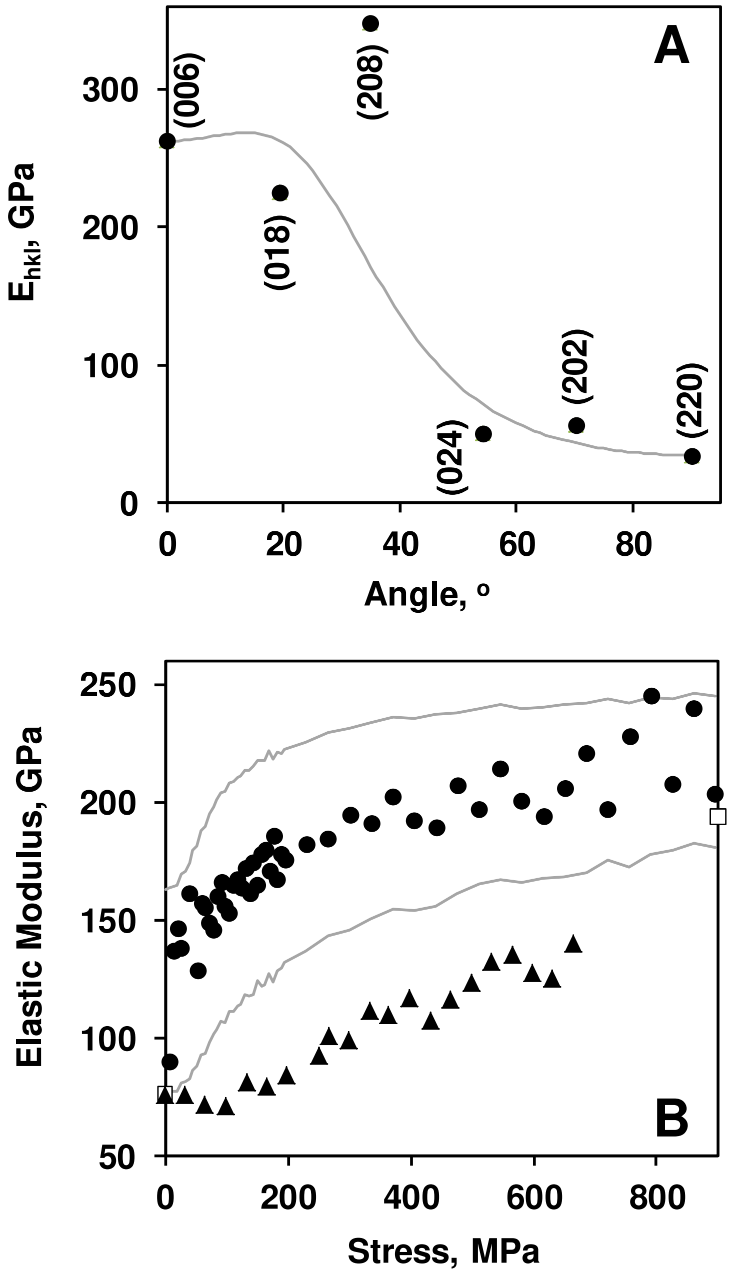

Figure 49. Calculated Young modulus for different crystallographic directions (solid line is the dependence for pure hexagonal lattice for comparison) (A) and corresponding estimated upper and lower boundaries (solid lines) for Young's modulus of polycrystal (B). Circles are the elastic modulus values measured utilizing average lattice strain. Squares are the elastic modulus values calculated as a slope of the macroscopic stress-strain deformation curve measured by the extensometer during neutron diffraction experiments. Triangles are the elastic modulus values measured in cyclic compression experiments where the incremental increase in load was applied.

3.4. High Temperature Elastic properties and Phase Transition in $LaCoO_3$ and $La_{0.8}Ca_{0.2}CoO_3$

The majority of the content of this section of the chapter is published in a paper co-authored by the author [143].

3.4.1. Introduction

Mixed Ionic Electronic Conducting (MIEC) $LaCoO_3$ based perovskites have been studied very extensively due to their unique and distinctive electronic, electrochemical, catalytic, and mechanical properties [55, 132, 144-149]. It was reported that polycrystalline $LaCoO_3$ based perovskites exhibit nonlinear ferroelastic behavior, which can be well explained by the kinetics of ferroelastic switching and corresponding changes in the cobaltite's microstructure and crystallographic orientation during loading [67]. The phenomena of domain switching and texture development were reported to be responsible for the appearance of elastic anisotropy and stress-strain hysteresis during deformation [67, 68]. It was also reported that at room temperature both pure $LaCoO_3$ and Ca doped $LaCoO_3$ have $R\bar{3}c$ low symmetry rhombohedral structure with a=5.378 Å and α=60.8° for pure $LaCoO_3$, and a=5.374 Å and α=60.72° for 20% Ca doped $LaCoO_3$, which is in perfect agreement with previously reported measurements [135, 150, 151]. Upon heating, the rhombohedral distortion in the lattice gradually decreases along with an increase in the lattice parameters up to the temperature at which a phase transition takes place to the high symmetry $Pm\bar{3}m$ cubic structure. Doping $LaCoO_3$ with cations like Ca^{2+} is known to reduce the lattice distortion and lower the transition temperature [152]. The $R\bar{3}c$ to $Pm\bar{3}m$ phase transition has been reported to occur above 1200°C for pure $LaCoO_3$ and at ~950°C for $La_{0.8}Ca_{0.2}CoO_3$, corresponding to the fact that a greater rhombohedral distortion at room temperature results in a higher transition temperature to cubic structure [152]. It is also know that the transition from the higher symmetry paraleastic phase to the lower symmetry ferroelastic phase leads to distortion in the cubic lattice, which results in spontaneous strain, and hence the lower symmetry phase has a non-linear deformation behavior. While only $R\bar{3}c$ rhombohedral structure was found at room temperature using most diffraction techniques, the existence of the lower symmetry monoclinic I2/a phase in $LaCoO_3$ based perovskite was confirmed by TEM and high-resolution synchrotron diffraction experiments. It is hard to detect in general by normal X-ray and neutron diffraction techniques due to the fact that the monoclinic distortion is very small and there are peaks overlapping peaks [153-155]. Vullum et al. also reported the presence of a monoclinic phase in $LaCoO_3$, even though they reported the monoclinic space group as $P2_1/m$ [156, 157].

It is important to mention that in our previous investigation of the thermal and mechanical properties of $LaCoO_3$ and $La_{0.8}Ca_{0.2}CoO_3$, a very unusual behavior was observed for pure lanthanum cobaltite [135]. At high temperatures (700-1000^oC), $La_{0.8}Ca_{0.2}CoO_3$ perovskite exhibits significant softening as expected and the value of Young's modulus decreases in comparison with the value at room temperature. On the other hand, pure $LaCoO_3$ exhibits an unexpected increase in Young's modulus with temperatures, varying from 76GPa at room temperature to 120GPa at 800^oC, a 30% increase in magnitude, while the lattice continuously expands from room temperature to 1000^oC as reported in [135]. The Young's modulus of $LaCoO_3$ and $La_{0.8}Ca_{0.2}CoO_3$ perovskites was measured from the loading portions of the stress-strain deformation curves obtained during 4-point bending experiments. The stiffening of $LaCoO_3$ reported in [135] was not explained and no detailed investigation into the unusual phenomenon was performed. In a paper by Raccah and Goodenough, the high temperature phase transition in $LaCoO_3$ was reported [59], however, these results were retracted in a later publication [150], where the explanation of the phase transition in $LaCoO_3$ was replaced by the appearance of the secondary Co_3O_4 oxide spinel phase as an impurity in $LaCoO_3$, thus leading to the disruptive changes in measured lattice parameters, that were erroneously assigned to the first order phase transition in $LaCoO_3$.

A summary of the many published results that have reported the variation of Young's modulus with temperature in different MIEC perovskites, all of them being of high relevance for their use in solid oxide fuel cells, was presented in [158]. This rather comprehensive review revealed that for certain perovskite compositions under certain experimental conditions, the Young's modulus decreases in the 100-600°C temperature range and then increases in the 700-1000°C temperature range [107, 159], while other materials with different perovskite compositions under similar or different experimental conditions showed the expected softening upon heating to 1000°C [160, 161]. A significant softening of $La_{0.8}Sr_{0.2}FeO_{3-\delta}$ and $La_{0.8}Sr_{0.2}Fe_{0.7}Ga_{0.3}O_{3-\delta}$ in the 200-400°C temperature range followed by an increase in the Young's modulus at 700-900°C was reported in [159].The phase transition occurring in the 700-900°C temperature range was considered to be responsible for the stiffening of the material in the higher temperature range (700-900°C) in $LaCoO_3$ based ceramics [159]. Similar softening followed by a small stiffening behavior of $La_{0.9}Sr_{0.1}Ga_{0.8}Mg_{0.2}O_{3-\delta}$ during heating to 1100°C was attributed to the successive structural changes in this perovskite material [162]. Changes both in Young's and shear moduli reported in [162] lead to the appearance of a significant discontinuity in the Poisson's ratio of $La_{0.9}Sr_{0.1}Ga_{0.8}Mg_{0.2}O_{3-\delta}$ at 600°C. A significant increase in measured Young's modulus of dense $La_{0.8}Sr_{0.2}MnO_3$ perovskite ceramics was reported to occur in the 600-1000°C temperature range, while no change in Young's modulus was found for the same composition when the ceramics had low density and an open pore structure [107]. A very large increase in Young's modulus of $La_{1-x}Sr_xMnO_3$ at high temperatures was also reported [158].

Similar stiffening of other mixed ionic electronic conducting ceramics was found in [107], where an increase in Young's modulus of $LaMnO_3$ and $LaFeO_3$ based perovskites in the 800-1000^{o}C temperature range was reported, however, again, no reasonable explanations were provided to explain this behavior.

In the current paper, the significant increase in Young's modulus of $LaCoO_3$ in the 700-1000^{o}C temperature range is reported, as measured using stress-strain deformation plots in four-point bending and sample resonance using the impulse excitation technique. For comparison, the properties of $La_{0.8}Ca_{0.2}CoO_3$ perovskite were also measured. Since the cobaltites exhibit non-linear deformation behavior upon loading, even at very small stresses, the Young's modulus cannot simply be directly determined from stress-strain data. Therefore, in the case of the four-point bending measurements the term "Young's modulus" will be replaced by the term "effective Young's modulus" in the paper. The detailed study of crystal structure of the two cobaltite compositions were done using powder X-ray diffraction as well as neutron diffraction.

3.4.2. Experimental

The $LaCoO_3$ and $La_{0.8}Ca_{0.2}CoO_3$ samples were sintered by Praxair Surface Technologies, Specialty Ceramics, USA; and machined by PremaTech Ceramics, USA. Three separate sample geometries were prepared – bars with dimensions 3mm x 4mm x 50mm for four-point bending experiments, bars with dimensions 50mm x 14mm x 14mm for impulse excitation measurements, and cylindrical pellets with 6mm diameter and 12mm length for compression testing.

The four-point bending tests of $LaCoO_3$ and $La_{0.8}Ca_{0.2}CoO_3$ samples were carried out at Empa, Swiss Federal Laboratories for Materials Science and Technology, Laboratory for High

Performance Ceramics, Switzerland. The samples were loaded with a 20 mm loading span and 40 mm supporting span. A Universal Testing Machine (UPM-Zwick 1478, Germany) was used for testing, in accordance with EN 843-1 standard [163]. The heating and cooling rate was set at 15°C/min, with a dwell time of 10 minutes for each temperature. The loading/unloading of the cobaltites was done up to a relatively small load to ensure that the maximum normal stress imposed on the sample during loading would be limited to ~8 MPa. As mentioned earlier, since the cobaltites exhibit non-linear deformation behavior, the ”true” Young’s modulus cannot be directly determined. Therefore, a method was adopted to estimate the “effective Young’s modulus” of the ceramics, the secant modulus from the force-displacement data. The secant modulus is defined as the slope of the straight line joining any given point in the stress-strain diagram to the origin. To estimate the effective Young’s modulus, first, the Secant modulus was plotted against applied stress. Then, the intercept of secant modulus-applied stress curve with the Secant modulus axis was considered as the effective Young’s modulus.

In addition, the Impulse Excitation Technique (IET) was used to determine the elastic modulus of the two materials for the same temperature range and intervals. The instrument used is a Grindo-Sonic Mk5 “Industrial” (J.W. Lemmens, Belgium), and the measurements were carried out in accordance with the EN 843-2 standard [164]. Samples, in the form of bars, of known density were lined up with a supporting cylinder and placed over a microphone. To determine the elastic modulus at room temperature using the natural frequency of vibration, the test bar was struck slightly using a small hammer and the acoustic vibrations were recorded using the microphone. Then using the dimensions of the sample, its density and natural frequency of vibration, the Young’s modulus was calculated. An electric furnace was used to heat the samples in air to the desired temperatures, with a dwell time of 30 minutes at each temperature. The samples were placed on a sample holder in the furnace and fixed with weights, and the microphone was again placed below the sample holder, and a similar procedure was followed to determine the elastic modulus at high temperatures. Instead of a small hammer, ZrO_2 or stainless steel balls with 4mm diameter were used to excite the samples.

Powder diffraction of the $LaCoO_3$ and $La_{0.8}Ca_{0.2}CoO_3$ samples was conducted using neutron diffraction and X-ray diffraction (XRD) techniques. All of the collected diffraction data were analyzed by Rietveld refinement using the General Structure Analysis System (GSAS) software [165] along with the graphical user interface (EXPGUI) [166]. The $LaCoO_3$ and $La_{0.8}Ca_{0.2}CoO_3$ samples used for these experiments were in the form of powders ground from the sintered cylindrical pellets.

The neutron powder diffraction experiments were conducted at the Spallation Neutron Source (SNS) and High Flux Isotope Reactor (HFIR) facilities at Oak Ridge National Laboratory (ORNL). At SNS the beamline 11A called POWGEN was utilized, which is a general-purpose powder diffractometer with a relatively high resolution of $0.001 < \Delta d/d < 0.016$. The powder samples were loaded into a quartz basket and placed in an air furnace. The temperature was raised from 100 ºC to a maximum of 820 ºC, and the diffraction data were collected at each designed temperature dwell for 0.5~1 h. The wavelength center of the neutrons was set at 1.333 Å, such that the time-of-flight neutron diffraction patterns covered a *d*-spacing range of 0.41 to 3.61 Å.

The experiment at HFIR was conducted on the HB-2A High Resolution Neutron Powder Diffractometer. The HB-2A is an instrument that is helpful in crystal structural studies under varying conditions like pressure and temperature, and helps determine atomic positions, atomic displacement, atomic occupancies and phase transition. The HB-2A has a bank of 44 ^3He tubes, each with 12' Soller collimators arranged in a Debye-Scherrer geometry. The monochromator used is a Ge [115] corresponding to a wavelength of 1.1538 Å. The sample in the form of a pellet of 6mm diameter, 12 mm length was heated in a quartz tube within an air furnace. Quartz wool was placed on top of the sample to avoid any contamination from escaping out into the environment. Two thermocouples were used to monitor the sample and environment temperatures. The temperature of the sample was varied from 200ºC to 1050ºC in intervals of about 50ºC; a scan at 11ºC was also conducted. The time allotted for the temperature of the samples to stabilize was 20 minutes for each temperature. The time required per scan was approximately 68 minutes.

The high temperature X-ray diffraction was conducted at the High Temperature Materials Laboratory (HTML) at ORNL using a PANalytical X'Pert PRO MPD diffractometer with an Anton-Paar XRK-900 high temperature stage. Powder diffraction was performed for cylindrical samples. The data was collected in the 2θ range of 10º-80º with a count time of 30 seconds resulting in a scan duration of less than 5 minutes, using Cu Kα radiation at 45 kV and 40mA. The use of an X'celeraotor detector allowed fast data collection.

3.4.3. Results and Discussion

Stress-strain curves of $LaCoO_3$ and $La_{0.8}Ca_{0.2}CoO_3$ ceramics obtained under uniaxial compression are shown in Figure 50. Both materials exhib`it ferroelastic hysteresis, which was well characterized in our previous work [67, 132, 167, 168]. The inserts in Figure 50 show stress-strain plots obtained both in uniaxial compression during loading (dashed line) and, for comparison, in four point bending during loading/unloading up to 8 MPa (solid line) and shows a good overlap of the data from the two tests.

The stress-strain hysteresis plots of $LaCoO_3$ and $La_{0.8}Ca_{0.2}CoO_3$ as a function of temperature for heating and cooling are shown in Figure 51. Hysteresis loops were obtained in both perovskites at almost all temperatures with the only exception that an almost straight line and no hysteresis is visible for loading/unloading of $La_{0.8}Ca_{0.2}CoO_3$ at room temperature. The characteristic features of hysteresis of $LaCoO_3$ and $La_{0.8}Ca_{0.2}CoO_3$ on loading/unloading at different temperatures obtained from the results presented in Figure 51. The hysteresis area of $LaCoO_3$ is larger in comparison with Ca doped $LaCoO_3$ at room temperature as well as at 100^{o}C (Figure 52A and B). However, beginning at 200^{o}C there is a significant increase in the hysteresis area measured for Ca doped cobaltite, when the values of hysteresis area increase to almost 300 Pa upon heating, whereas for pure $LaCoO_3$ an increase of hysteresis area was also detected but the values at 200^{o}C were in the range of 100 Pa both upon heating and cooling, which is three times less than those of Ca doped $LaCoO_3$. The trend shows an increase in the hysteresis area between 200^{o}C to ~400^{o}C for both compounds, and then a decrease up to 800^{o}C, followed by a slight increase in the value for $LaCoO_3$ and a large increase for Ca doped $LaCoO_3$. The largest area of hysteresis loop was measured for $La_{0.8}Ca_{0.2}CoO_3$ at 1000^{o}C when plastic deformation, most likely caused by the movement of dislocations, was present (Figure 51C and D). Other parameters, such as irreversible strain, showed similar trends for pure and Ca doped $LaCoO_3$ (Figure 52C and D). Both hysteresis areas and irreversible strains increased in the 200-400^{o}C temperature range for both compositions. Both hysteresis areas and irreversible strains slightly decreased in the 700-1000^{o}C temperature range for pure $LaCoO_3$, however in the 600-700^{o}C temperature range the hysteresis area, irreversible and even maximum strains decreased for Ca doped $LaCoO_3$, while at the higher 900-1000^{o}C temperature range, especially at 1000^{o}C, all three parameters increased dramatically for $La_{0.8}Ca_{0.2}CoO_3$ (Figure 52E and F). The effective Young's modulus of both compounds showed contrasting behavior upon heating (Figure 52G and H). As the effective Young's modulus strongly depends on the bond strength and bond length of the compound, as temperature increases the bond strength decreases as the bond length increases, thus bringing down the stiffness of the bonds causing the expected softening of the material at high temperature. The effective Young's modulus of $LaCoO_3$ remains equal to ~80 GPa at room temperature and at 100°C, the perovskite slightly softens at 200-400°C until the value reaches ~75 GPa. However, starting from 600-700°C the effective Young's modulus value increases close to 120 GPa at 800°C (Figure 52G). The effective Young's modulus values measured from the loading portion of the stress-strain deformation plot taken at the very beginning of the loading and the Young's modulus measurements taken from impulse excitation technique coincide well (Figure 52G). However, for $La_{0.8}Ca_{0.2}CoO_3$, the effective Young's modulus behavior is very different from the behavior of pure $LaCoO_3$ upon heating (Figure 52H). As can be seen in Figure 52H, the effective Young's modulus of $La_{0.8}Ca_{0.2}CoO_3$ is ~135 GPa both at room temperature and 100°C, but upon further increase in temperature the effective Young's modulus decreases to ~50 GPa at 1000°C, exhibiting the expected softening behavior. Thus, unusual stiffening behavior of $LaCoO_3$ where effective Young's modulus increases significantly upon increase of temperature, is observed and needs to be understood.

While there have been many studies done of the crystal structure, phase composition, lattice parameters and other aspects including Co ion spin states of $LaCoO_3$ using neutron diffraction and X-ray diffraction in the past [169-172], the purpose of this study was to present an even more comprehensive high temperature neutron and X-ray diffraction study to clarify the changes in the crystal structure and lattice parameters of both pure and Ca doped $LaCoO_3$. The room temperature neutron and X-ray diffraction patterns of LaCoO3 and La0.8Ca0.2CoO3 perovskites are shown in Figure 53. The refinement results from powder diffraction patterns taken on the HB-2A instrument at HFIR and POWGEN instrument at SNS at ORNL coincide well with the X-ray diffraction (XRD) patterns taken using the X-ray diffractometer at the High Temperature Materials Laboratory at ORNL. Only peaks belonging to $LaCoO_3$ based perovskite structure were indexed and thus phase pure rhombohedral $R\bar{3}c$ structure was identified; a schematic of the unit cell and bonds in the cobaltite's lattice are shown in Figure 54. Both rhombohedral and hexagonal lattice unit cells are shown in Figure 54A and B, as well as the characteristic bond lengths of Co-O and La-O, as seen in Figure 54C and D respectively. The O-Co-O bond angle (Figure 54C), O-La-O bond angle (Figure 54D) and the Co-O-Co angle (Figure 54E) between two octahedrons are also shown. The diffraction patterns of pure $LaCoO_3$ and $La_{0.8}Ca_{0.2}CoO_3$ perovskites taken at different temperatures are shown in Figure 55. Peaks that belong to only the rhombohedral $R\bar{3}c$ structure are observed and lattice expansion is observed as the temperature increases. Examples of Rietveld refinement results for $LaCoO_3$ are shown at 11^{o}C (Figure 57A) and 1000^{o}C (Figure 57C), and for $La_{0.8}Ca_{0.2}CoO_3$ are shown at 11^{o}C (Figure 57B) and 1000^{o}C (Figure 57D) from data collected at HFIR. The fitting parameters wRp, Rp and reduced $\chi 2$ were found to be in the range of 3.9%–5%, 3.1%–4% and 0.84–1.3, respectively The rhombohedral a and c lattice parameters as well as the volume of the unit cell as a function of temperature are shown in Figure 58. There is good correspondence between lattice parameters and volume of the two compounds as measured by three different methods – two of them by neutron diffraction and one by X-ray diffraction. The smooth evolution of lattice parameters and cell volume as a simple thermal response of the lattice indicates the absence of phase transition in the two materials. It is possible to see from the corresponding lattice parameters, that the thermal expansion and increase in "*a*" lattice parameter was much larger for pure $LaCoO_3$ in comparison with $La_{0.8}Ca_{0.2}CoO_3$. As one can see from Figure 58A and D, the "*a*" lattice parameters are rather similar at room temperature for both compounds (5.37-5.38 Å) but there is a difference at high temperatures - 5.537±0.00117 Å for $LaCoO_3$ and 5.505±0.00100 Å for $La_{0.8}Ca_{0.2}CoO_3$ at 1000°C. There is no indication of any significant changes in the thermal expansion of $LaCoO_3$ which might correlate and account for the measured increase in effective Young's modulus of this compound. The change in the rhombohedral angle with temperature of the two compounds reveals that $La_{0.8}Ca_{0.2}CoO_3$ perovskite has a ferroelastic phase transition at ~1050°C with $\alpha=60^\circ\pm0.005^\circ$ ($\alpha=60^\circ$ for cubic phase), whereas $LaCoO_3$ is still rhombohedral ($\alpha=60.18^\circ\pm0.009^\circ$) even at 1050°C (Figure 58).

There are significant differences in the variation of Co-O, La-O bond lengths and O-Co-O, Co-O-Co, O-La-O bond angles with temperature, between pure $LaCoO_3$ and $La_{0.8}Ca_{0.2}CoO_3$ compositions (Figure 58 and Figure 59). Co-O and La-O bond lengths increase much faster in pure $LaCoO_3$ upon heating in comparison with $La_{0.8}Ca_{0.2}CoO_3$. The O-Co-O bond angle approaches 90° at 1100°C for $La_{0.8}Ca_{0.2}CoO_3$ indicating that the structure becomes close to cubic, whle for pure $LaCoO_3$ the structure still has a significant distortion and remains rhombohedral at all temperatures. The geometric tolerance factor approaches 1 for $La_{0.8}Ca_{0.2}CoO_3$ at 1050°C, but for pure $LaCoO_3$ it is remains at 0.996. Thus, despite the significant increase in effective Young's modulus of pure $LaCoO_3$ at 700-900°C, the lattice expansion and bond lengths/angles do not provide any clear answer as to why the effective Young's modulus increases.

Refinement for oxygen occupancies for the two compounds from neutron diffraction results was inconclusive. There was no discernable trend as far as the amount of oxygen vacancies as a function of temperature that can be inferred, as seen in Figure 60(A, B). The Atomic Displacement Parameter, presented as U_{iso} for isotropic case in the refinement, characterizes the thermal vibration of the oxygen atoms, plotted against temperature for the two compounds as shown in Figure 60 (C, D). It is expected to have a higher value at elevated temperatures due to stronger thermal vibrations. However, the value can be also high if the structure locally involves incoherent static distortions [173] of the CoO_6 octahedra. The incoherent atomic displacements with respect to the lattice-averaged positions may not contribute to additional Bragg's reflection, but will mimic large Debye-Waller factors. This effect is hard to differentiate from that owing to the thermal vibrations in the diffraction patterns. From the plots in Figure 60 (C, D), there is a change in slope for $LaCoO_3$ at about 500°C, which coincides with the temperature at which there is an increase in its effective Young's modulus. In contrast, there is no change in slope for $La_{0.8}Ca_{0.2}CoO_3$ that can be observed, and the effective Young's modulus continues to decrease with increasing temperature. Therefore, it is proposed that at high temperatures, some static distortions occur in $LaCoO_3$ but not in $La_{0.8}Ca_{0.2}CoO_3$. With the local static distortions, the atom's position can differ from the lattice-averaged sites, and therefore the true bond lengths cannot be precisely calculated from the "characteristic bond lengths" by the refinement. The subtle static distortions changes indicated by U_{iso} parameter lead to the variation in local bond lengths (true bond lengths) and may be responsible for the effective Young's modulus increase. Nevertheless, this mechanism cannot be fully verified by the current data. The change in local bond lengths could also be explained by the different valence and spin states of Co atoms. For these effects different directions, locally, there may be multiple modes of $Co\text{-}O_6$ octahedron distortions in the perovskite. These are possible mechanisms, although not explicit, that could explain the effect that static distortions have on the anomalous behavior of U_{iso} with temperature in $LaCoO_3$.

From the X-ray and neutron diffraction analysis, the structure of $LaCoO_3$ based perovskites was identified as rhombohedral $R\overline{3}c$ (D_{3d}^6) structure, and according to the factor group analysis for D_{3d}^6 rhombohedral perovskites only five Raman active phonon modes of irreducible representation $A_{1g}+4E_g$ are allowed [174]. It was found in the previous work [175] that there are five active Raman peaks in pure $LaCoO_3$ when measurements were taken from the as-machined surface. When the sample is heated up to 900°C the effect of the strain at the surface associated with machining disappears [176]. Raman spectra were collected for the two compositions during heating from room temperature up to 900°C, and cooling back down to room temperature, as shown in Figure 61 and Figure 62. In Figure 62, two low frequency modes 160 cm^{-1} (1) and 185 cm^{-1} (2) are present in the low frequency region, and two intermediate frequency modes 450 cm^{-1} (3) and 550 cm^{-1} (4), along with a strong 700 cm^{-1} (5) mode are detected for pure $LaCoO_3$. All of these peaks remain present on heating up to 900°C for both $LaCoO_3$ and $La_{0.8}Ca_{0.2}CoO_3$. The peak intensities decrease and peak widths increase upon heating to 900°C. For $LaCoO_3$ the 450 cm^{-1} and 550 cm^{-1} peaks, even as they weaken, remain separate even at 900°C; in contrast to $La_{0.8}Ca_{0.2}CoO_3$ for which the 450 cm^{-1} peak slowly disappears upon heating and only the 550 cm^{-1} could be seen at 900°C. There are two other important differences in the Raman spectra of pure and Ca-doped $LaCoO_3$. First, for the $La_{0.8}Ca_{0.2}CoO_3$ perovskite there is only one 185 cm^{-1} peak present in the low frequency region, as can be seen in Figure 62. Second, for Ca-doped $LaCoO_3$ the 400 cm^{-1} (3') peak is more clearly present at room temperature and then weakens, but for pure $LaCoO_3$ the 400 cm^{-1} peak is hardly seen at room temperature but it becomes more prominent in the temperature range of 200-400°C. To summarize, there is no significant change in the Raman spectra that could be indicative of any structural changes that would provide a realistic explanation as to why effective Young's modulus of $LaCoO_3$ increases so dramatically upon heating.

One of the possible explanations for the increase of effective Young's modulus of pure $LaCoO_3$ could be connected to the strong elastic anisotropy of this compound. As it was established in [68], a strong texture formed during the loading of this perovskite at room temperature, when the volume of the domains with a higher elastic modulus along loading direction increased thus leading to an increase in observed effective Young's modulus. Increase in temperature could bring about a significant increase in the mobility of the domain walls and, therefore, formation of texture might easily be facilitated, resulting in an increase in the effective Young's modulus at much lower applied stress, such as for example 8 MPa as it was applied in the current study. By providing such explanation though, one has to take precaution – the increase in temperature of the material not only allows for texture formation process to occur, but the increase in temperature also leads to decrease in the elastic constants that occurs simultaneously which leads to a reduction in the effective Young's modulus. The overall changes in effective Young's modulus would depend on these two processes – increase in the volume of the domains with a certain crystallographic orientations along the load direction as well as changes in the elastic constants – as a function of temperature.

Another factor that could contribute to the stiffening or softening behavior in the two compounds is the pinning effect of oxygen vacancies on the movement of domain walls. It has been reported that in perovskites such as $Ca_{1-x}Sr_xTiO_3$, oxygen vacancies or clusters of oxygen vacancies pin the domain walls, thus impeding the movement of domain walls and softening of the material [177-179]. In Ca-doped $LaCoO_3$, the number of oxygen vacancies is higher due to doping with Ca and the number of vacancies should increase with temperature as more oxygen atoms leave the lattice at higher temperature, the density of clusters of oxygen vacancies is thus predictably much higher at high temperatures compared to pure $LaCoO_3$, thus the pinning effect of these clusters and the eventual softening that occurs could be much more significant in Ca-doped $LaCoO_3$, whereas in pure $LaCoO_3$ the mobility of the domain walls can still be the dominating phenomenon. This means that the domain wall mobility phenomenon dominates and leads to stiffening in pure $LaCoO_3$, and for Ca-doped $LaCoO_3$ the pinning effect due to large number of oxygen vacancy clusters dominates and leads to softening. To verify such hypotheses in-situ stress-strain X-ray or neutron diffraction experiments would be required, and this might be a subject of future work.

3.4.4. Conclusions

The stress-strain deformation behavior of $LaCoO_3$ and $La_{0.8}Ca_{0.2}CoO_3$ was studied by loading the ceramics to a low stress of 8 MPa in four-point bending at RT – 1000 °C temperature range. The changes in hysteresis loops were significant in the 200-500 °C range and at 1000 °C for both $LaCoO_3$ and $La_{0.8}Ca_{0.2}CoO_3$, however, the changes in the hysteresis loop area for $La_{0.8}Ca_{0.2}CoO_3$ was much more substantial. A very unusual phenomenon was noticed in $LaCoO_3$ – significant stiffening of the ceramic in the 700-900 °C temperature range. The effective Young's modulus of $LaCoO_3$ at room temperature was recorded as ~76 GPa, however, its value increased dramatically beginning around 700 °C to a value of ~120 GPa at 900 °C. In the case of $La_{0.8}Ca_{0.2}CoO_3$, softening behavior was recorded, as in the case for most materials, under the same testing conditions. High temperature XRD along with neutron diffraction and micro-Raman spectroscopy were used in order to clarify such behavior in the two cobaltites. While many useful crystal lattice parameters along with vibrational behavior of the two ceramics were derived, the cause of high temperature stiffening of $LaCoO_3$ is still not clear. As the temperature was increased, lattice expansion was noticed in both cobaltites as expected. As the lattice expands, an increase in bond lengths was observed and as a result the bond strength is expected to decrease leading to a decrease in the effective Young's modulus for both $LaCoO_3$ and $La_{0.8}Ca_{0.2}CoO_3$. Yet, this is not the case with $LaCoO_3$ and thus more research is required to shed light on and find the exact physical phenomenon responsible for such tremendous increase in stiffness of this material.

3.5. Acknowledgement

Funding: This work was supported by the National Science Foundation [grant numbers: 0968911, 1030833, 0748364]. A portion of this research at ORNL's High Flux Isotope Reactor and Spallation Neutron Source, was sponsored by the Scientific User Facilities Division, Office of Basic Energy Sciences, U.S. Department of Energy.

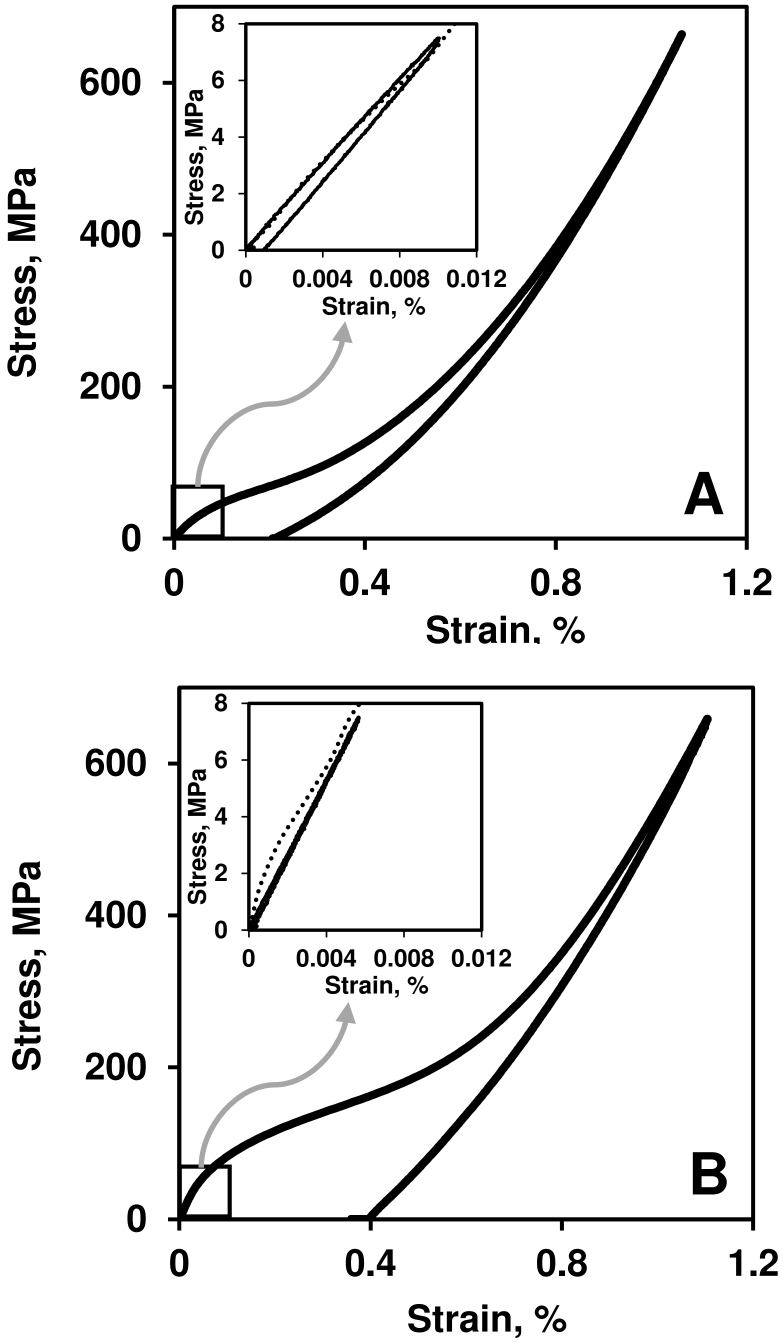

Figure 50. Stress-strain curve during uniaxial compressive loading and unloading for (A) $LaCoO_3$ and (B) $La_{0.8}Ca_{0.2}CoO_3$. The inset portions of the curves in the two figures show the initial portion of the stress-strain curve from uniaxial compressive loading (dotted line) plotted with stress-strain curve from four-point bending for the two compounds.

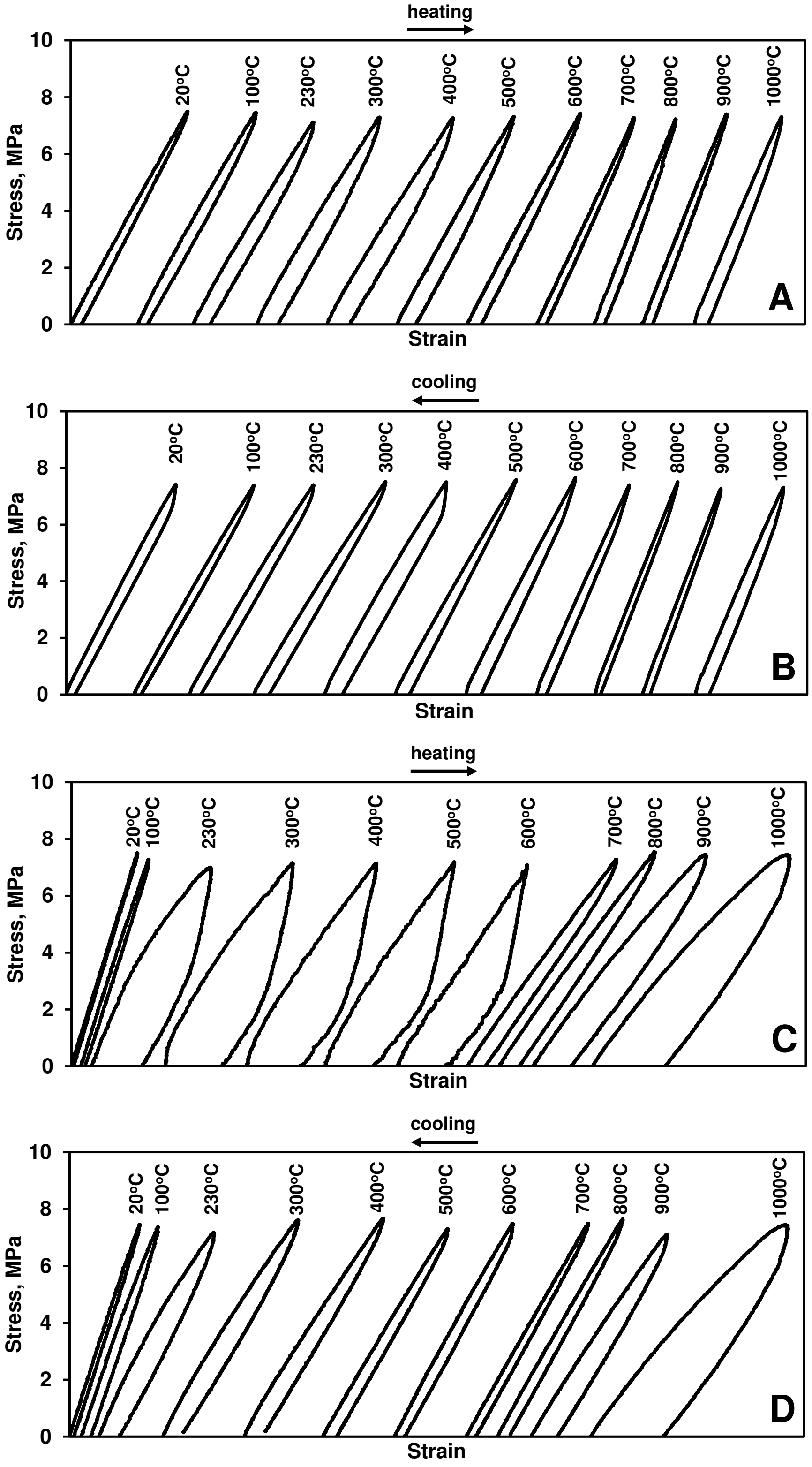

Figure 51. Stress-strain curves obtained from four-point bending of $LaCoO_3$ during (A) heating from room temperature to 1000°C and for (B) cooling back to room temperature. Similarly, stress-strain curves of $La_{0.8}Ca_{0.2}CoO_3$ during (C) heating from room temperature

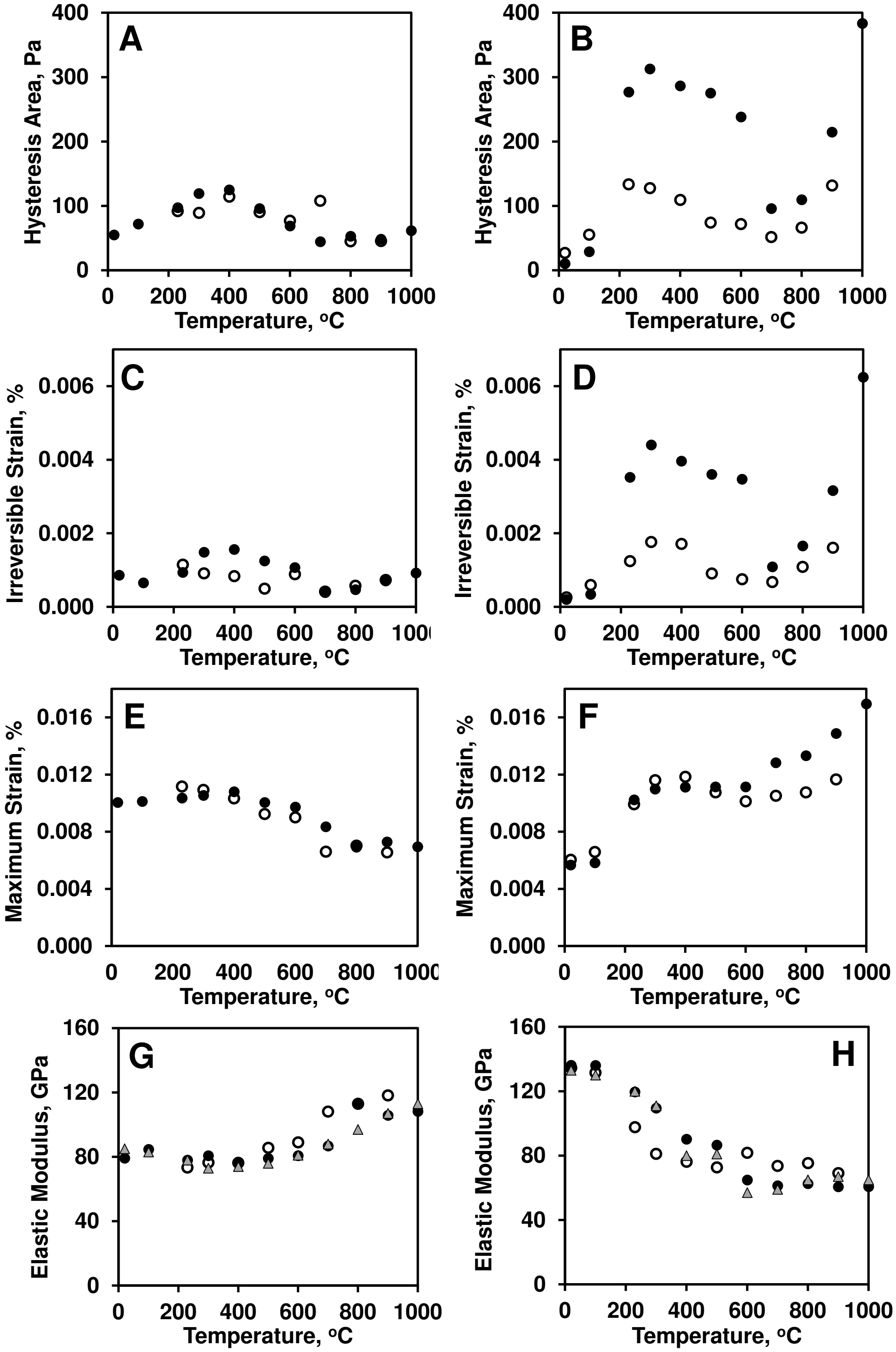

Figure 52. The dependence of (A) hysteresis area, (C) irreversible strain, (E) maximum strain, and (G) elastic modulus with temperature in LaCoO$_3$ during mechanical loading and unloading; and the dependence of (B) hysteresis area, (D) irreversible strain, (F) maximum strain, and (H) elastic modulus with temperature in La$_{0.8}$Ca$_{0.2}$CoO$_3$. Solid circles correspond to heating, open circles correspond to cooling. Triangles are the values measured by Impulse Excitation Technique.

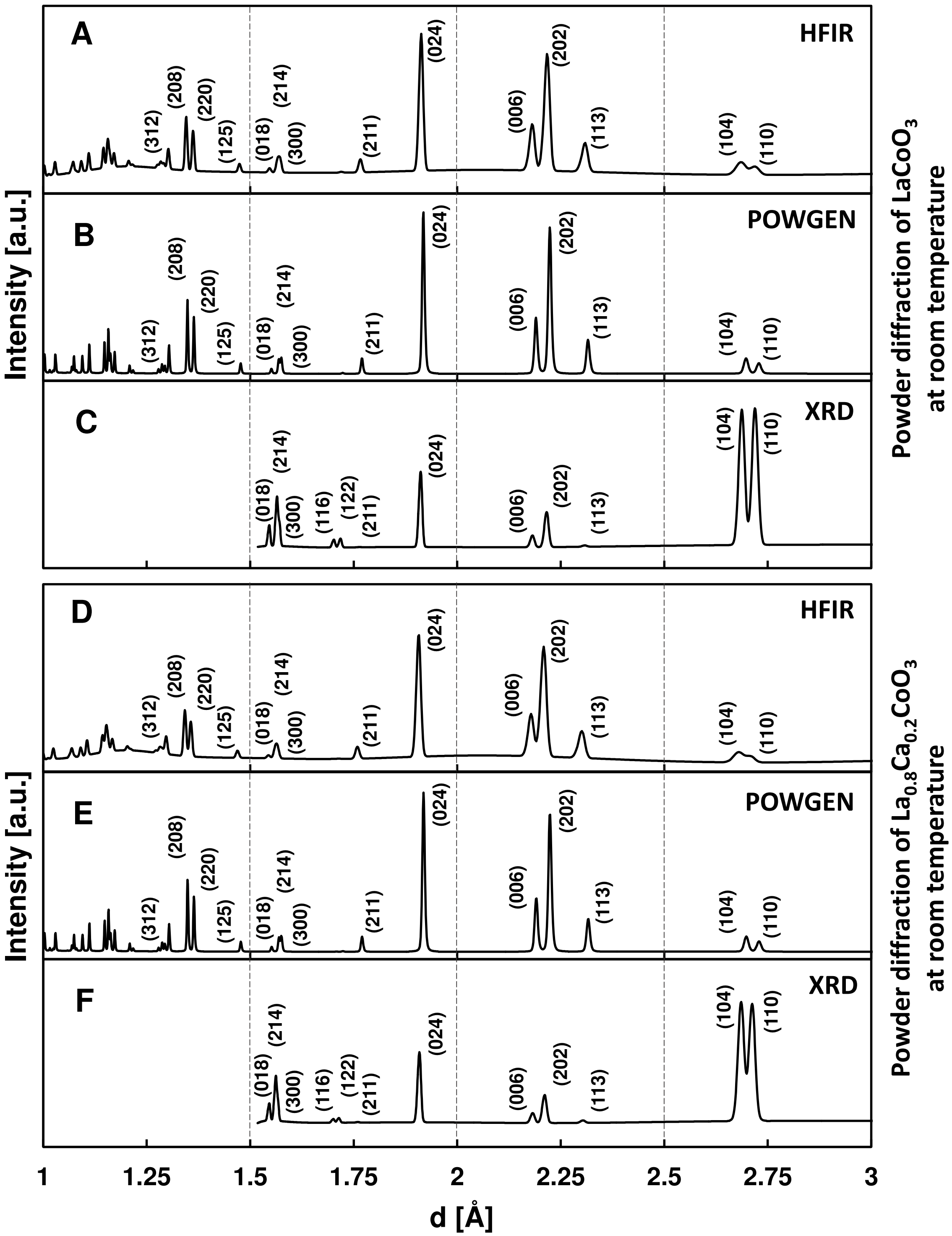

Figure 53. The diffraction patterns for $LaCoO_3$ sample at or near room temperature from neutron diffraction at (A) High Flux Isotope Reactor, (B) Spallation Neutron Source and from (C) X-ray diffraction at High Temperature Materials Laboratory. The diffraction patterns for $La_{0.8}Ca_{0.2}CoO_3$ sample at or near room temperature from neutron diffraction at (D) HFIR, (E) POWGEN and from (F) X-ray diffraction at High Temperature Materials Laboratory.

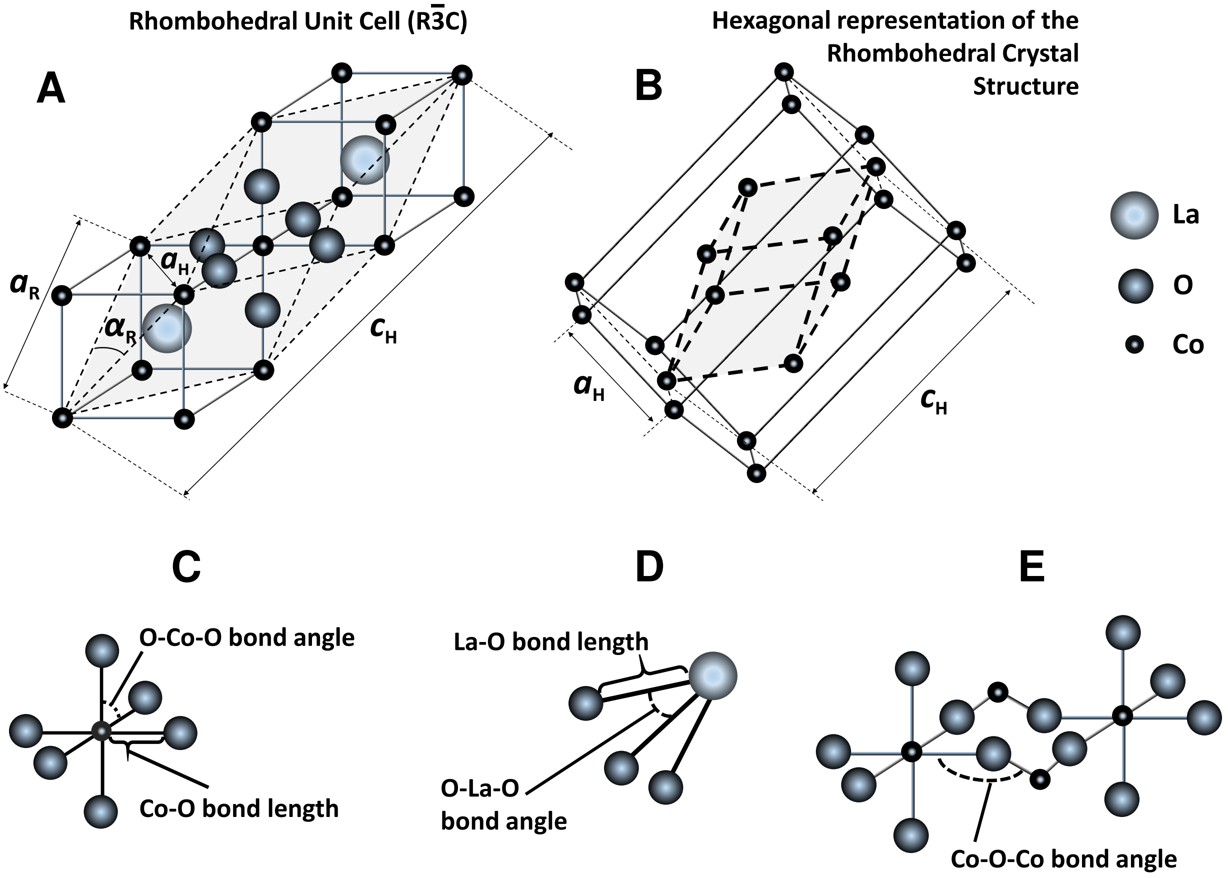

Figure 54. Schematic showing (A) the rhombohedral unit cell of $LaCoO_3$, space group $R\bar{3}C$, (B) hexagonal representation of the rhombohedral crystal structure, (C) the bond length and bond angle between Co and O atoms in the Co-O octahedron, (D) the bond length and bond angle between La and O atoms, (E) the Co-O-Co bond angle between adjacent octahedrons.

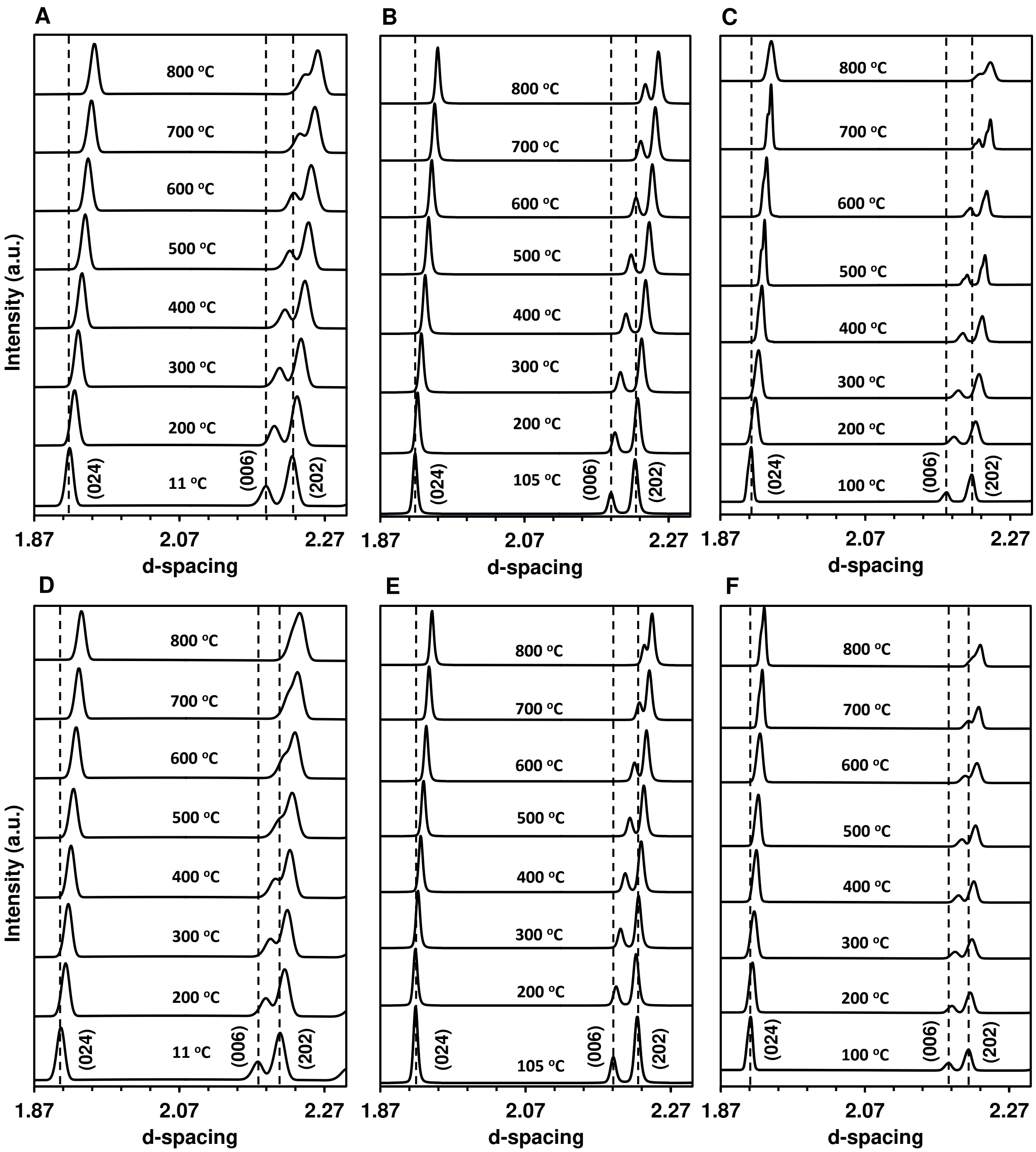

Figure 55. The change in diffraction patterns of $LaCoO_3$ and $La_{0.8}Ca_{0.2}CoO_3$ collected on different instruments during heating. The evolution of the single peak (024) and the doublet (006)/(202) in $LaCoO_3$ from the data collected at HFIR, POWGEN and HTML can be seen in (A), (B) and (C). Accordingly the evolution of the same peaks in $La_{0.8}Ca_{0.2}CoO_3$ are shown from the data collected at HFIR, POWGEN and HTML can be seen in (D), (E) and (F).

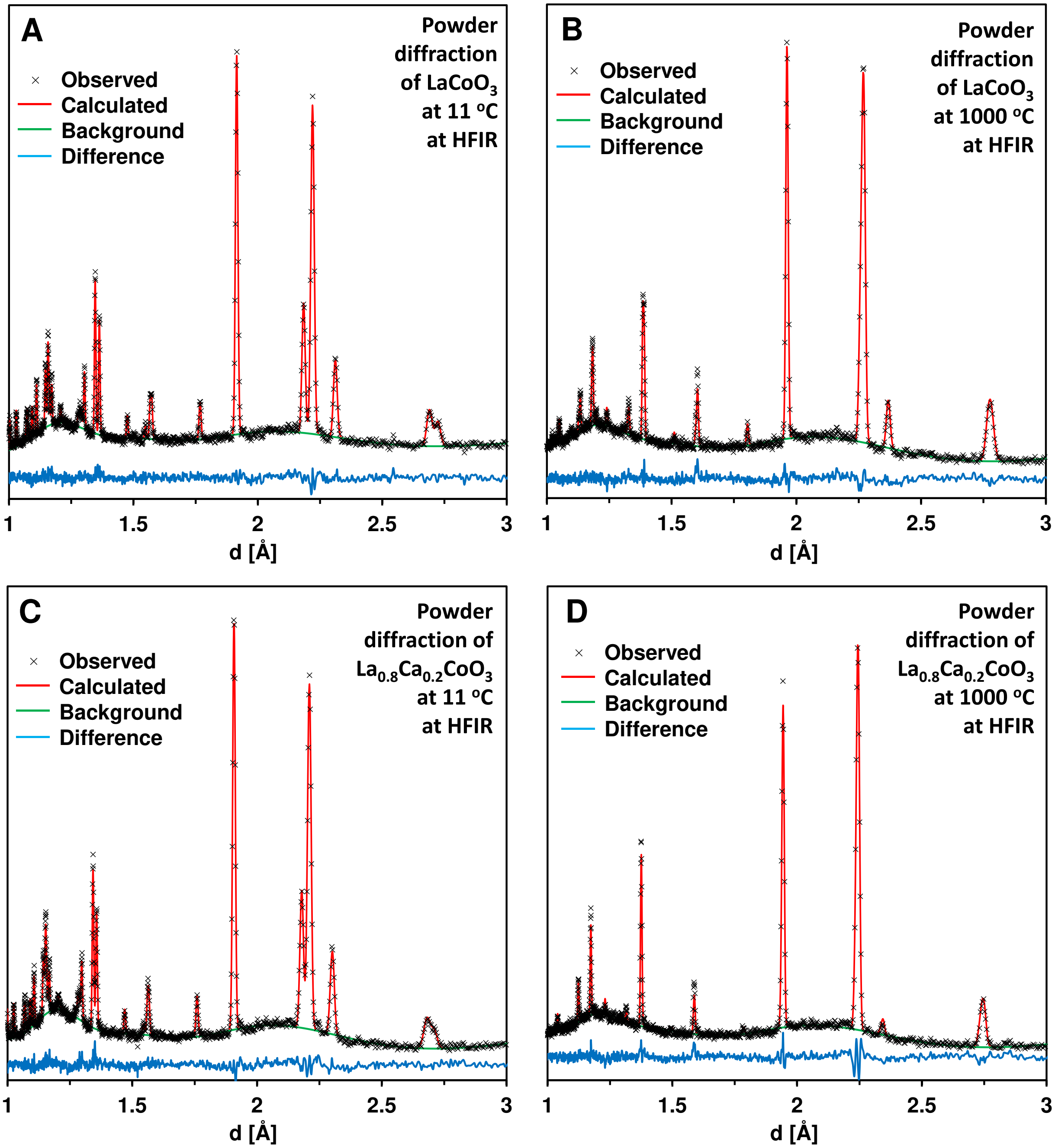

Figure 56. Neutron diffraction patterns after Rietveld refinement for $LaCoO_3$ from the data collected at HFIR for (A) 11°C and (B) 1000°C. Neutron diffraction patterns after Rietveld refinement for $La_{0.8}Ca_{0.2}CoO_3$ from the data collected at HFIR for (C) 11°C and (D) 1000°C. As can be seen, the calculated diffraction pattern (red line) matches well with the observed diffraction pattern (black cross markers) with minimal errors (blue line). The background (green line) is also seen to be fit well.

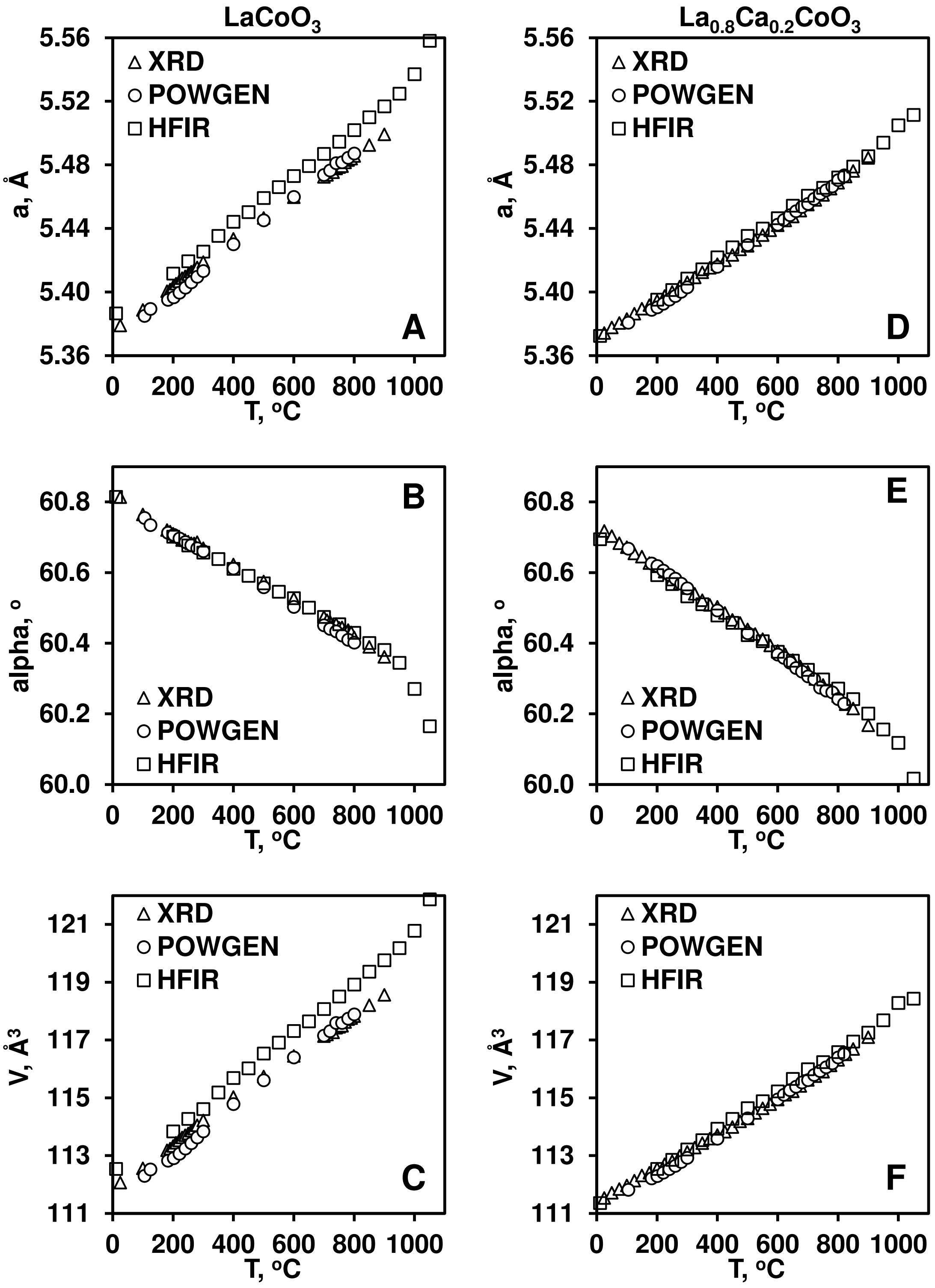

Figure 57. (A, B, C) Variation of lattice parameters and unit cell volume in rhombohedral system during heating and cooling of $LaCoO_3$ from the data collected via XRD at HTML, neutron diffraction at POWGEN and HFIR. (D, E, F) Variation of lattice parameters and unit cell volume in rhombohedral system during heating and cooling of $La_{0.8}Ca_{0.2}CoO_3$ from the data collected via XRD at HTML, neutron diffraction at POWGEN and HFIR.

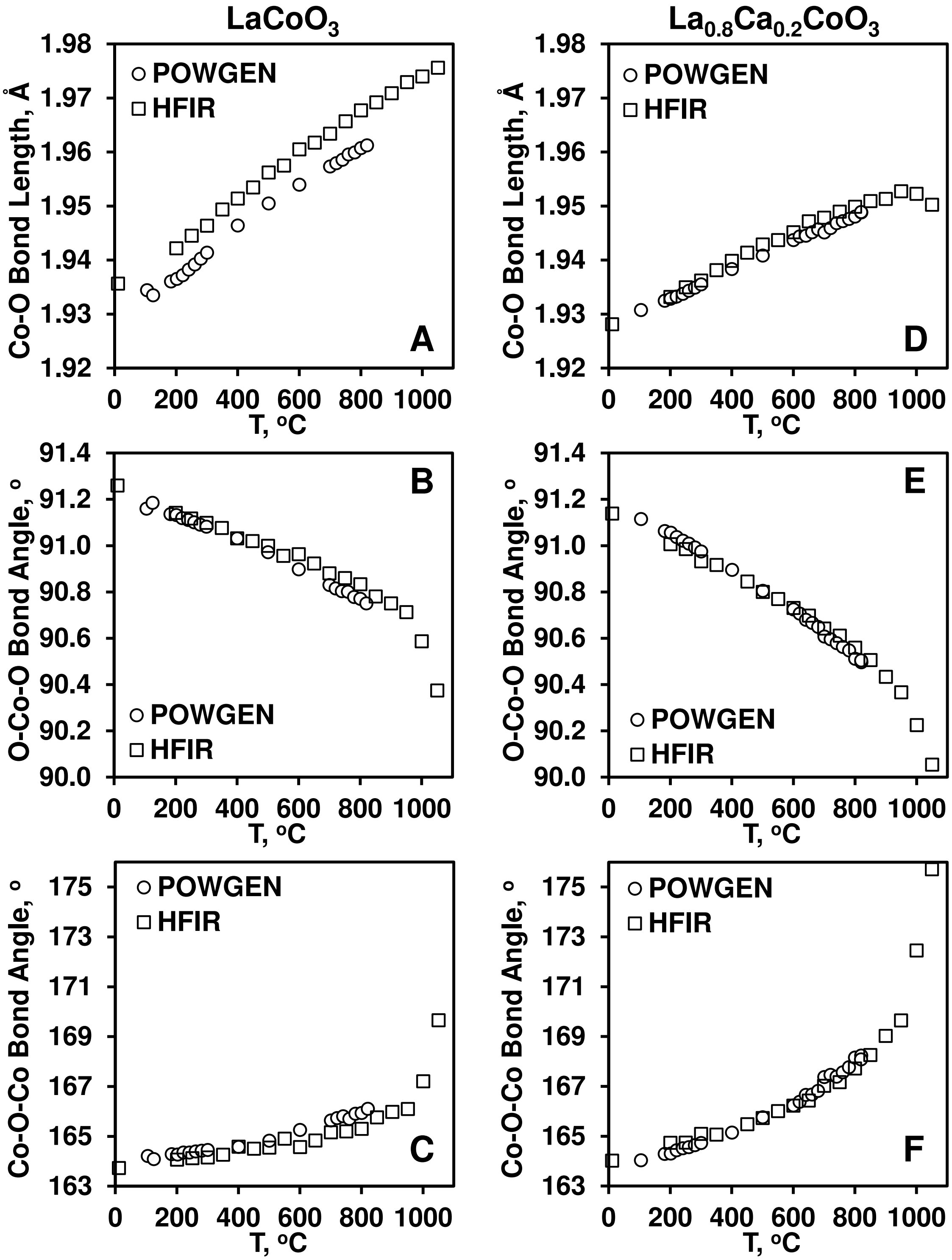

Figure 58. (A, B, C) Change in Co-O bond length, O-Co-O bond angle and Co-O-Co bond angle during heating and cooling of LaCoO$_3$ from the data collected via neutron diffraction at POWGEN and HFIR. (D, E, F) Change in Co-O bond length, O-Co-O bond angle and Co-O-Co bond angle during heating and cooling of La$_{0.8}$Ca$_{0.2}$CoO$_3$ from the data collected via XRD at HTML, neutron diffraction at POWGEN and HFIR.

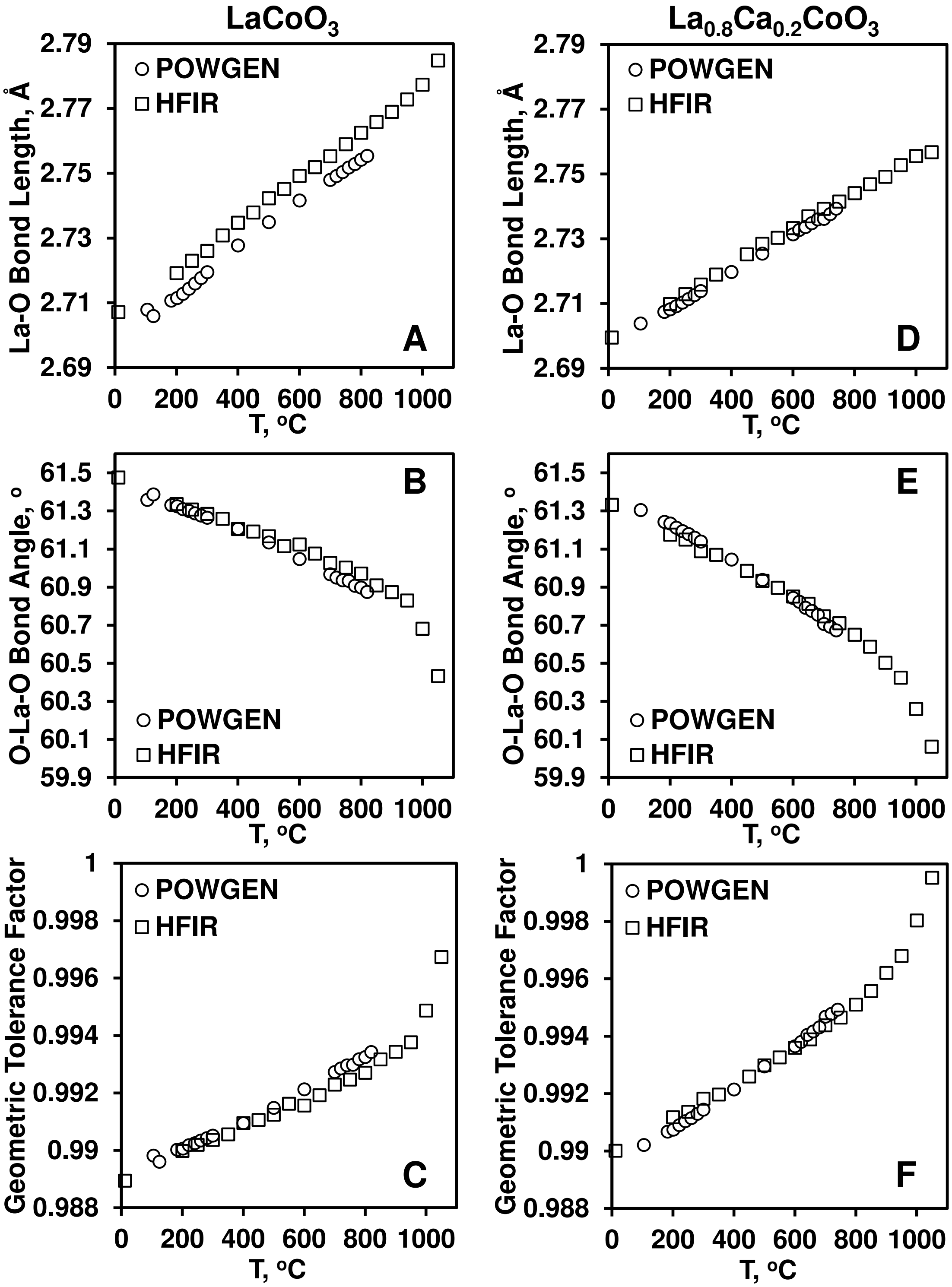

Figure 59. (A, B, C) Change in La-O bond length, O-La-O bond angle and the Geometric tolerance factor during heating and cooling of LaCoO$_3$ from the data collected neutron diffraction at POWGEN and HFIR. (D, E, F) Change in La-O bond length, O-La-O bond angle and the Geometric tolerance factor during heating and cooling of La$_{0.8}$Ca$_{0.2}$CoO$_3$ from the data collected via XRD at HTML, neutron diffraction at POWGEN and HFIR.

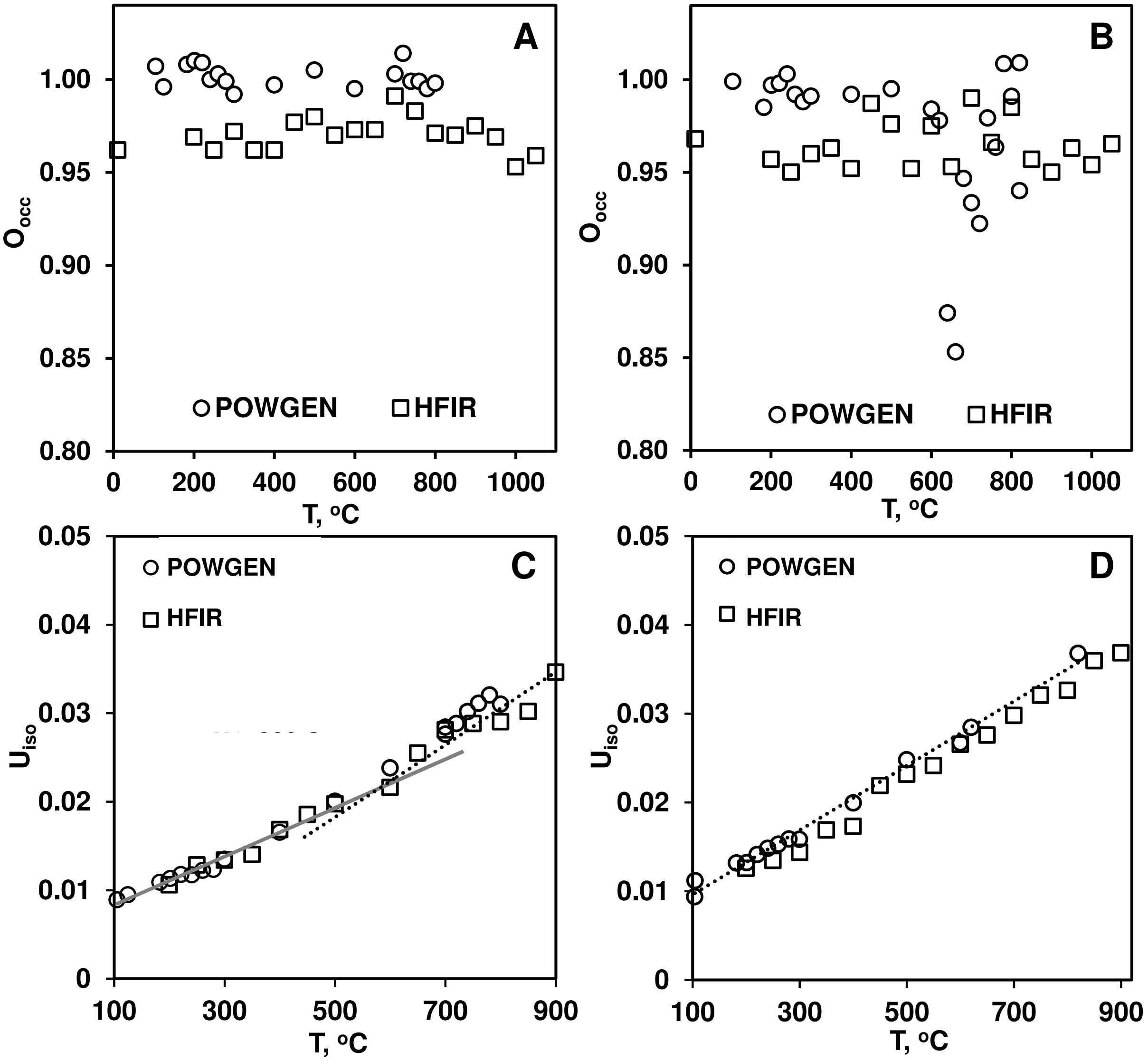

Figure 60. Neutron diffraction data from POWGEN and HFIR. (A, B) shows the change in the oxygen occupancy in the unit cell during heating of $LaCoO_3$ and $La_{0.8}Ca_{0.2}CoO_3$ respectively. (C, D) shows the change in the atomic displacement parameter (Uiso) for the oxygen atom during heating of $LaCoO_3$ and $La_{0.8}Ca_{0.2}CoO_3$ respectively. The slope of the trend line for $LaCoO_3$ up to 500°C is $3x10^{-5}$ and then changes to $4x10^{-5}$ from 600°C to 900°C (C). The slope of the trend line for $La_{0.8}Ca_{0.2}CoO_3$ remains at $4x10^{-5}$ up to 900°C (D).

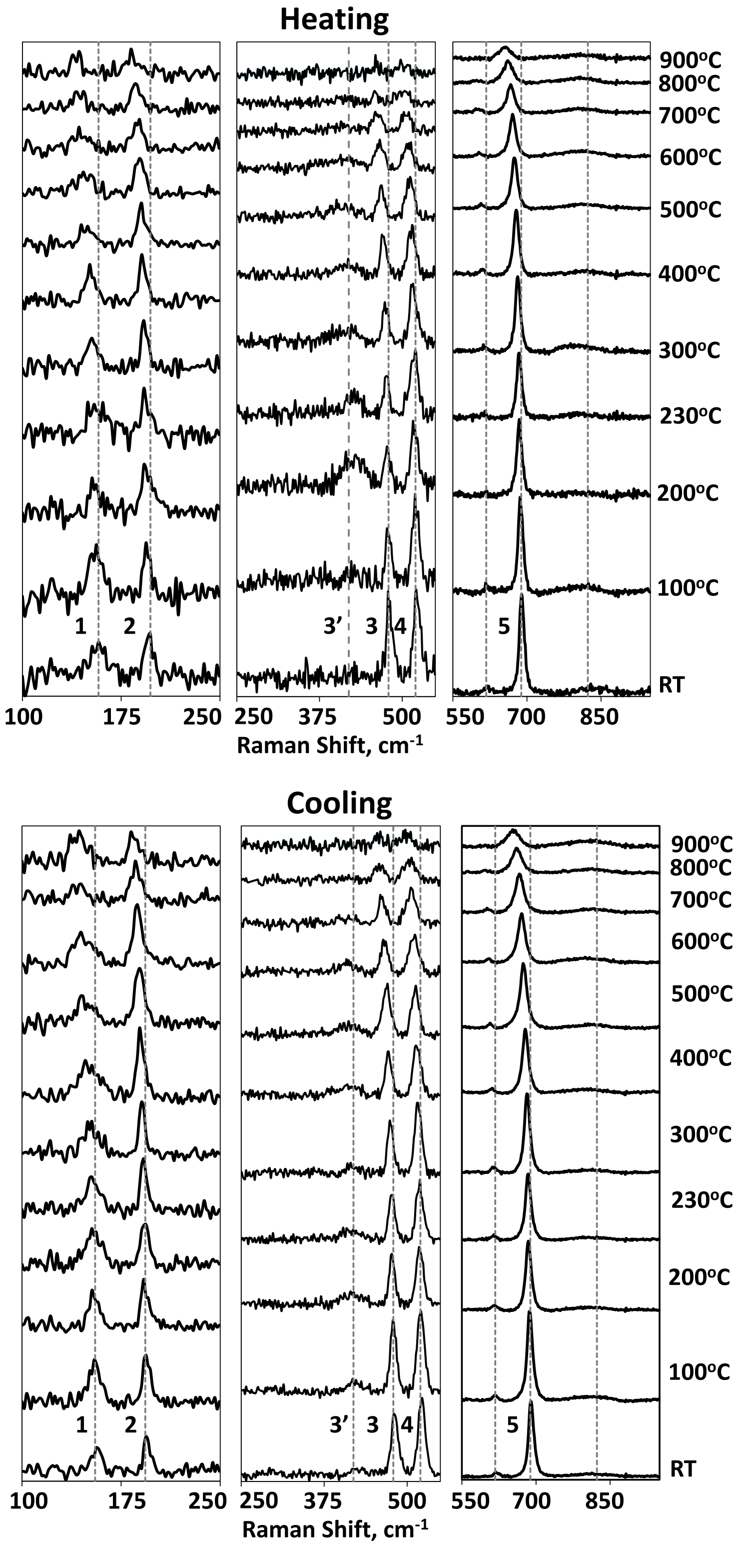

Figure 61. Raman spectra collected for $LaCoO_3$ as it is heated from room temperature to 900°C and then cooled back to room temperature. 1 – 160 cm^{-1}, 2 – 185 cm^{-1}, 3’ – 400 cm^{-1}, 3 – 450 cm^{-1}, 4 – 550 cm^{-1}, 5 – 700 cm^{-1}.

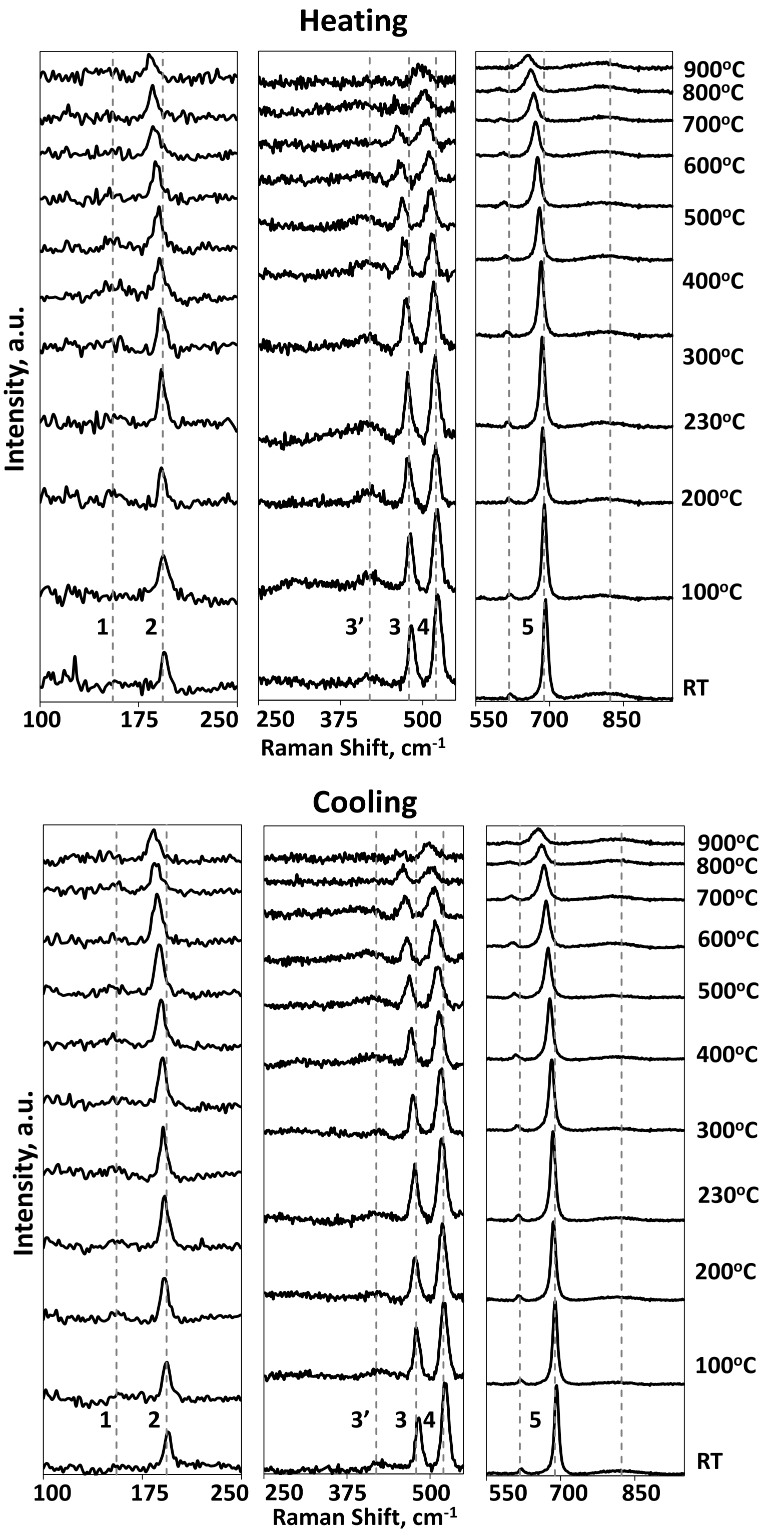

Figure 62. Raman spectra collected for $La_{0.8}Ca_{0.2}CoO_3$ as it is heated from room temperature to 900°C and then cooled back to room temperature. 1 – 160 cm^{-1}, 2 – 185 cm^{-1}, 3 – 400 cm^{-1}, 4 – 450 cm^{-1}, 5 – 550 cm^{-1}, 6 – 700 cm^{-1}.

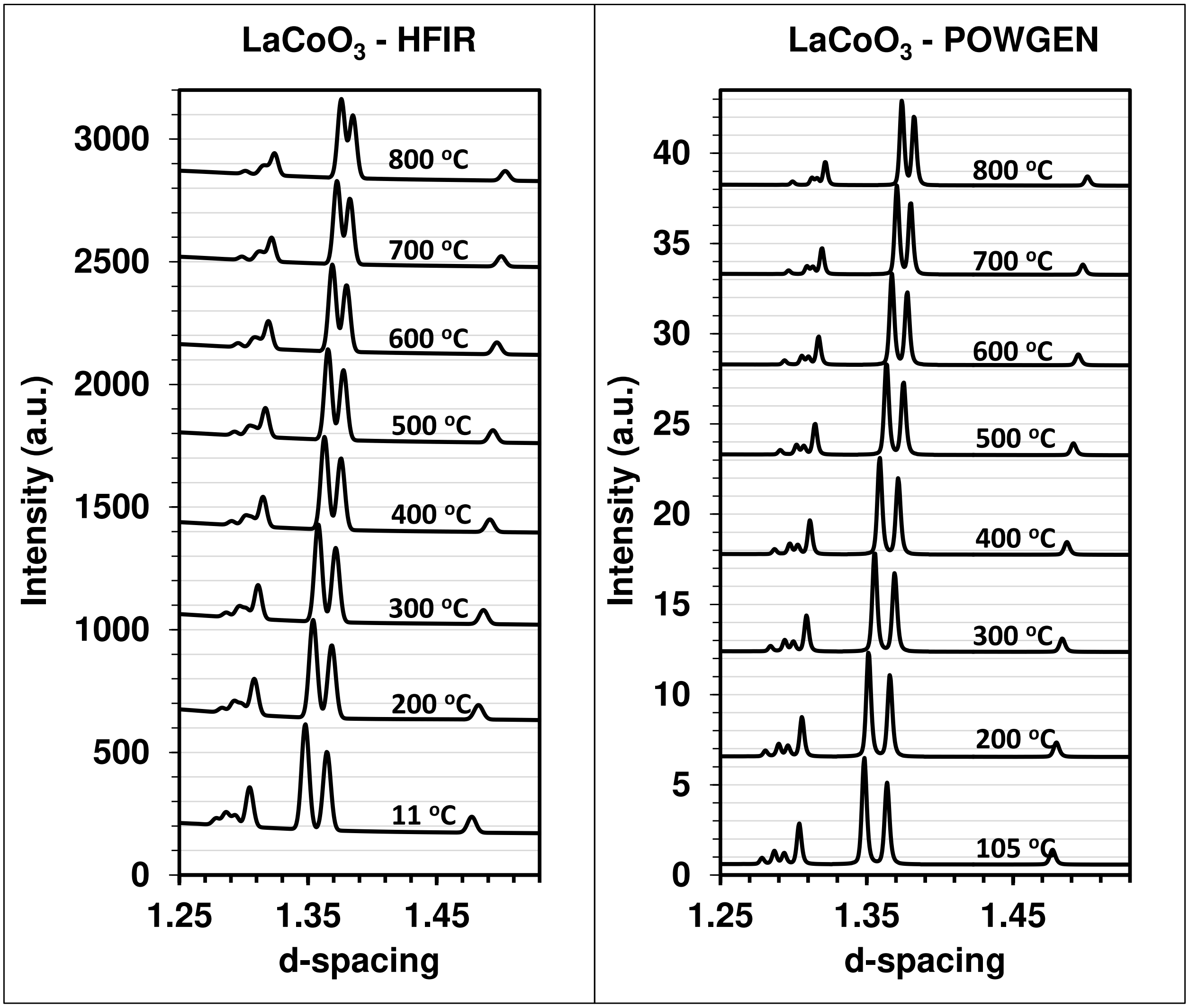

Figure 63. Neutron diffraction pattern of LaCoO$_3$ during heating collected at HB-2A instrument at HFIR, and at POWGEN instrument at SNS, at Oak Ridge National Laboratory.

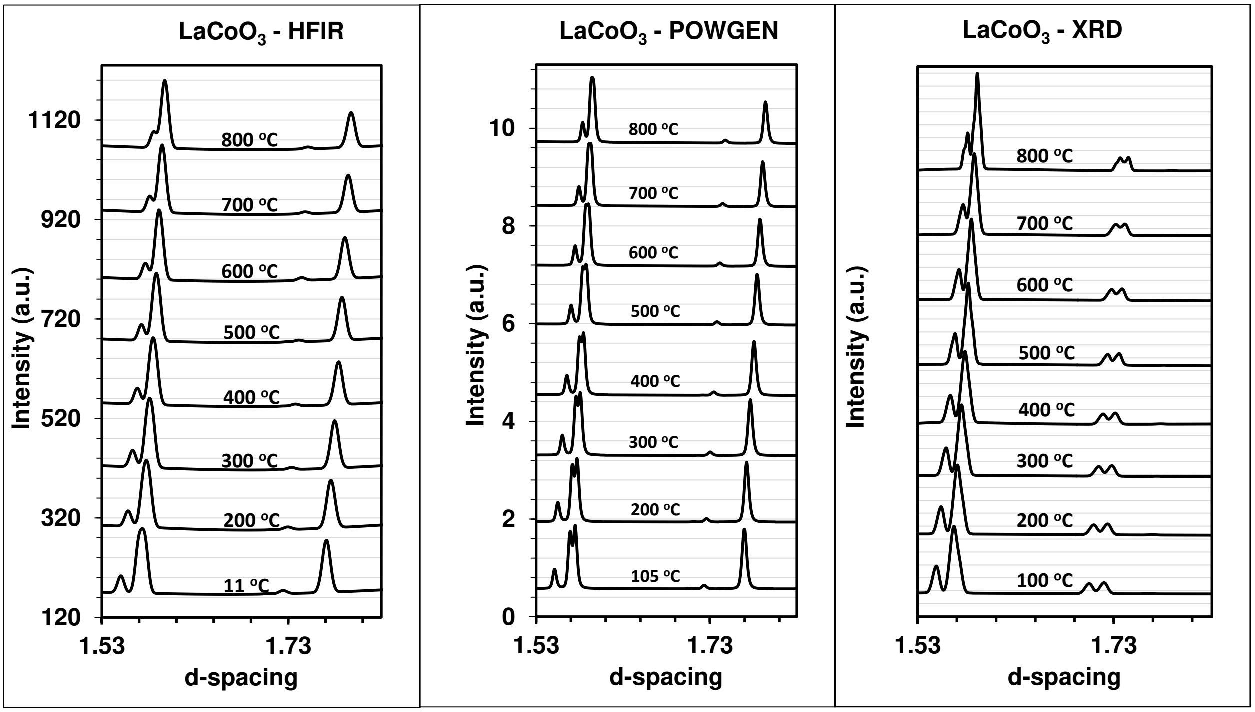

Figure 64. Diffraction pattern of LaCoO$_3$ during heating collected at HB-2A instrument at HFIR, and at POWGEN instrument at SNS, and using XRD, at Oak Ridge National Laboratory.

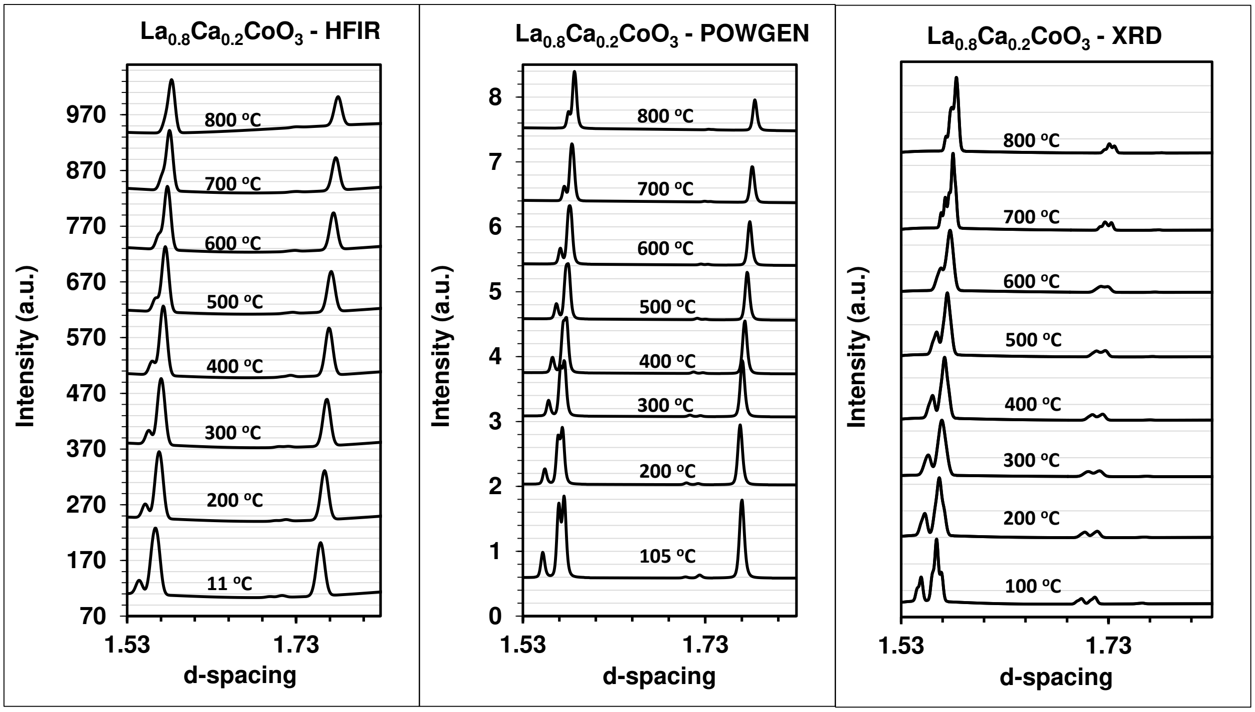

Figure 65. Diffraction pattern of $LaCoO_3$ during heating collected at HB-2A instrument at HFIR, and at POWGEN instrument at SNS, and using XRD, at Oak Ridge National Laboratory.

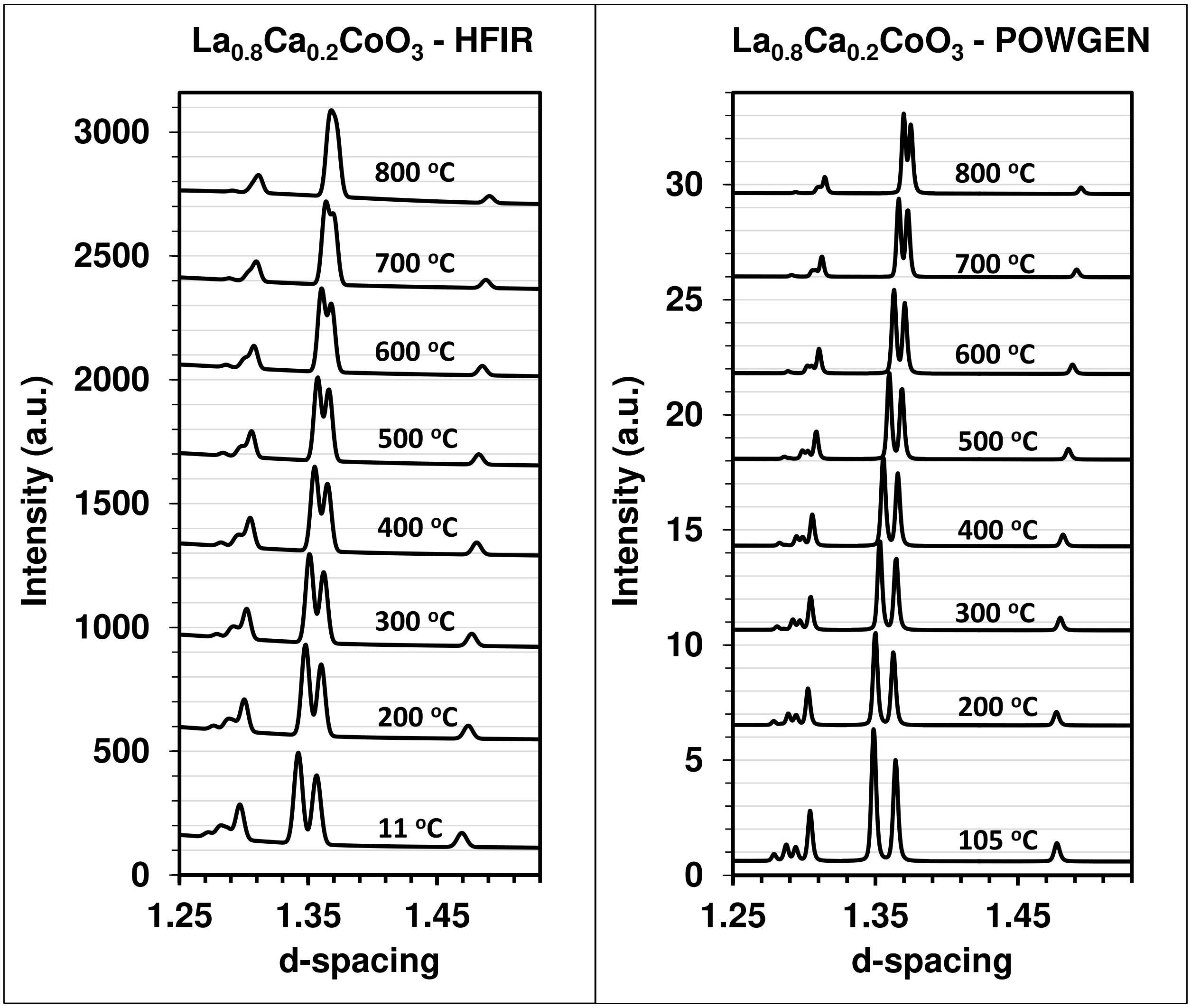

Figure 66. Neutron diffraction pattern of $La_{0.8}Ca_{0.2}CoO_3$ during heating collected at HB-2A instrument at HFIR, and at POWGEN instrument at SNS, at Oak Ridge National Laboratory.

CHAPTER 4: FUEL CELL EDUCATIONAL SOFTWARE

The majority of the content of this chapter is published papers co-authored by the author [180, 181].

The purpose of this portion of the dissertation is to show the development, testing, and evaluation of a software package that is to be used as an augmented/supplementary learning tool in undergraduate fuel cell courses. The emphasis of this tool is the system level thinking of fuel cells and the interconnection among different levels of fuel cell knowledge. The targeted users mainly include undergraduate students in the majors of materials, mechanical, and aerospace engineering.

The effect of the software in enhancing students' learning is also evaluated. Quasi-experimental research is designed to evaluate the effectiveness of the developed software modules. The test group for the current study included around 145 senior undergraduate students in a senior design course.

The methodology used in developing the software package will first be covered. Then several examples in the software modules will be illustrated. After that, the results from the evaluation of the tool in a senior undergraduate student group will be discussed; followed by conclusion and future work.

4.1. Methodology of Software Development

The software was designed with deliberate consideration and a trial-and-error method to find the best way to present the educational material to maximize retention of the material. The main goals of the software are that it has to be easy to use, be highly interactive, gives the student the freedom to learn in their own style, and serves as a supplemental learning tool for fuel cell courses.

The software is designed using Adobe Flash Professional, Adobe Premiere Professional and Microsoft PowerPoint 2013. The software can be accessed and used by students on computers with a standard operating system, a web browser, and an internet connection. The minimal hardware and software requirements make it easy for students to use the software. The instructor could give the students the option to open the software and follow along in the classroom or they could just have the students go over the software outside the classroom.

The software is divided into five modules, each module has sub-modules and the sub-modules contain “slides” with animations or videos. The five modules are: (i) introduction, (ii) applications, (iii) fuel cell systems, (iv) cell level, and (v) fuel cell science. There are two important standpoints in the development of this software: (a) contents, and (b) interconnectedness among software modules. First, the educational content is presented in the form of text, video, and animations with audio. All the material contents are verified by the instructor of the fuel cell courses. Not only is it important to choose the right kind of material, but also the design, sequence, and flow of the animations or videos are planned out; as well as the continuity between animations/videos is taken into consideration. At the same time, the animations/videos are made to keep student's attention and be highly interactive.

Second, the interconnectedness is the unique feature of this software. The five main modules are all interconnected. What is more is that the sub-modules and different slides are interconnected as well. The plan of the interconnections is demonstrated in Figure 67. As shown in Figure 67, the modules and sub-modules are connected through hyperlinks. Clickable buttons are used to establish the interconnections. For example, students most interested in applications can go straight to applications and from there they can go on to learn about fuel cell science, fuel cell systems, or cell level. Or they could start with the fundamental fuel cell science, then go on to learn the working of a fuel cell stack/system and finally the applications. This gives students the freedom to learn and adapt themselves to the material in a way they feel comfortable. This could result in higher retention of the educational content as it reinforces what the students have already learned in class, improve their performance, and can maximize retention of students in the class.

4.2. Module Examples

Here five examples are shown of the five software modules. Each example is explained with the use of figures.

4.2.1 Example 1:

An example of one of the animations in the Introduction module is demonstrated using Figure 68. The animation gives an introduction to the losses in fuel cells. The sequence of the animations is shown in Figure 68 (a) through (f). It starts with the interface of the "Introduction" module in (a). When the button "Losses in Fuel Cells" is clicked, the animation begins as seen in (b). It shows that in the ideal scenario one would want a 100% of the chemical energy of the fuel could be converted to electrical energy, but that's not the case based on the laws of thermodynamics [18, 182]. Figure 68 (c) shows a man trying to obtain as much work from a fuel cell as possible; and in (d) the man has succeeded in extracting the maximum work from a fuel cell. The thermodynamic equations of maximum theoretical work output from a fuel cell are shown. The thermodynamic or reversible voltage for a hydrogen-oxygen fuel cell is 1.23 V and is presented as the upper limit of the voltage achievable, and also points to the fact that there always are other losses to consider [18]. Finally Figure 68 (f) shows the current-voltage plot with the regions of different losses in a fuel cell.

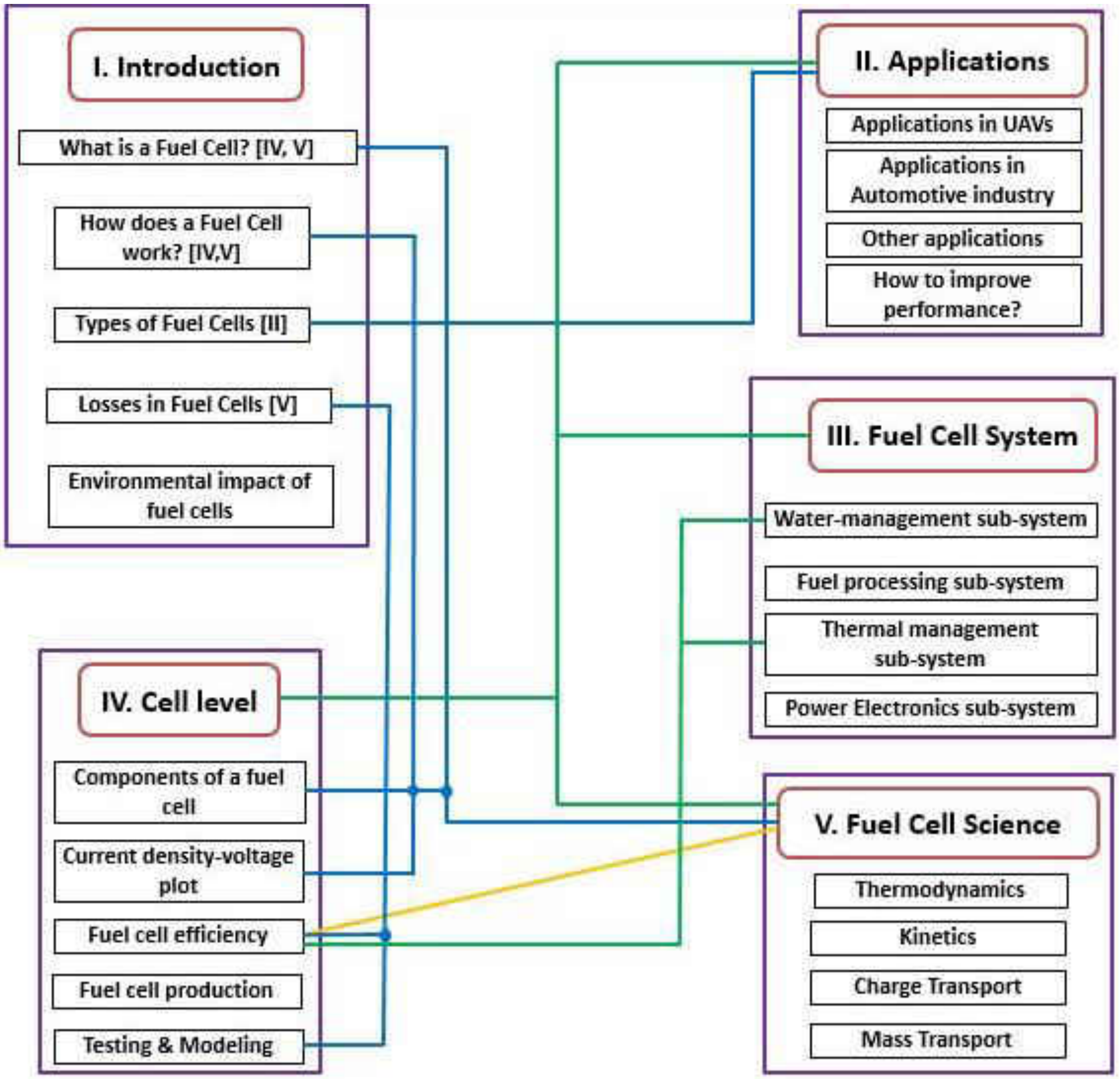

Figure 67. The interconnections among the five main modules of the software.

From here if the student wants to go deeper into the understanding of the science behind the three different types of losses, the student could click on any of the three colored regions in the current-voltage plot, which will take them to the Fuel Cell Science module where the concept of Reaction Kinetics will help explain activation losses [18, 183]. The Charge Transport sub-module will explain Ohmic losses and the Mass Transport sub-module will make the concept of concentration losses [18, 183] clear.

4.2.2. Example 2:

Figure 69 (a) shows the menu of the Fuel Cell Applications module. The applications of fuel cell in UAVs and automotive industry and other applications such as stationary power generation are discussed in this module. Part (b) shows the menu of the sub-module “Applications in UAVs”; this is followed by a sequence of animations. An animation of the three most suitable types of fuel cells that could be used in UAVs can be seen in (c). As seen in (d) Solid Oxide Fuel Cell is not feasible due to the challenge of the high operating temperature of operations of fuel cells that operate way above the room temperature [184]. This will add to the weight of the UAV that increases the overall cost. Use of Alkaline Fuel Cells is also not very favorable due to their operating temperature as shown in (d). Part (e) explains that Polymer Electrolyte Membrane Fuel Cells (PEMFC) are most suitable due to their operating temperature range and other factors [185]. Finally a screenshot of the video of the flight of a UAV designed by senior design students in the Department of Mechanical and Aerospace Engineering at the University of Central Florida is shown in (f). This UAV employed PEMFC as the energy conversion device with a hydrogen tank as the fuel source. Student could click on any of the type of fuel cell, which will take them to the explanation of how each type of fuel cell works under the Introduction module.

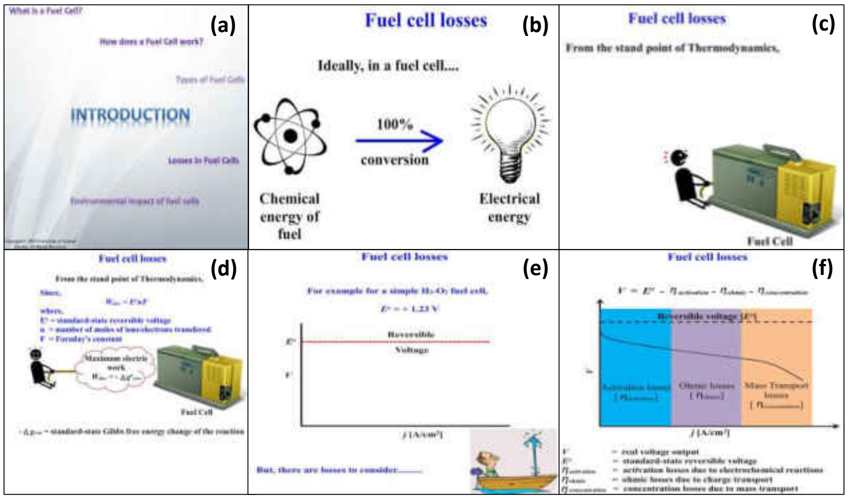

Figure 68. Example of an animation and the interconnections shown in the Introduction module. Part (a) shows the interface of the module; and parts (b) – (f) screen shots of the "Fuel Cell Losses" animation.

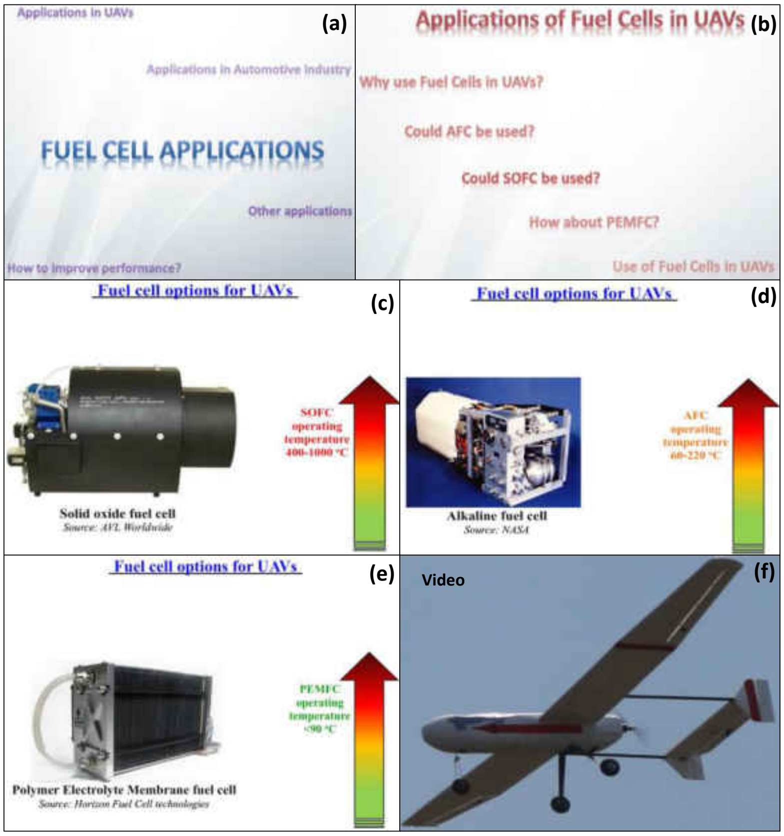

Figure 69. (a) the menu of the Fuel Cell Applications module; (b) the menu of the sub-module Applications in UAVs; (c) animation that presents the three types of fuel cells, here Solid Oxide Fuel Cell (SOFC); (d) Alkaline Fuel Cells; (e) Polymer Electrolyte Membrane Fuel Cells (PEMFC); and(f) video showing the flight of a UAV powered by PEMFC

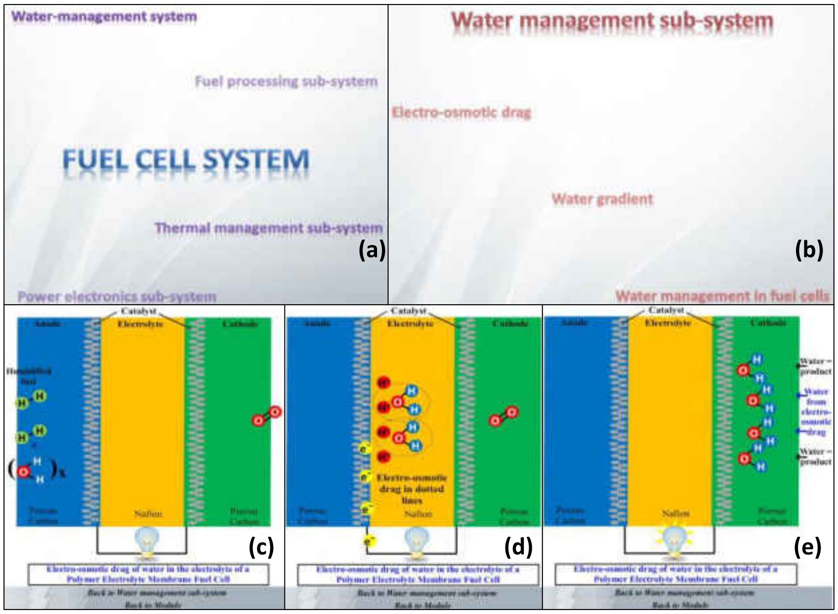

Figure 70. One example animation in the Fuel Cell System module. Part (a): the interface of the module; and part (b): the menu of the "Water management system" sub-module. Screenshots of the "Electro-osmotic drag" animation are shown in parts (c) – (f).

4.2.3. Example 3:

The Fuel Cell System module is discussed in Figure 70. Part (a) shows the menu of the module. The screen shot in (b) is the sub-menu that appears when the "Water-management system" is clicked. Polymer Electrolyte Membrane Fuel Cells (PEMFCs) operate below 100ºC and have the issue of water flooding since the water in the cell will remain in the liquid form. The two contributing factors of this issue is electro-osmotic drag and back diffusion [18]. Parts (c), (d) and (f) show the three progressive steps in the animation that explains the concept of electro-osmotic drag in PEMFCs. This sub-module is connected with the sub-module called Efficiency & How to Improve It under the Cell-Level module. Water flooding is a serious issue and brings down the overall efficiency of the fuel cell [186].

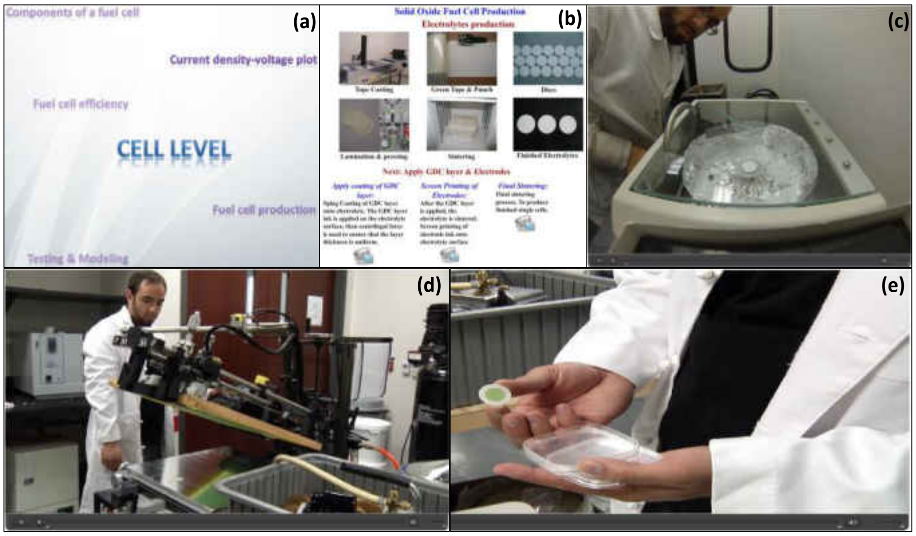

Figure 71. The Cell Level module is explained here. The main menu of the module is displayed in (a); followed by the animation that appears when "Fuel cell production" is clicked; and (c) – (e) are screenshots of three different videos.

4.2.4. Example 4:

The Cell Level module explains various aspects like the components, production, testing, modeling, and study on efficiency of individual fuel cells. In Figure 71 (a) the interface of the Cell Level module is seen. When the "Fuel cell production" button is clicked an animation pops up as displayed in (b) that explains the steps involved in producing electrolytes for solid oxide fuel cells.

These videos are taken at the Ceramics for Energy Applications lab at the University of Central Florida. Part (c) has a screen shot of the video that shows the spin coating of Gadolinia Doped Ceria layer over the surface of the fuel cell electrolyte. Part (d) is a snap shot of the video showing the screen printing of anode and cathode inks over either side of the electrolyte. The final sintering process of the fuel cell is described in the video in part (e). This sub-module is connected to the other sub-module called "Components of a fuel cell" within the same module.

4.2.5. Example 5:

Figure 72 describes one of the animations in the Fuel Cell Science modules starting with the menu of the module in part (a). Part (b) similarly shows the sub-menu that opens up when the “Charge Transport” item is clicked. Animation explaining the concept of Ohmic resistance in fuel cells is seen in part (c) [18, 183]. Part (d) describes the additive nature of resistance in fuel cell components, and part (e) demonstrates the effect of Ohmic losses using the voltage plot across the cross section of the fuel cell. Finally part (f) clarifies the effect of varying magnitudes of Ohmic losses using the current-voltage plot. This sub-module is linked with the sub-module under Cell Level which goes over the concept of current-voltage or power-voltage plots and how to interpret them.

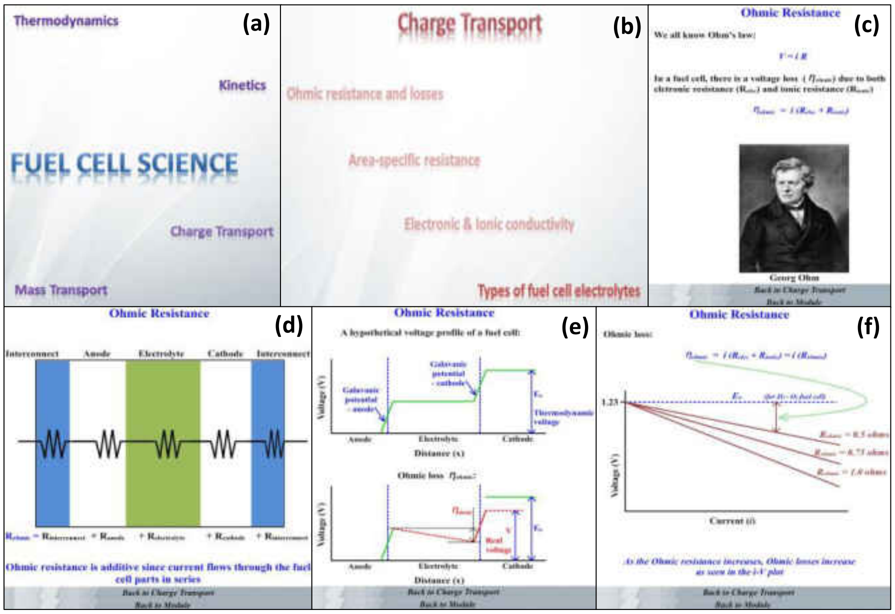

We all know Ohm's law:

$V = i\,R$

In a fuel cell, there is a voltage loss (η_{ohmic}) due to both eletronic resistance (R_{elec}) and ionic resistance (R_{ionic})

$\eta_{ohmic} = i\,(R_{elec} + R_{ionic})$

$R_{ohmic} = R_{interconnect} + R_{anode} + R_{electrolyte} + R_{cathode} + R_{interconnect}$

Ohmic resistance is additive since current flows through the fuel cell parts in series

A hypothetical voltage profile of a fuel cell:

Ohmic loss η_{ohmic}:

Ohmic loss:

$\eta_{ohmic} = i\,(R_{elec} + R_{ionic}) = i\,(R_{ohmic})$

$R_{ohmic} = 0.5$ ohms

$R_{ohmic} = 0.75$ ohms

$R_{ohmic} = 1.0$ ohms

As the Ohmic resistance increases, Ohmic losses increase as seen in the i-V plot

Figure 72. Interface and screenshots of one animation in the Fuel Cell Science module

4.3. Evaluation/Assessment Method

Pre- and post- quantitative data analyses are used to evaluate the effectiveness of the interconnected software modules for increasing engineering students’ learning outcomes and motivations in fuel cell courses.

A random clustered sample of 145 senior college students majoring in Mechanical and Aerospace Engineering from a large university in the south-east of the United States is used. IRB approval at the authors' university was obtained in the Fall of 2014. The *Student Learning Motivation* (SLM) survey [187] based on ARCS [188] model was used to collect student course learning motivation data. SLM has been reported as a reliable instrument for collecting students' course motivation data [187]. The Cronbach alpha value is 0.91 for the current data. The researchers created a *Fuel Cell Knowledge Test* which was used to collect student learning outcome data before and after the software intervention period.

4.3.1. Data Collection Procedure:

Paper-based test and survey were given to the students in a normal classroom setting. Before the class, the researchers distributed the test papers and questionnaires to the students in one large classroom along with the consent form approved by IRB as the cover page of the survey package. One of the researchers read the consent form to the students and made students aware that they were invited to participant the research on a volunteer basis. Students were asked to complete the *Student Learning Motivation* survey and the *Fuel Cell Knowledge Test* as the pretests before class. Then one of the researchers taught the entire class with the software modules as the intervention for 20 minutes. After the intervention, students were asked to complete the *Student Learning Motivation* survey and the *Fuel Cell Knowledge Test* again as the post-tests. Students' demographic data were also collected.

4.3.2. Data Analysis Results*:*

Repeated measure test was used to analyze the pre- and post-test data for comparing test differences in their motivation scores and knowledge test scores between pre-test and post-test. The analysis results showed that after the software treatment, students' motivation was significantly improved with $F(1) = 5.44$ ($p = .02 < .05$) (See Table 10), and the mean of post-test motivation score ($M = 69.10$; $SD = 14.13$) was 2.09 points higher than the mean of pre-test score ($M = 67.01$, $SD = 13.01$). The analysis also revealed that the learning outcomes of students were significantly increased with $F(1) = 20.59$ ($p < .001$) (See Table 11) while controlling for the motivation of students. The mean of students' post knowledge test score ($M = 22.08$, $SD = 5.07$) was 14.47 points higher than the mean of pre-test score ($M = 7.67$, $SD = 4.48$).

To summarize this chapter, a recently developed software tool is discussed, which can be used as a secondary learning tool for students who are interested in fuel cell and hydrogen related technologies. The technical contents are represented using videos, figures, animations, and texts, and all the modules and sub-models in this tool are interconnected. Up to now, a total of five modules have been developed with system level thinking, and some pedagogical effects have been assessed in one senior undergraduate class. It is shown that both students' motivation and learning outcome are significantly improved.

Table 10. Motivation Tests of Within-Subjects Effects

Source		Type III Sum of Squares	*df*	Mean Square	*F*	*p*
Motivation	Sphericity Assumed	266.496	1	266.496	5.436	.021
	Greenhouse-Geisser	266.496	1	266.496	5.436	.021
	Huynh-Feldt	266.496	1	266.496	5.436	.021
	Lower-bound	266.496	1	266.496	5.436	.021
Error(Motivation)	Sphericity Assumed	5932.004	121	49.025		
	Greenhouse-Geisser	5932.004	121	49.025		
	Huynh-Feldt	5932.004	121	49.025		
	Lower-bound	5932.004	121	49.025		

Table 11. Knowledge Tests of Within-Subjects Effects

Source		Type III Sum of Squares	*df*	Mean Square	*F*	*p*
Test	Sphericity Assumed	232.161	1	232.161	20.586	<.001
	Greenhouse-Geisser	232.161	1	232.161	20.586	<.001
	Huynh-Feldt	232.161	1	232.161	20.586	<.001
	Lower-bound	232.161	1	232.161	20.586	<.001
test * CMS_pre_T	Sphericity Assumed	55.540	1	55.540	4.925	.028
	Greenhouse-Geisser	55.540	1	55.540	4.925	.028
	Huynh-Feldt	55.540	1	55.540	4.925	.028
	Lower-bound	55.540	1	55.540	4.925	.028
Error(test)	Sphericity Assumed	1477.400	131	11.278		
	Greenhouse-Geisser	1477.400	131	11.278		
	Huynh-Feldt	1477.400	131	11.278		
	Lower-bound	1477.400	131	11.278		

CHAPTER 5: CONCLUSION

The purpose of this dissertation was to present a multi-scale approach to the study of solid oxide fuel cells. This could be categorized broadly into three sections. Chapter 2 talked about the mechanical testing of layered YSZ and SCSZ electrolytes using the standard ring-on-ring testing, in order to obtain the biaxial flexure strength of these electrolytes. It was shown that the analytical methodology failed to predict the non-linear load and stress behavior in the specimen. The developed finite element model was not only successful with predicting the non-linear load and stress behavior in the specimen, but was also used to determine the biaxial flexure strength of the various electrolyte configurations.

Chapter 3 discussed the thermo-mechanical study of $LaCoO_3$ based perovksites that could be used as cathode material. In-situ neutron diffraction was used to study the crystal structure evolution, texture development, and domain switching phenomenon in material as it was subjected to uniaxial compression. In addition, the elastic properties and elastic constants of $LaCoO_3$ were derived. With the use of in-situ neutron diffraction, X-ray diffraction and Raman spectroscopy; the high temperature study of $LaCoO_3$ based perovskites were carried out to find the correlation between structural and mechanical behavior.

Finally, the design, development and evaluation of an interactive and interconnected educational tool to teach undergraduate students about fuel cells was presented.

LIST OF REFERENCES

[1] I. E. Agency, "World Energy Outlook 2014," November 12, 2014 2014.

[2] T. Elmer, M. Worall, S. Wu, and S. B. Riffat, "Fuel cell technology for domestic built environment applications: State of-the-art review," *Renewable and Sustainable Energy Reviews,* vol. 42, pp. 913-931, 2015.

[3] U. S. o. America, "U.S. Cover Note INDC and Accompanying Information," ed, 2015.

[4] L. Blum, U. Packbier, I. C. Vinke, and L. G. J. de Haart, "Long-Term Testing of SOFC Stacks at Forschungszentrum Jülich▲," *Fuel Cells,* 2012.

[5] K. Huang and J. B. Goodenough, *Solid oxide fuel cell technology: principles, performance and operations*: CRC Press, 2009.

[6] F. C. Today, "The fuel cell industry review," *Fuel Cell Today,* 2013.

[7] E. Baur and H. Preis, "Über Brennstoff‐Ketten mit Festleitern," *Zeitschrift für Elektrochemie und angewandte physikalische Chemie,* vol. 43, pp. 727-732, 1937.

[8] D. J. Brett, A. Atkinson, N. P. Brandon, and S. J. Skinner, "Intermediate temperature solid oxide fuel cells," *Chemical Society Reviews,* vol. 37, pp. 1568-1578, 2008.

[9] A. B. Stambouli and E. Traversa, "Solid oxide fuel cells (SOFCs): a review of an environmentally clean and efficient source of energy," *Renewable and Sustainable Energy Reviews,* vol. 6, pp. 433-455, 2002.

[10] S. Badwal, S. Giddey, A. Kulkarni, and C. Munnings, "Review of progress in high temperature solid oxide fuel cells," *J. Aust. Cer. Soc,* vol. 50, pp. 23-37, 2014.

[11] N. Mahato, A. Banerjee, A. Gupta, S. Omar, and K. Balani, "Progress in material selection for solid oxide fuel cell technology: A review," *Progress in Materials Science,* vol. 72, pp. 141-337, 2015.

[12] M. C. Williams, J. P. Strakey, and S. C. Singhal, "U.S. distributed generation fuel cell program," *Journal of Power Sources,* vol. 131, pp. 79-85, 5/14/ 2004.

[13] S. Singhal, "Science and technology of solid-oxide fuel cells," *MRS bulletin,* vol. 25, pp. 16-21, 2000.

[14] B. Haberman and A. Marquis, "A Numerical Investigation Into the Interaction Between Current Flow and Fuel Consumption in a Segmented-in-Series Tubular SOFC," *Journal of fuel cell science and technology,* vol. 6, 2009.

[15] M. Cologna, "Advances in the Production of Planar and Micro-Tubular Solid Oxide Fuel Cells," University of Trento, 2009.

[16] A. Buonomano, F. Calise, M. D. d'Accadia, A. Palombo, and M. Vicidomini, "Hybrid solid oxide fuel cells–gas turbine systems for combined heat and power: A review," *Applied Energy,* vol. 156, pp. 32-85, 2015.

[17] S. Singhal, *High-temperature Solid Oxide Fuel Cells: Fundamentals, Design and Applications: Fundamentals, Design and Applications*: Elsevier Science, 2003.

[18] R. P. O'Hayre, S.-W. Cha, W. Colella, and F. B. Prinz, *Fuel cell fundamentals*: John Wiley & Sons New York, 2006.

[19] W. Winkler and H. Lorenz, "Design studies of mobile applications with SOFC–heat engine modules," *Journal of power sources,* vol. 106, pp. 338-343, 2002.

[20] A. Choudhury, H. Chandra, and A. Arora, "Application of solid oxide fuel cell technology for power generation—A review," *Renewable and Sustainable Energy Reviews,* vol. 20, pp. 430-442, 2013.

[21] Z. Yan, P. Zhao, J. Wang, and Y. Dai, "Thermodynamic analysis of an SOFC–GT–ORC integrated power system with liquefied natural gas as heat sink," *International Journal of Hydrogen Energy,* vol. 38, pp. 3352-3363, 2013.

[22] http://www.bloomenergy.com/.

[23] Y. Zhao, C. Xia, L. Jia, Z. Wang, H. Li, J. Yu*, et al.*, "Recent progress on solid oxide fuel cell: Lowering temperature and utilizing non-hydrogen fuels," *International Journal of Hydrogen Energy,* vol. 38, pp. 16498-16517, 2013.

[24] M. Fellet and W. Rossner, "Ceramics improve operating conditions of solid-oxide fuel cells," *MRS Bulletin,* vol. 40, pp. 214-215, 2015.

[25] J. B. Goodenough, "Ceramic technology: Oxide-ion conductors by design," *Nature,* vol. 404, pp. 821-823, 2000.

[26] S. Badwal, F. Ciacchi, and J. Drennan, "Investigation of the stability of ceria-gadolinia electrolytes in solid oxide fuel cell environments," *Solid State Ionics,* vol. 121, pp. 253-262, 1999.

[27] B. Steele, "Appraisal of Ce 1− y Gd y O 2− y/2 electrolytes for IT-SOFC operation at 500 C," *Solid state ionics,* vol. 129, pp. 95-110, 2000.

[28] Y. Ma, "Ceria-based nanocomposite electrolyte for low-temperature solid oxide fuel cells," KTH, 2009.

[29] B. C. Steele and A. Heinzel, "Materials for fuel-cell technologies," *Nature,* vol. 414, pp. 345-352, 2001.

[30] D. Simwonis, F. Tietz, and D. Stöver, "Nickel coarsening in annealed Ni/8YSZ anode substrates for solid oxide fuel cells," *Solid State Ionics,* vol. 132, pp. 241-251, 2000.

[31] E. D. Wachsman and K. T. Lee, "Lowering the Temperature of Solid Oxide Fuel Cells," *Science,* vol. 334, pp. 935-939, 2011.

[32] S. Jiang, "Advances and Challenges of Intermediate Temperature Solid Oxide Fuel Cells: A Concise Review," *Journal of Electrochemistry,* vol. 18, pp. 479-495, 2012-12-03 2012.

[33] S.-C. Park, J.-J. Lee, S.-H. Lee, J. Moon, and S.-H. Hyun, "Design and Preparation of SOFC Unit Cells Using Scandia-Stabilized Zirconia Electrolyte for Intermediate Temperature Operation," *Journal of fuel cell science and technology,* vol. 8, 2011.

[34] J. B. Goodenough, "Oxide-ion electrolytes," *Annual Review of Materials Research,* vol. 33, pp. 91-128, 2003.

[35] F. Figueiredo and F. Marques, "Electrolytes for solid oxide fuel cells," *Wiley Interdisciplinary Reviews: Energy and Environment,* vol. 2, pp. 52-72, 2013.

[36] K. Kreuer, "Proton-conducting oxides," *Annual Review of Materials Research,* vol. 33, pp. 333-359, 2003.

[37] J. W. Fergus, *Solid oxide fuel cells: materials properties and performance* vol. 1: CRC PressI Llc, 2009.

[38] S. Badwal, "Zirconia-based solid electrolytes: microstructure, stability and ionic conductivity," *Solid State Ionics,* vol. 52, pp. 23-32, 1992.

[39] C. C. Sorrell, J. Nowotny, and S. Sugihara, *Materials for energy conversion devices*: Elsevier, 2005.

[40] M. Nasrallah and D. Douglass, "Ionic and electronic conductivity in Y 2 O 3 ‐ doped monoclinic ZrO2," *Journal of The Electrochemical Society,* vol. 121, pp. 255-262, 1974.

[41] G. Katz, "X ‐ Ray Diffraction Powder Pattern of Metastable Cubic ZrO2," *Journal of the American Ceramic Society,* vol. 54, pp. 531-531, 1971.

[42] J. Boivin and G. Mairesse, "Recent material developments in fast oxide ion conductors," *Chemistry of materials,* vol. 10, pp. 2870-2888, 1998.

[43] J. Fergus, R. Hui, X. Li, D. P. Wilkinson, and J. Zhang, *Solid oxide fuel cells: materials properties and performance*: CRC press, 2008.

[44] J. W. Fergus, "Electrolytes for solid oxide fuel cells," *Journal of Power Sources,* vol. 162, pp. 30-40, 2006.

[45] A. Nakamura and J. B. Wagner, "Defect structure, ionic conductivity, and diffusion in yttria stabilized zirconia and related oxide electrolytes with fluorite structure," *Journal of the Electrochemical Society,* vol. 133, pp. 1542-1548, 1986.

[46] U. o. Cambridge. (2004-2015). *Solid Oxide Fuel Cells - Electrolyte*. Available: http://www.doitpoms.ac.uk/tlplib/fuel-cells/sofc_electrolyte.php

[47] S. Ostanin, E. Salamatov, A. Craven, D. McComb, and D. Vlachos, "Theory of the phases and atomistic structure of yttria-doped zirconia," *Physical Review B,* vol. 66, p. 132105, 2002.

[48] D. W. Strickler and W. G. Carlson, "Electrical Conductivity in the ZrO2-Rich Region of Several M2O3—ZrO2 Systems," *Journal of the American Ceramic Society,* vol. 48, pp. 286-289, 1965.

[49] Y. Chen, N. Orlovskaya, M. Klimov, X. Huang, D. Cullen, T. Graule*, et al.*, "Layered YSZ/SCSZ/YSZ Electrolytes for Intermediate Temperature SOFC Part I: Design and Manufacturing," *Fuel Cells,* vol. 12, pp. 722-731, 2012.

[50] S. Ho, C. Hillman, F. Lange, and Z. Suo, "Surface cracking in layers under biaxial, residual compressive stress," *Journal of the American Ceramic Society,* vol. 78, pp. 2353-2359, 1995.

[51] P. Hjalmarsson, *Strontium and Nickel Substituted Lanthanum Cobaltite as Cathode in Solid Oxide Fuel Cells: PhD Thesis*: Fuel Cells and Solid State Chemistry Department, Technical University of Denmark, 2008.

[52] D. Button and D. Archer, "Development of La1-x SrxCoO3 air electrodes for solid electrolyte fuel cells," in *Amer Ceram Soc Washington, Meeting May*, 1966.

[53] H.-H. Möbius, "On the history of solid electrolyte fuel cells," *Journal of solid state electrochemistry,* vol. 1, pp. 2-16, 1997.

[54] K. Huang, H. Y. Lee, and J. B. Goodenough, "Sr ‐ and Ni ‐ Doped LaCoO3 and LaFeO3 Perovskites New Cathode Materials for Solid ‐ Oxide Fuel Cells," *Journal of the Electrochemical Society,* vol. 145, pp. 3220-3227, 1998.

[55] K. Huang, M. Feng, J. B. Goodenough, and M. Schmerling, "Characterization of Sr ‐ Doped LaMnO3 and LaCoO3 as Cathode Materials for a Doped LaGaO3 Ceramic Fuel Cell," *Journal of the Electrochemical Society,* vol. 143, pp. 3630-3636, 1996.

[56] W. Zhou, Z. Shao, R. Ran, P. Zeng, H. Gu, W. Jin*, et al.*, "Ba 0.5 Sr 0.5 Co 0.8 Fe 0.2 O 3− δ+ LaCoO 3 composite cathode for Sm 0.2 Ce 0.8 O 1.9-electrolyte based intermediate-temperature solid-oxide fuel cells," *Journal of power sources,* vol. 168, pp. 330-337, 2007.

[57] R. Heikes, R. Miller, and R. Mazelsky, "Magnetic and electrical anomalies in LaCoO 3," *Physica,* vol. 30, pp. 1600-1608, 1964.

[58] C. Naiman, R. Gilmore, B. DiBartolo, A. Linz, and R. Santoro, "Interpretation of the magnetic properties of LaCoO3," *Journal of Applied Physics,* vol. 36, pp. 1044-1045, 1965.

[59] P. Raccah and J. Goodenough, "First-Order Localized-Electron⇆ Collective-Electron Transition in LaCo O 3," *Physical Review,* vol. 155, p. 932, 1967.

[60] V. Křápek, P. Novák, J. Kuneš, D. Novoselov, D. M. Korotin, and V. Anisimov, "Spin state transition and covalent bonding in LaCoO 3," *Physical Review B,* vol. 86, p. 195104, 2012.

[61] Y. Yamada, K. Yano, D. Hong, and S. Fukuzumi, "LaCoO3 acting as an efficient and robust catalyst for photocatalytic water oxidation with persulfate," *Physical Chemistry Chemical Physics,* vol. 14, pp. 5753-5760, 2012.

[62] H. Zhu, P. Zhang, and S. Dai, "Recent Advances of Lanthanum-Based Perovskite Oxides for Catalysis," *ACS Catalysis,* vol. 5, pp. 6370-6385, 2015.

[63] S. Royer, D. Duprez, F. Can, X. Courtois, C. Batiot-Dupeyrat, S. Laassiri*, et al.*, "Perovskites as substitutes of noble metals for heterogeneous catalysis: Dream or reality," *Chemical reviews,* vol. 114, pp. 10292-10368, 2014.

[64] M. Lugovy, V. Slyunyayev, N. Orlovskaya, D. Verbylo, and M. J. Reece, "Room-temperature creep of LaCoO_ {3}-based perovskites: Equilibrium strain under compression," *Physical Review B,* vol. 78, p. 024107, 2008.

[65] N. Orlovskaya, Y. Gogotsi, M. Reece, B. Cheng, and I. Gibson, "Ferroelasticity and hysteresis in LaCoO< sub> 3</sub> based perovskites," *Acta materialia,* vol. 50, pp. 715-723, 2002.

[66] N. Orlovskaya, M. Lugovy, S. Pathak, D. Steinmetz, J. Lloyd, L. Fegely*, et al.*, "Thermal and mechanical properties of LaCoO< sub> 3</sub> and La< sub> 0.8</sub> Ca< sub> 0.2</sub> CoO< sub> 3</sub> perovskites," *Journal of Power Sources,* vol. 182, pp. 230-239, 2008.

[67] A. Aman, Y. Chen, M. Lugovy, N. Orlovskaya, M. J. Reece, D. Ma*, et al.*, "In-situ neutron diffraction of LaCoO3 perovskite under uniaxial compression. I. Crystal structure analysis and texture development," *Journal of Applied Physics,* vol. 116, p. 013503, 2014.

[68] M. Lugovy, A. Aman, Y. Chen, N. Orlovskaya, J. Kuebler, T. Graule*, et al.*, "In-situ neutron diffraction of LaCoO3 perovskite under uniaxial compression. II. Elastic properties," *Journal of Applied Physics,* vol. 116, p. 013504, 2014.

[69] M. Losurdo, A. Sacchetti, P. Capezzuto, G. Bruno, L. Armelao, D. Barreca*, et al.*, "Optical and electrical properties of nanostructured< equation>< font face='verdana'> LaCoO< sub> 3</sub></equation> thin films," *Applied Physics Letters,* vol. 87, pp. 061909-061909-3, 2005.

[70] C. J. Benedict, A. Rao, G. Sanjeev, G. Okram, and P. Babu, "A systematic study on the effect of electron beam irradiation on structural, electrical, thermo-electric power and magnetic property of LaCoO 3," *Journal of Magnetism and Magnetic Materials,* vol. 397, pp. 145-151, 2016.

[71] Q. Wei, T. Zhang, X. P. Wang, and Q. F. Fang, "Size effects on the magnetic properties of LaCoO3 nanoparticles," *The European Physical Journal - Applied Physics,* vol. 57, pp. null-null, 2012.

[72] A. Durand, D. Belanger, T. Hamil, F. Ye, S. Chi, J. Fernandez-Baca*, et al.*, "The unusual magnetism of nanoparticle LaCoO3," *Journal of Physics: Condensed Matter,* vol. 27, p. 176003, 2015.

[73] M. E. Berg, "Magnetic force microscopy studies of magnetic domain structure in $LaCoO_3$ and UMn_2Ge_2," 2014.

[74] K. Kleveland, N. Orlovskaya, T. Grande, A. M. M. Moe, M. A. Einarsrud, K. Breder, *et al.*, "Ferroelastic Behavior of LaCoO3 ‐ Based Ceramics," *Journal of the American Ceramic Society,* vol. 84, pp. 2029-2033, 2001.

[75] U. Balachandran, J. Dusek, P. Maiya, B. Ma, R. Mieville, M. Kleefisch, *et al.*, "Ceramic membrane reactor for converting methane to syngas," *Catalysis Today,* vol. 36, pp. 265-272, 1997.

[76] S. Kim, Y. Yang, R. Christoffersen, and A. Jacobson, "Determination of oxygen permeation kinetics in a ceramic membrane based on the composition SrFeCo< sub> 0.5</sub> O< sub> 3.25− δ</sub>," *Solid state ionics,* vol. 109, pp. 187-196, 1998.

[77] E. Goldberg, A. Nemudry, V. Boldyrev, and R. Schöllhorn, "Model for anomalous transport of oxygen in nonstoichiometric perovskites: 1. General formulation of the problem," *Solid State Ionics,* vol. 110, pp. 223-233, 1998.

[78] M. Pena and J. Fierro, "Chemical structures and performance of perovskite oxides," *Chemical Reviews,* vol. 101, pp. 1981-2018, 2001.

[79] M. S. D. Read, M. Saiful Islam, G. W. Watson, F. King, and F. E. Hancock, "Defect chemistry and surface properties of LaCoO," *Journal of Materials Chemistry,* vol. 10, pp. 2298-2305, 2000.

[80] S. Daungdaw, "PREPARATION OF LaCoO3 PEROVSKITE FOR CO GAS SENSOR," Degree of Master of Science (Chemistry), Chemistry, Graduate School, Kasetsart University, 2009.

[81] P. Hjalmarsson, M. B. Mogensen, and R. Fehrmann, "Strontium and nickel substituted lanthanum cobaltite as cathode in Solid Oxide Fuel Cells," Technical University of DenmarkDanmarks Tekniske Universitet, Department of ChemistryInstitut for Kemi, 2008.

[82] P. Raccah and J. Goodenough, "First-Order Localized-Electron⇆ Collective-Electron Transition in LaCoO_ {3}," *Physical Review,* vol. 155, p. 932, 1967.

[83] Y. Kobayashi, T. Mitsunaga, G. Fujinawa, T. Arii, M. Suetake, K. Asai, *et al.*, "Structural Phase Transition from Rhombohedral to Cubic in LaCoO_ 3," *Journal of the Physical Society of Japan,* vol. 69, pp. 3468-3469, 2000.

[84] H. F. B. Gilbu, and A. Kjekshus, *Acta Chemica Scandinavica,* vol. 48, p. 37, 1994.

[85] K. Aizu, "Possible species of ferromagnetic, ferroelectric, and ferroelastic crystals," *Physical Review B,* vol. 2, p. 754, 1970.

[86] R. J. Harrison, S. A. Redfern, and E. K. Salje, "Dynamical excitation and anelastic relaxation of ferroelastic domain walls in LaAlO_ {3}," *Physical Review B,* vol. 69, p. 144101, 2004.

[87] K. Aizu, "Possible species of ferroelastic crystals and of simultaneously ferroelectric and ferroelastic crystals," *J. Phys. Soc. Japan,* vol. 27, 1969.

[88] E. Salje, "Phase transitions in ferroelastic and co-elastic crystals," *Ferroelectrics,* vol. 104, pp. 111-120, 1990.

[89] F. Greco, A. Nakajo, and Z. Wuillemin, "Thermo-Mechanical Reliability of SOFC Stacks during Combined Long-Term Operation and Thermal Cycling," *ECS Transactions,* vol. 68, pp. 1921-1931, 2015.

[90] N. C. o. S. Legislatures, "Meeting the Energy Challenges of the Future: A Guide for Policymakers," N. C. o. S. Legislatures, Ed., ed, 2010.

[91] U. S. D. o. Energy, "Energy Literacy: Essential Principles and Fundamental Concepts for Energy Education," 2014.

[92] O. o. E. E. R. Energy. *Education homepage*. Available: http://energy.gov/eere/education/education-homepage

[93] CareerOneStop.Org. (2015). *Energy: Renewable Energy Competency Model*. Available: http://www.careeronestop.org/competencymodel/competency-models/renewable-energy.aspx

[94] T. C. Kandpal and L. Broman, "Renewable energy education: A global status review," *Renewable and Sustainable Energy Reviews,* vol. 34, pp. 300-324, 2014.

[95] L. Broman, "On the didactics of renewable energy education—drawing on twenty years experience," *Renewable Energy,* vol. 5, pp. 1398-1405, 1994.

[96] P. Jennings, "New directions in renewable energy education," *Renewable Energy,* vol. 34, pp. 435-439, 2009.

[97] F. S. E. Center. (2015). *Education - Florida Solar Energy Center*. Available: http://www.fsec.ucf.edu/En/education/index.htm

[98] L. Broman and T. C. Kandpal, "PURE–Public Understanding of Renewable Energy," in *Proc. World Renewable Energy Congress WREC-2011 in Linköping, Sweden*, 2011, pp. 8-13.

[99] A. Q. Huang, "Renewable energy system research and education at the NSF FREEDM systems center," in *Power & Energy Society General Meeting, 2009. PES'09. IEEE*, 2009, pp. 1-6.

[100] S. Curtin and J. Gangi, "The Business Case for Fuel Cells 2014: Powering the Bottom Line for Businesses and Communities," 2014.

[101] T. T. Corporation, "Annual Report on World Progress in Hydrogen," June, 2011 2011.

[102] U. S. D. o. Energy, "Fuel Cell Technologies Office January 2014 Newsletter," 2014.

[103] G. Bromaghim, Gibeault, K., Serfass, J., Serfass, P., and Wagner, E., "Hydrogen and Fuel Cells: The U.S. Market Report," March 22, 2010.

[104] B. T. I. Fuel Cells 2000. (2015). Available: http://www.fuelcells.org/ced/career/university.htm

[105] Y. Chen, A. Aman, M. Lugovy, N. Orlovskaya, S. Wang, X. Huang, *et al.*, "Residual stress and biaxial strength in Sc2O3–CeO2–ZrO2/Y2O3–ZrO2 layered electrolytes," *Fuel Cells,* vol. 13, pp. 1068-1075, 2013.

[106] N. Orlovskaya, S. Lukich, G. Subhash, T. Graule, and J. Kuebler, "Mechanical properties of 10mol% Sc< sub> 2</sub> O< sub> 3</sub>–1mol% CeO< sub> 2</sub>–89mol% ZrO< sub> 2</sub> ceramics," *Journal of Power Sources,* vol. 195, pp. 2774-2781, 2010.

[107] S. Giraud and J. Canel, "Young's modulus of some SOFCs materials as a function of temperature," *Journal of the European Ceramic Society,* vol. 28, pp. 77-83, 2008.

[108] Y. Chen, "Scandia and ceria stabilized zirconia based electrolytes and anodes for intermediate temperature solid oxide fuel cells: manufacturing and properties," Doctor of Philosophy Dissertation, Department of Mechanical and Aersospace Engineering, University of Central Florida, Orlando, Florida, USA, 2013.

[109] A. Aman, Russell Gentile, Yan Chen, Yunjun Xu, Xinyu Huang, and Nina Orlovskaya, "Numerical Simulation of Electrolyte-Supported Planar Button Solid Oxide Fuel Cells," presented at the COMSOL Boston 2012 conference, Boston, MA, USA, 2012.

[110] C. M. a. version, "Structural Mechanics module user's guide," 2012.

[111] A. F. Bower, *Applied mechanics of solids*: CRC press, 2011.

[112] A. s. C. 09, "Standard Test Method for Monotonic Equibiaxial Flexural Strength of Advanced Ceramics at Ambient Temperature," ed.

[113] T. E. M.E. Manley, C. Vaucamps, D. Gailus, *Ceram. Eng. Sci. Proc.,* vol. 20, 1999.

[114] L. P. J.A. Salem, *Ceram. Eng. Sci. Proc. ,* vol. 24, p. 357, 2003.

[115] J. Kübler, R. Primas, and B. Gut, "Mechanical strength of thermally aged and cycled thin zirconia sheets, Advances in Science and Technology, Ceramics: Charting the Future, ed. P. Vincenzini, Techna, Florence, Italy," ISBN 88-86538-02-21995.

[116] A. F. Bower, *Applied mechanics of solids*: CRC press, 2009.

[117] C. M. a. version, "Structural Mechanics user's guide," 2012.

[118] W. Weibull, "Wide applicability," *Journal of applied mechanics,* vol. 103, p. 33, 1951.

[119] D. Munz and T. Fett, *Ceramics: mechanical properties, failure behaviour, materials selection* vol. 36: Springer Science & Business Media, 2013.

[120] J. Pascual, T. Lube, and R. Danzer, "Fracture statistics of ceramic laminates strengthened by compressive residual stresses," *Journal of the European Ceramic Society,* vol. 28, pp. 1551-1556, 2008.

[121] T. Chartier, D. Merle, and J. Besson, "Laminar ceramic composites," *Journal of the European Ceramic Society,* vol. 15, pp. 101-107, 1995.

[122] M. Lugovy, N. Orlovskaya, K. Berroth, and J. Kuebler, "Macrostructural engineering of ceramic-matrix layered composites," *Composites science and technology,* vol. 59, pp. 1429-1437, 1999.

[123] O. R. N. Laboratory. Available: http://neutrons.ornl.gov/facilities/SNS/

[124] G. B. o. W. Records. Available: http://www.guinnessworldrecords.com/records-5000/most-powerful-pulsed-spallation-neutron-source/

[125] T. M. Holden, A. Stoica, X. Wang, K. An, H. D. Skorpenske, A. Jones*, et al.*, "First results from the VULCAN diffractometer at the SNS," in *Materials Science Forum*, 2010, pp. 105-110.

[126] K. An, H. D. Skorpenske, A. D. Stoica, D. Ma, X.-L. Wang, and E. Cakmak, "First In Situ Lattice Strains Measurements Under Load at VULCAN," *Metallurgical and Materials Transactions A,* vol. 42, pp. 95-99, 2011.

[127] R. Riedel, "Spallation Neutron Source Data Acquisition System," SNS Report No. 107030200-TD005-R04, Oak Ridge National Laboratory, Oak Ridge, TN2007.

[128] K. An, "Data Reduction and Interactive Visualization Software for Event
Mode Neutron Diffraction," in *ORNL Report, ORNL-TM-2012-621*, ed. Oak Ridge National Laboratory, Oak Ridge, TN, USA, 2012.

[129] J.-S. Zhou, J.-Q. Yan, and J. Goodenough, "Bulk modulus anomaly in RCoO_ {3}(R= La, Pr, and Nd)," *Physical review b,* vol. 71, p. 220103, 2005.

[130] S. Murata, S. Isida, M. Suzuki, Y. Kobayashi, K. Asai, and K. Kohn, "Elastic anomalies with the spin-state transitions in LaCoO< sub> 3</sub>," *Physica B: Condensed Matter,* vol. 263, pp. 647-649, 1999.

[131] P. E. Vullum, J. Mastin, J. Wright, M.-A. Einarsrud, R. Holmestad, and T. Grande, "In situ synchrotron X-ray diffraction of ferroelastic La0.8Ca0.2CoO3 ceramics during uniaxial compression," *Acta materialia,* vol. 54, pp. 2615-2624, 2006.

[132] N. Orlovskaya, Y. Gogotsi, M. Reece, B. Cheng, and I. Gibson, "Ferroelasticity and hysteresis in LaCoO 3 based perovskites," *Acta materialia,* vol. 50, pp. 715-723, 2002.

[133] N. Orlovskaya, N. Browning, and A. Nicholls, "Ferroelasticity in mixed conducting LaCoO3 based perovskites: a ferroelastic phase transition," *Acta Materialia,* vol. 51, pp. 5063-5071, 10/6/ 2003.

[134] S. Faaland, T. Grande, M.-A. Einarsrud, P. E. Vullum, and R. Holmestad, "Stress–Strain Behavior During Compression of Polycrystalline La1−xCaxCoO3 Ceramics," *Journal of the American Ceramic Society,* vol. 88, pp. 726-730, 2005.

[135] N. Orlovskaya, M. Lugovy, S. Pathak, D. Steinmetz, J. Lloyd, L. Fegely*, et al.*, "Thermal and mechanical properties of LaCoO 3 and La 0.8 Ca 0.2 CoO 3 perovskites," *Journal of Power Sources,* vol. 182, pp. 230-239, 2008.

[136] S. Pathak, J. Kuebler, A. Payzant, and N. Orlovskaya, "Mechanical behavior and electrical conductivity of La1−xCaxCoO3 (x = 0, 0.2, 0.4, 0.55) perovskites," *Journal of Power Sources,* vol. 195, pp. 3612-3620, 6/1/ 2010.

[137] N. O. M. Lugovy, M. Reece, "Title," unpublished|.

[138] E. 843-2:2006, "Advanced technical ceramics. Mechanical properties of monolithic ceramics at room temperature. Determination of Young’s modulus, shear modulus and Poisson’s ratio," ed, 2006.

[139] M. R. Daymond, M. A. M. Bourke, and R. B. Von Dreele, "Use of Rietveld refinement to fit a hexagonal crystal structure in the presence of elastic and plastic anisotropy," *Journal of Applied Physics,* vol. 85, pp. 739-747, 1999.

[140] M. R. Daymond, "The determination of a continuum mechanics equivalent elastic strain from the analysis of multiple diffraction peaks," *Journal of Applied Physics,* vol. 96, pp. 4263-4272, 2004.

[141] S. Yu and M. Shaskolskaya, "Fundamentals of crystal physics," *Mir Publ, Moscow,* 1982.

[142] W. D. Callister and D. G. Rethwisch, *Materials science and engineering: an introduction* vol. 7: Wiley New York, 2007.

[143] R. J. Amjad Aman, Yan Chen, Richard Stadelmann, Mykola Lugovy, Nina Orlovskaya, E. Andrew Payzant, Clarina dela Cruz, Michael J. Reece, Thomas Graule, Jakob Kuebler, "Title," unpublished|.

[144] J. B. Goodenough, "Narrow-band electrons in transition-metal oxides," *Czechoslovak Journal of Physics B,* vol. 17, pp. 304-336, 1967.

[145] J. Stevenson, T. Armstrong, R. Carneim, L. R. Pederson, and W. Weber, "Electrochemical Properties of Mixed Conducting Perovskites La1− x M x Co1− y Fe y O 3− δ (M= Sr, Ba, Ca)," *Journal of the Electrochemical Society,* vol. 143, pp. 2722-2729, 1996.

[146] V. Kharton, F. Figueiredo, A. Kovalevsky, A. Viskup, E. Naumovich, A. Yaremchenko*, et al.*, "Processing, microstructure and properties of LaCoO 3− δ ceramics," *Journal of the European Ceramic Society,* vol. 21, pp. 2301-2309, 2001.

[147] L. Simonot and G. Maire, "A comparative study of LaCoO 3, Co 3 O 4 and LaCoO 3—Co 3 O 4: I. Preparation, characterisation and catalytic properties for the oxidation of CO," *Applied Catalysis B: Environmental,* vol. 11, pp. 167-179, 1997.

[148] S. Royer, F. Berube, and S. Kaliaguine, "Effect of the synthesis conditions on the redox and catalytic properties in oxidation reactions of LaCo 1− x Fe x O 3," *Applied Catalysis A: General,* vol. 282, pp. 273-284, 2005.

[149] N. Orlovskaya, K. Kleveland, T. Grande, and M.-A. Einarsrud, "Mechanical properties of LaCoO 3 based ceramics," *Journal of the European Ceramic Society,* vol. 20, pp. 51-56, 2000.

[150] M. Senarıs-Rodrıguez and J. Goodenough, "LaCoO 3 revisited," *Journal of Solid State Chemistry,* vol. 116, pp. 224-231, 1995.

[151] G. Thornton, B. Tofield, and A. Hewat, "A neutron diffraction study of LaCoO 3 in the temperature range 4.2< T< 1248 K," *Journal of Solid State Chemistry,* vol. 61, pp. 301-307, 1986.

[152] J. Mastin, M.-A. Einarsrud, and T. Grande, "Structural and Thermal Properties of La1-x Sr x CoO3-δ," *Chemistry of materials,* vol. 18, pp. 6047-6053, 2006.

[153] G. Maris, Y. Ren, V. Volotchaev, C. Zobel, T. Lorenz, and T. Palstra, "Evidence for orbital ordering in LaCoO 3," *Physical Review B,* vol. 67, p. 224423, 2003.

[154] V. Gnezdilov, K.-Y. Choi, Y. Pashkevich, P. Lemmens, S. Shiryaev, G. Bychkov*, et al.*, "Low temperature mixed spin state of Co3+ in LaCoO3 evidenced from Jahn-Teller lattice distortions," *arXiv preprint cond-mat/0601121,* 2006.

[155] Y. Wang and H. J. Fan, "Orbital ordering-driven ferromagnetism in LaCoO3 nanowires," *Journal of Applied Physics,* vol. 108, p. 3917, 2010.

[156] P. E. Vullum, R. Holmestad, H. L. Lein, J. Mastin, M. A. Einarsrud, and T. Grande, "Monoclinic Ferroelastic Domains in LaCoO3 - Based Perovskites," *Advanced Materials,* vol. 19, pp. 4399-4403, 2007.

[157] P. E. Vullum, H. L. Lein, M.-A. Einarsrud, T. Grande, and R. Holmestad, "TEM observations of rhombohedral and monoclinic domains in LaCoO3-based ceramics," *Philosophical Magazine,* vol. 88, pp. 1187-1208, 2008.

[158] Y. Kimura, "Mechanical Properties of Perovskite and Related Oxides for Energy Conversion Devices," 2015.

[159] A. Julian, E. Juste, P.-M. Geffroy, N. Tessier-Doyen, P. Del Gallo, N. Richet*, et al.*, "Thermal behaviour of La 0.8 Sr 0.2 Fe 1− x Ga x O 3− δ (x= 0 or x= 0.3)," *Journal of the European Ceramic Society,* vol. 29, pp. 2603-2610, 2009.

[160] E. Sánchez-González, P. Miranda, J. J. Meléndez-Martínez, F. Guiberteau, and A. Pajares, "Temperature dependence of mechanical properties of alumina up to the onset of creep," *Journal of the European Ceramic Society,* vol. 27, pp. 3345-3349, 2007.

[161] L. Dong, D. S. Stone, and R. S. Lakes, "Softening of bulk modulus and negative Poisson ratio in barium titanate ceramic near the Curie point," *Philosophical Magazine Letters,* vol. 90, pp. 23-33, 2010.

[162] T. Okamura, S. Shimizu, M. Mogi, M. Tanimura, K. Furuya, and F. Munakata, "Elastic properties of Sr-and Mg-doped lanthanum gallate at elevated temperature," *Journal of power sources,* vol. 130, pp. 38-41, 2004.

[163] CEN, "EN 843-1, Part 1: Determination of Flexural Strength," ed. Brussels, Belgium: EUROPEAN COMMITTEE FOR STANDARDIZATION, 2006.

[164] CEN, "EN 843-2, Part 2: Determination of Young's modulus, shear modulus and Poisson's ratio," ed. Brussels, Belgium: EUROPEAN COMMITTEE FOR STANDARDIZATION, 2006.

[165] A. Larson and R. Von Dreele, "GSAS: generalized structure analysis system," *Document LAUR,* pp. 86-748, 1994.

[166] B. H. Toby, "EXPGUI, a graphical user interface for GSAS," *Journal of applied crystallography,* vol. 34, pp. 210-213, 2001.

[167] K. Kleveland, N. Orlovskaya, T. Grande, A. M. Moe, M. A. Einarsrud, K. Breder*, et al.*, "Ferroelastic Behavior of LaCoO~ 3-Based Ceramics," *J. Am. Ceram. Soc.,* vol. 84, pp. 2029-2033, 2001.

[168] N. Orlovskaya, N. Browning, and A. Nicholls, "Ferroelasticity in mixed conducting LaCoO 3 based perovskites: a ferroelastic phase transition," *Acta materialia,* vol. 51, pp. 5063-5071, 2003.

[169] P. G. Radaelli and S.-W. Cheong, "Structural phenomena associated with the spin-state transition in LaCoO 3," *Physical Review B,* vol. 66, p. 094408, 2002.

[170] D. Kozlenko, N. Golosova, Z. Jirak, L. Dubrovinsky, B. Savenko, M. Tucker*, et al.*, "Temperature-and pressure-driven spin-state transitions in LaCoO 3," *Physical Review B,* vol. 75, p. 064422, 2007.

[171] Z. Zhang, J. Koppensteiner, W. Schranz, D. Prabhakaran, and M. A. Carpenter, "Strain coupling mechanisms and elastic relaxation associated with spin state transitions in LaCoO3," *Journal of Physics: Condensed Matter,* vol. 23, p. 145401, 2011.

[172] K. Knížek, Z. Jirák, J. Hejtmánek, M. Veverka, M. Maryško, G. Maris*, et al.*, "Structural anomalies associated with the electronic and spin transitions in LnCoO3," *The European Physical Journal B-Condensed Matter and Complex Systems,* vol. 47, pp. 213-220, 2005.

[173] P. G. Radaelli, M. Marezio, H. Y. Hwang, S. W. Cheong, and B. Batlogg, "Charge localization by static and dynamic distortions of the ${\mathrm{MnO}}_{6}$ octahedra in perovskite manganites," *Physical Review B,* vol. 54, pp. 8992-8995, 10/01/ 1996.

[174] M. Abrashev, A. Litvinchuk, M. Iliev, R. Meng, V. Popov, V. Ivanov*, et al.*, "Comparative study of optical phonons in the rhombohedrally distorted perovskites LaAlO 3 and LaMnO 3," *Physical Review B,* vol. 59, p. 4146, 1999.

[175] N. Orlovskaya, D. Steinmetz, S. Yarmolenko, D. Pai, J. Sankar, and J. Goodenough, "Detection of temperature-and stress-induced modifications of La Co O 3 by micro-Raman spectroscopy," *Physical Review B,* vol. 72, p. 014122, 2005.

[176] A. Aman, R. Stadelmann, and N. Orlovskaya, "Unpublished work."

[177] E. K. Salje and H. Zhang, "Domain boundary pinning and elastic softening in KMnF3 and KMn1− xCaxF3," *Journal of Physics: Condensed Matter,* vol. 21, p. 035901, 2008.

[178] R. J. Harrison, S. A. Redfern, and J. Street, "The effect of transformation twins on the seismic-frequency mechanical properties of polycrystalline Ca1–xSrxTiO3 perovskite," *American Mineralogist,* vol. 88, pp. 574-582, 2003.

[179] W. Lee, E. Salje, and U. Bismayer, "Influence of point defects on the distribution of twin wall widths," *Physical Review B,* vol. 72, p. 104116, 2005.

[180] A. Amjad, X. Yunjun, B. Haiyan, and O. Nina, "Interconnected Software Modules to Aid the Learning of Fuel Cell Courses," Seattle, Washington.

[181] A. A. Haiyan Bai, Yunjun Xu, Nina Orlovskaya, Mingming Zhou,, "Effects Of Web-Based Interactive Modules On Engineering Students' Learning Motivations," *American Journal of Engineering Education,* vol. 7, December, 2016 2016.

[182] Y. A. Cengel and M. A. Boles, "Thermodynamics: an engineering approach," *Sea,* vol. 1000, p. 8862, 1994.

[183] S. Srinivasan, *Fuel cells: from fundamentals to applications*: Springer Science & Business media, 2006.

[184] S. C. Singhal and K. Kendall, *High-temperature solid oxide fuel cells: fundamentals, design and applications*: Elsevier, 2003.

[185] M. Dudek, P. Tomczyk, P. Wygonik, M. Korkosz, P. Bogusz, and B. Lis, "Hybrid fuel cell–battery system as a main power unit for small Unmanned Aerial Vehicles (UAV)," *Int. J. Electrochem. Sci,* vol. 8, pp. 8442-8463, 2013.

[186] F.-B. Weng, A. Su, C.-Y. Hsu, and C.-Y. Lee, "Study of water-flooding behaviour in cathode channel of a transparent proton-exchange membrane fuel cell," *Journal of power sources,* vol. 157, pp. 674-680, 2006.

[187] M. Kebritchi, A. Hirumi, and H. Bai, "The effects of modern mathematics computer games on mathematics achievement and class motivation," *Computers & education,* vol. 55, pp. 427-443, 2010.

[188] J. M. Keller, *Motivational design for learning and performance: The ARCS model approach*: Springer Science & Business Media, 2009.